NUCLEAR STRUCTURE STUDIES OF TRANSITIONAL NUCLEI

THESIS SUBMITTED FOR THE DEGREE OF DOCTOR OF PHILOSOPHY (SCIENCE) IN PHYSICS

BY

SOUMENDU SEKHAR BHATTACHARJEE

UNIVERSITY OF CALCUTTA

KOLKATA

2016

Thesis Title: Nuclear Structure Studies Of Transitional Nuclei

Abstract

The present thesis work is based on the detailed investigation of the nuclear structure of transitional nuclei, such as ^{26}Mg, ^{29}Si at the interface of the *sd* and *pf* shells. These nuclei are uniquely positioned in between the valley of stability and the island of inversion. The level structures of nuclei along the valley of stability are dominated by single particle excitations, whereas at island of inversion they are dominated by collective excitations. Hence, the structure of the nuclei in the transitional region is likely to reveal an intriguing interplay between these two degrees of freedom. The excitation of nucleons within the *sd* shell would give rise to positive parity sequences. There are sufficient particles within this major shell to induce deformation in these mid-shell nuclei. Further, the excitation of a single nucleon across the *sd-pf* shell gap, would result in the substantial occupation of the $f_{7/2}$ *(l=3)* orbital, which is expected to favour deformed structures. The deformed structures, could be uniquely probed within the framework of the spherical shell model due to the availability of adequate computational resources coupled to the development of appropriate interactions (inter and intra shell). The detailed study of the lowest negative parity level in these nuclei is warranted as the level energy encodes the signature of the energy gap between the *sd* & *pf* shells, which has a direct bearing on our understanding of the *"island of inversion"*. The aforementioned features motivated the present thesis work.

It is pertinent to mention that all the previous investigations on the level structure of these nuclei were primarily based on light ion induced reactions using a modest detector setup, and consequently, had a substantial scatter and some of them have large uncertainties even at low excitation energies and spins. Hence, the need to re-visit the level structure of these transitional nuclei, using high resolution γ-ray spectroscopy, following heavy-ion induced fusion evaporation reactions. The use of a multi-Clover array was best suited for these measurements, due to the superior detection efficiency of these composite detectors for high energy γ-rays (≥ 2 MeV), routinely observed in these nuclei. Several new transitions have been observed in the level scheme of these nuclei from the γ - γ coincidence measurement. Spin parity assignments were made following a consistent analysis of the angular intensity anisotropy and the linear polarization measurements. The level lifetime is extracted from the Doppler Shift Attenuation Method. The transition probabilities extracted from lifetime measurements are indicative of deformation in these nuclei. Large basis shell model calculations were successfully carried out for these nuclei, whose predictions are in agreement with the experimental observables. The model calculations have successfully reproduced the deformed characteristics of these mid-shell transitional nuclei at the interface of the *sd* and *pf* shells. Thus all the textbooks tools prevalent in the field of in-beam gamma rays spectroscopy have been uniquely utilized in the present thesis and the shell model could explain both the single particle and collective features of these nuclei.

Soumendu Sekhar Bhattacharjee

Acknowledgements

Without people who supported me and believed in me, this thesis by far the most significant scientific accomplishment in my life, could not have been realized.

Firstly, I would like to thank Dr. S. S. Ghugre and Dr. A. K. Sinha for allowing me to join the Nuclear Physics group at the UGC-DAE CSR, Kolkata Centre. It has indeed been a privilege for me to to have Dr. R. Raut as associate supervisor of my research work. I express my deep sense of gratitude to him for his interest and the concern he has shown at every stage of my work. Dr Raut has always offered advice and insight throughout this work. I appreciate his vast knowledge and skill in many areas and his kindness to part with the various developments carried out by him, which played a crucial role in academically shaping the present thesis.

I would like express my gratitude to my research advisor, Dr. S. S. Ghugre. His trust and scientific knowledge inspired me to make the right decisions at the crucial moments of this journey. Without his inspiring, enthusiastic and critical guidance and his trust in me, this work would not have been possible. His kindness will always be remembered with reverence in the years to come.

I have great pleasure in expressing my gratitude and indebtedness to Dr. A. K. Sinha, Director UGC DAE CSR, Indore for his constant encouragement and invaluable suggestions during the tenure of my research. The present work is the result of his interest and deep vision. This thesis is more a testament to the efforts of my mentors in the Nuclear Physics Group at the UGC DAE CSR, Kolkata Centre rather than my own.

It has been my privilege to be associated with Prof. Umesh Garg during my research carrier. His thoughtful conversation and critical comments were most helpful. Special mention need be made of Prof. Alex Brown for the discussions we had on Shell model

calculations and for the valuable suggestions we have received from him. I would like to thank Dr. J. P. Greene (Argonne National Laboratory, USA) for the ^{18}O target and W. P. Tan and Late Dr. Larry Lamm (University of Notre Dame, USA) for providing the enriched ^{18}O cathode. Special thanks to Prof. Z. Elekes for his help, guidance and valuable inputs during the GEANT4 simulations.

A special thank to Mr. Kausik Basu from UGC-DAE CSR, Kolkata Centre for his help during the experiment. My heartfelt thanks to my fellow lab mates, especially Dr. Ritwika Chakrabarti, Rajashri Bhattacharjee, Soumya Kanti Das and Saradindu Samanta for their help and support during this thesis work. I would like to thank all the faculty members and research scholars of UGC-DAE CSR, whose supportive attitude helped me during my tenure at the Kolkata Centre. I will be failing in my duty if I do not mention the technical and administrative staff of this centre for their timely help in all relevant matters.

I thank all the Pelletron staff at IUAC, New Delhi and TIFR, Mumbai for their excellent support during the experiments. I thank all the participants of the INGA (Indian National Gamma Array) collaboration for their efforts in setting up the INGA facility.

I would like to acknowledge the financial assistance in the form of a fellowship (JRF and SRF, CSIR sanction No. 09/838(0038)2010-EMR-I) from the Council of Scientific and Industrial Research (CSIR), Government of India. The INGA Project is partially supported by the Department of Science Technology (DST), Government of India, under Grant No. IR/S2/PF-03/2003-III. This work has been supported in part by the U.S. National Science Foundation (Grants No. PHY-1068192 and PHY-1419765).

The encouragement and motivation that was given to me by my mother and sister to carry out this work will never be forgotten. I would like to share this moment of happiness with all my family members and well-wishers.

Soumendu Sekhar Bhattacharjee

UGC-DAE Consortium for Scientific Research

Kolkata, India.

List of Publications

Published in referred journals:

Thesis related:

1. Nuclear structure study of ^{26}Mg following heavy-ion-induced fusion-evaporation reaction: **S. S. Bhattacharjee**, R. Bhattacharjee, R. Chakrabarti, R. Raut, S. S. Ghugre, A. K. Sinha, T. Trivedi, L. Chaturvedi, S. Saha, J. Sethi, R. Palit ; **Phys. Rev. C 89, 024324 (2014)**

2. Spectroscopy and shell model calculations in Si isotopes: **S. S. Bhattacharjee**, R. Bhattacharjee, R. Raut, S. S. Ghugre, A. K. Sinha, L. Chaturvedi, T. Trivedi, U. Garg, S. Ray, B. K. Yogi, M. Kumar Raju, R. Chakrabarti, S. Mukhopadhyay, A. Dhal, R. P. Singh, N. Madhavan, S. Muralithar, S. Saha, J. Sethi, R. Palit ; **Phys. Rev. C 91, 044306 (2015)**

Others:

1. Level lifetimes in ^{32}P obtained using the Doppler-shift attenuation method with thick molecular targets: R. Bhattacharjee, **S. S. Bhattacharjee**, K. Basu, P. V. Rajesh, R. Raut, S. S. Ghugre, D. Das, A. K. Sinha, L. Chaturvedi, U. Garg, S. Ray, B. K. Yogi, M. Kumar Raju, R. Chakrabarti, S. Mukhopadhyay, A. Dhal, R. P. Singh, N. Madhavan, S. Muralithar ; **Phys. Rev. C 90, 044319 (2014)**

2. A new high-spin isomer in ^{195}Bi: T. Roy, G. Mukherjee, N. Madhavan, T. K. Rana, Soumik Bhattacharya, Md. A. Asgar, I. Bala, K. Basu, **S. S. Bhattacharjee**, C. Bhattacharya, S. Bhattacharya, S. Bhattacharyya, J. Gehlot, S. S. Ghugre, R. K. Gurjar, A. Jhingan, R. Kumar, S. Muralithar, S. Nath, H. Pai, R. Palit, R. Raut, R. P. Singh, A. K. Sinha, T. Varughese ; **Eur. Phys. J. A. 51, 153 (2015)**

Conference proceedings

National:

1. Application of state-of-the-art Monte Carlo simulations in DSAM analysis: S. Das, S. Samanta, R. Bhattacharjee, **S. S. Bhattacharjee**, R. Raut, S. S. Ghugre, A. K. Sinha, U. Garg, L. Chaturvedi, T. Trivedi, S. Mukhopadhyay, R. Chakrabarti, A. Dhal, M. Kumar Raju, N. Madhavan, R. P. Singh, S. Muralithar, S. Saha, J. Sethi, R. Palit ; **Proceedings of the DAE Symposium on Nuclear Physics, 60, 74 (2015)**.

2. Installation of a Digitizer based Pulse Processing and Data Acquisition System and related developments: S. Samanta, S. Das, R. Bhattacharjee, **S. S. Bhattacharjee**, K. Basu, H. Sultana, R. Raut, S. S. Ghugre, A. K. Sinha, H. Tan ; **Proceedings of the DAE Symposium on Nuclear Physics, 60, 1020 (2015)**.

3. Spectroscopy of ^{25}Mg: H. Sultana, A. Chakraborty, R. Bhattacharjee, **S. S. Bhattacharjee**, R. Chakrabarti, S. K. Das, S. Samanta, S. S. Ghugre, R. Raut, A. K. Sinha, T. Trivedi, L. Chaturvedi, S. Saha, J. Sethi, R. Palit ; **Proceedings of the DAE Symposium on Nuclear Physics, 60, 268 (2015)**.

4. High Spin Spectroscopic Study of a few nearly spherical nuclei in $A \sim 150$ region: H. Sultana, A. Chakraborty, R. Bhattacharjee, **S. S. Bhattacharjee**, S. K. Das, S. Samanta, S. S. Ghugre, R. Raut, A. K. Sinha, L. Chaturvedi, B. K. Yogi, A. Jhingan, N. Madhavan, S. Muralithar, S. Nath, R. P. Singh, P. Sugathan, Krishichayan ; **Proceedings of the DAE Symposium on Nuclear Physics, 60, 266 (2015)**.

5. Lifetime Measurements in *sdpf* Nuclei with Thick Molecular Target: R. Bhattacharjee, **S. S. Bhattacharjee**, S. Samanta, S. Das, N. Ghosh, K. Basu, P.V. Rajesh, R. Raut, S. S. Ghugre, D. Das, A. K. Sinha, U. Garg, T. Trivedi, L. Chaturvedi, S. Ray, B. K. Yogi, S. Mukhopadhyay, R. Chakrabarti, A. Dhal, M. Kumar Raju, N. Madhavan, R. P. Singh, S. Muralithar, S. Saha, J. Sethi, R.

Palit ; **Proceedings of the DAE Symposium on Nuclear Physics, 59, 138 (2014)**.

6. A New Isomer in^{195}Bi Identified at the Focal Plane of HYRA: T. Roy, G. Mukherjee, Md. A. Asgar, Soumik Bhattacharya, H. Pai, T. K Rana, S. Bhattacharyya, C. Bhattacharya, S. Bhattacharya, N. Madhavan, S. Nath, R. P. Singh, A. Jhingan, S. Muralithar, R. Kumar, J. Ghelot, T. Varughese, I. Bala, R. K. Gurjar, A. K. Sinha, S. S. Ghugre, R. Raut, **S. S. Bhattacharjee**, K. Basu, R. Palit ; **Proceedings of the DAE Symposium on Nuclear Physics, 59, 126 (2014)**.

7. Re-examination of Dipole Band in^{104}Ag: K. Suryanarayana, A. Tejaswi, M. Kumar Raju, M. Ratna Raju, D. Vijaya Lakshmi, T. Seshi Reddy, J. Matta, A. D. Ayangeakaa, U. Garg, R. Bhattacharjee, **S. S. Bhattacharjee**, S. Samanta, S. Das, N. Ghosh, R. Raut, S. S. Ghugre, A. K. Sinha, S. Mukhopadhyay, L. Dhanu, B. K. Nayak, D. C. Biswas, A. Y. Deo, S. K. Tandel, N. Kaur, Ashok Kumar, S. Saha, J. Sethi, R. Palit, S. Muralithar, R. P. Singh, S Chattopadhyay, P. V. Madhusudhana Rao ; **Proceedings of the DAE Symposium on Nuclear Physics, 59, 292 (2014)**.

8. DSAM Analysis with Novel Backing using Modified LINESHAPE Program: A. K. Sinha, S. S. Ghugre, R. Raut, S. Ray, **S. S. Bhattacharjee**, R. Bhattacharjee ; **Proceedings of the DAE Symposium on Nuclear Physics, 58, 268 (2013)**.

9. Shell Model Calculations for Negative Parity States in $sd - pf$ Nuclei: R Bhattacherjee, **S. S. Bhattacharjee**, R. Raut, S. S. Ghugre, A. K Sinha ; **Proceedings of the DAE Symposium on Nuclear Physics, 58, 270 (2013)**.

10. High spin states in ^{205}At: D. Kanjilal, A. Bisoi, M. Das, C. C. Dey, S. Ray, R. Palit, S. Saha, J. Sethi, T. Trivedi, S. Nag, **S. S. Bhattacharjee**, S. Saha ; **Proceedings of the DAE Symposium on Nuclear Physics, 58, 264 (2013)**.

11. Study of deformed structures in N $\sim$ Z nuclei: R. Bhattacharjee, R. Chakrabarti, **S. S. Bhattacharjee**, R. Raut, S. S. Ghugre, L. Chaturvedi, M. Kumar Raju,

A. Dhal, N. Madhavan, R. P. Singh, S. Muralithar, B. K. Yogi, U. Garg, A. K. Sinha ; **Proceedings of the DAE Symposium on Nuclear Physics, 57, 336 (2012)**.

12. Novel Method of Lifetime Measurements in ^{156}Dy with Aerogel Backing: A. K. Sinha, **S. S. Bhattacharjee**, R. Bhattacherjee, R. Raut, S. S. Ghugre, R. P. Singh, N. Madhavan, S. Muralithar, P. V. M. Rao, M. Kumar Raju, Krishichayan, L. Chaturvedi, S. Saha, J. Sethi, R. Palit, S. Mukhopadhyay, G. Smith,R. V. F. Janssens ; **Proceedings of the DAE Symposium on Nuclear Physics, 57, 338 (2012)**.

13. Enriched ^{148}Nd Target on Ultra Low-Density Backing: K. Basu, **S. S. Bhattacharjee**, R. Raut, S. S. Ghugre, S. R. Abhilash, D. Kabiraj, I. Bala, R. P. Singh, S. Muralithar, A. K. Sinha ; **Proceedings of the DAE Symposium on Nuclear Physics, 57, 946 (2012)**.

14. Nuclear Structure Studies in the Vicinity of the "Island of Inversion": **S. S. Bhattacharjee**, R. Chakrabarti, R. Bhattacharjee, R. Raut, S. S. Ghugre , A. K. Sinha, S. Saha , J. Sethi, T. Trivedi, R. Palit ; **Proceedings of the DAE Symposium on Nuclear Physics, 56, 390 (2011)**.

15. Simulations for Segmented Germanium Detectors: **S. S. Bhattacharjee**, S. S. Ghugre , A. K. Sinha, Z. Elekes ; **Proceedings of the DAE Symposium on Nuclear Physics, 56, 1114 (2011)**.

16. Design & simulation of a Composite Gamma Detector with fast-Timing, Good Resolution, Efficiency & Tracking Possibilities: **S. S. Bhattacharjee**, R. Raut, S. S. Ghugre, A. K. Sinha, R. Palit, I. Kojouharov, J. Gerl ; **Proceedings of the DAE Symposium on Nuclear Physics, 56, 1116 (2011)**.

Contents

List of Figures

List of Tables

Chapter - 1

Introduction and Motivation

The nucleus is a few body quantum mechanical system and the constituents of this system *viz.* neutrons and protons are bound together by a strong nuclear force within the nucleus. Within the small dimension of the nucleus, the protons and the neutrons are bound together by the strong (nuclear) force. Nuclear force is the strongest among the four known forces (gravitational, electro-magnetic, weak and strong) in nature. It is a short range force, operational over an extremely short distance $\sim$ few fm, and thus of relevance only within the nuclear dimensions. The spin dependent part of the nuclear force is evident from the properties of the deuteron (proton neutron bound state) nucleus. The charge independent nature of the nuclear force ($p-p$, $n-p$ and $n-n$ forces are equal) was arrived at from the study of the properties of the mirror nuclei (for a given mass number the numbers of protons in one nucleus is equal to the number of neutrons in the other nucleus and vice versa), for example ^{25}Al and ^{25}Mg which are a pair of mirror nuclei, have similar masses, the only minor difference is due to the Coulomb energy. The repulsive nature of the nuclear force (at distance less than 0.5 fm) can be estimated from the high energy scattering experiments. Thus the nuclear force has very unique features, which may hinder a complete mathematical understanding of this force, as of now.

Hence, our understanding of the nuclear force and the potential is essentially empirical. One such insight is based on the study of nuclear masses. It was observed that the mass of a nucleus is always less than the sum of the individual masses of its constituents *viz.* the protons and the neutrons. This mass difference is known as mass defect (Δm) and from the mass energy equivalence ($\mathrm{E} = \Delta mc^2$) relation, the mass defect can be converted to energy, which is known as the nuclear binding energy (B). The nuclear binding energy is the energy required to break the nucleus into its independent individual constituents neutrons and protons. It has been well established that the binding energy per nucleon ($\bar{B} = B/A \sim 8\ MeV$) is fairly constant for all nuclei. This is attributed to the short range saturation property of the nuclear force *ie.*, the nucleon interacts only with

it's immediate neighbours, (a quantity which is approximately constant for all nuclei) and hence is not affected by the sea of other nucleons. The pioneering work in arriving at a model for the nuclear force, was undertaken by Yukawa way back in the 1930's, [1] and according to his theory the force carrier is massive. From the range of the nuclear force which is $\sim fm$, he suggested that the force carrier must weigh $\sim 100\ MeV/c^2$ (according to the uncertainty principle range of the force is inversely proportional to the mass of the force carrier). Yukawa modeled the nuclear potential in the form :

$$V(r) = -g^2 e^{-\mu r}/r, \tag{1}$$

where g is the amplitude of potential, μ is the Yukawa particle mass (pion) and r is the radial distance to the particle. Yukawa potential will give the interaction a finite range, so that particles at greater distances will not practically interact. Attempts were also made to use the well known potentials such as square-well potential, simple harmonic oscillator potential, to represent the nuclear potential. This resulted in an over simplification as these simplistic potentials did not appropriately include some of the fundamental nuclear properties, such as the shape of the potential, the requirement that the charge distribution should vary smoothly to zero, to name a few.

Further, in absence of a comprehensive mathematical and physical knowledge of the nuclear potential, it is imperative to have a model for the same. To understand the observed properties of the nucleus various models have been developed. Historically the liquid drop model was one of the earlier models, followed by the spherical shell model and collective model.

Based on the analogy between a nucleus and a liquid drop, where the nucleus could be treated as a incompressible nuclear fluid. Bohr and Wheeler, developed the liquid drop model for the nucleus where the fluid is made of nucleons (protons and neutrons), which are held together by the strong nuclear force. This model was able to explain some of the macroscopic properties of the nucleus, such as the binding energy, the energy released in fission to name a few. If the nucleus is comprised of Z number of protons and N number of neutrons, the mass of the nucleus is then given by :

$$M(A,Z) = ZM_p + (A-Z)M_n - B(A,Z), \tag{2}$$

Where M_p *and* M_n are the mass of proton and neutron respectively and B(A,Z) ($=M(A,Z)c^2$) is the binding energy of the nucleus.

The empirical Bethe Weizsäcker mass formula [2, 3] which is based on the liquid drop model, parametrizes, the binding energy into several terms, and is given by :

$$B(A,Z) = a_1 A - a_2 A^{2/3} - a_3 Z(Z-1)/A^{1/3} - a_4 (N-Z)^2/A \pm a_5 A^{-3/4} \qquad (3)$$

The first term is known as the volume term and it is proportional to the number of nucleons (A, being the mass number). The nucleons at the surface, which have a dissimilar ambiance on either sides, tend to lower the stability of the nucleus, and hence would have a negative contribution to the binding energy. This is analogous to the property of surface tension in liquids. As the surface area is proportional to R^2, (R being the nuclear radius and R = $R_0 A^{1/3}$) so the surface term is expected to have a $A^{2/3}$ dependence. The third term in the binding energy formula represents the "repulsive" and hence "disruptive" Coulomb effect between the protons, which is expected to be proportional to $\sim Z^2$ (for high Z nuclei). This term would have a dominant effect for heavier nuclei (higher atomic number), which qualitatively explains the reduced stability for these nuclei. The fourth term referred to as asymmetry term, is proportional to the square of the neutron excess. The next term in the binding energy formula is known as pairing term, which incorporates the enhanced stability in nucleus with even number of protons as well as neutrons. As mentioned earlier this model has limited success with the macroscopic nuclear observables, and could not explain the finer microscopic nuclear properties (such as spin, parity, electro-magnetic transition probability etc).

The inert nature (enhanced stability) for atoms with certain configurations (number) of electrons, has been attributed to the completely filled electron shell, which has resulted in a convincing establishment of the electronic shell structure in atoms. There are several empirical observations of enhanced stability for nuclei with a certain nucleon number (number of neutrons or protons or both = 2, 8, 20, 28, 50, 82, 126), such as, the sudden increase in the binding energy per nucleon, as compared with it's immediate neighbour, which is indicative of an enhanced stability for these nuclei. Thus it is logical to think of an analogous nucleon shell structure / configuration for the nucleus.

Within this framework, we assume that the nucleons experience a potential due to the rest of the nucleons. We usually model this potential and the simplistic form is the well known harmonic oscillator potential, which successfully reproduced the first three "magic numbers" (magic numbers : nucleon configuration for which the nucleus has an enhanced stability). The revolutionary concept of introducing the *spin-orbit* term ($l.s$ coupling) by Goeppert-Maier and Jensen [4–6] successfully reproduced all the observed magic numbers. Due to this term the energy levels were appropriately bunched with a large energy gap between two major oscillator shells, owing to the intrusion of one of the higher angular momentum orbital ($g_{9/2}$ for example) from the next major shell into the lower shell. The model hence is known as spherical shell model and has been successful in reproducing the properties of nuclei in the vicinity of the nucleon magic number. This model till date is a fundamental microscopic model and has been extensively used in the present thesis work. The distribution of the predicted energy levels including the degeneracy of the sub-shells, as predicted by the shell model is illustrated in Fig. 1. Besides these models (liquid drop & shell model) there are other nuclear models such as the collective model, geometrical model based on the underlying symmetries, which again are applicable to a certain set, type of nuclei for example deformed nuclei. Thus all nuclear models have their specific domains of success and constantly need experimental validation.

As we all know, that the nucleus being a few body system it at times manifests itself as a two body or single particle system while it also exhibits a collective behaviour. The interplay between these two extreme modes is also possible and has been the focus of several investigations, both experimental as well as theoretical, in nuclear structure endeavors. When we refer to a collective behaviour it signifies that the system of nucleons have collectively / coherently responded to an external stimulus provided by us. Similarly, a single particle behaviour, is suggestive of the participation of one or small number of nucleons to the external stimulus provided by us. The external stimulus, could be additionally imposed excitation energy, rotation of the system or an imbalance in the number of nucleons (iso-spin). Conventionally an excited (in terms of energy) and rapidly rotating nucleus is formed, in a heavy-ion fusion reaction, which then de-excites following

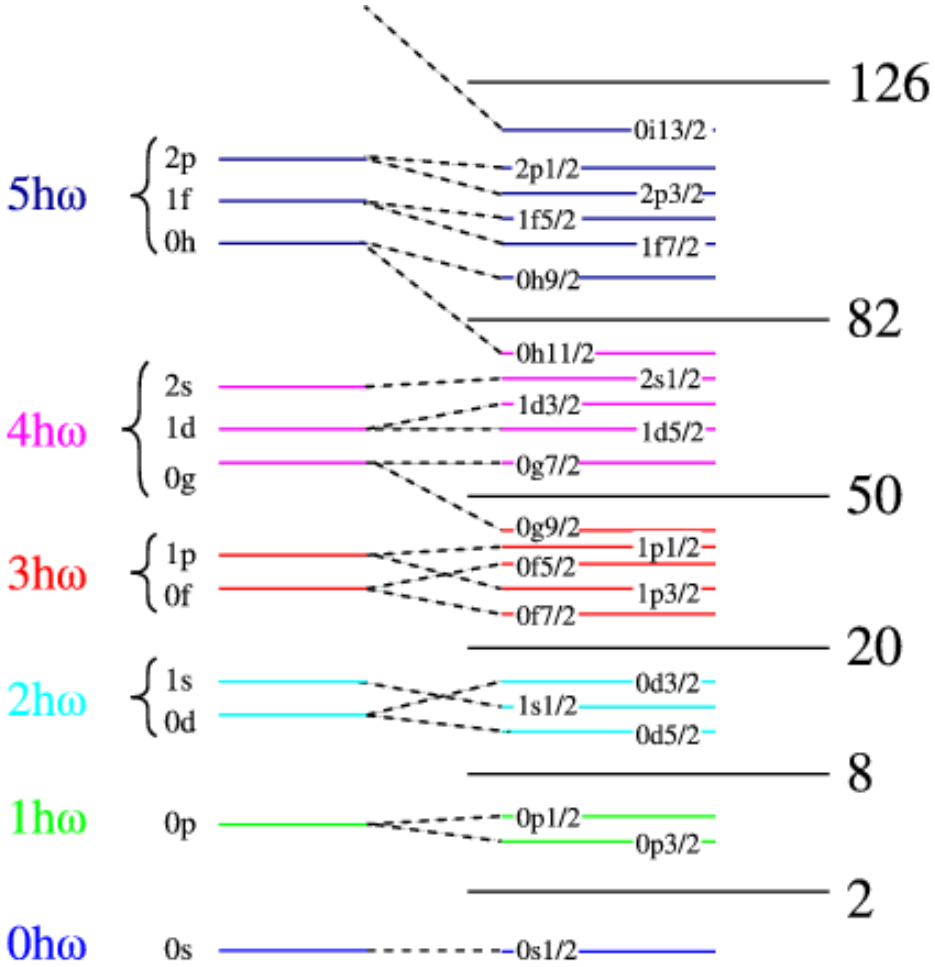

FIG. 1: The nuclear shell model energy levels. (This figure is taken from the internet).

1. particle emission

2. sequence of γ-rays.

The particle spectrum, usually helps infer about the formation probability of the various nuclei and the emitted particles energetically cools down the nucleus, as it helps the excited compound nucleus primarily loose it's excitation energy, and forms the residual nucleus. As a rapidly rotating residual nucleus de-excites to it's ground state via the emission of photons (which help the nucleus loose it's imposed angular momentum), provide us with the experimental signature on the two aforementioned extreme degrees of freedom. The detailed information during the emission of the photons (such as the γ-ray energy, their genetic relation /hierarchy) is experimentally

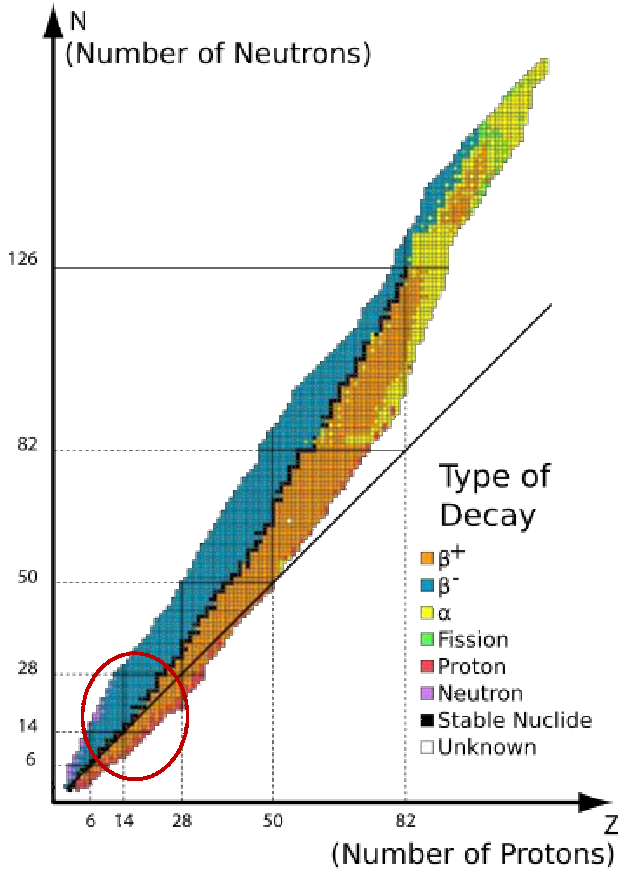

FIG. 2: The N v/s Z *plot*. The different decay mode of nuclei depicted by different colors. The region of our interest is depicted by red circle. (This figure is taken from the internet).

preserved and used to construct the decay pattern. A regular decay pattern is indicative of a collective behaviour of the nucleus under study, while an irregular decay pattern is the finger print for a single particle behaviour. The experimental level scheme is then compared with the model predictions, to have an into the underlying microscopic configurations.

The shell model perceives the nucleus as an inert core with the valence nucleons distributed in the orbitals usually within one major oscillator shell. Hence, if one were to consider the ^{26}Mg nucleus ($Z = 12,\ N = 14$), then this nucleus could be visualized as

$$^{26}Mg =^{16} O + 4\pi + 6\nu \tag{4}$$

$$^{26}Mg =^{16} O + \pi(s_{1/2}, d_{3/2}, d_{5/2})^4 + \nu(s_{1/2}, d_{3/2}, d_{5/2})^6 \quad (5)$$

Conventionally, one identifies the group of nuclei, by the orbitals which are available to the valence nucleons. Hence one would refer to ^{26}Mg as an $sd-pf$ nucleus, since valence nucleons in the ground state occupy the *sd* orbitals, where as the negative parity levels would require the occupation of the $f_{7/2}$ orbital. Traditionally, one uses the $N-Z$ plot to represent the nuclear landscape, which is presented in Fig. 2. The region of interest is appropriately highlighted by red circle. Recently, the main impetus for investigation of the structure of neutron rich $sd-pf$ nuclei, was the observation of the *"island of inversion"*, a group of nuclei, which exhibit the dominance of deformed structures at considerably lower excitation energies than their spherical counterparts, which naively one would have expected to be dominant at such low energies. Nuclear structure properties of nuclei at the interface of the $sd-pf$ shells have been the subject of contemporary interest [7–10] and Fig. 3 illustrates the family of such nuclei. These nuclei occupy a very important region in this landscape, as they are positioned mid-way between the valley of stability ($N \sim Z$) and the *"island of inversion"*. The level structure of nuclei in the around the valley of stability, is expected to be dominated by single particle excitations. On the other hand, as established recently, deformed structures dominate the level structure of nuclei belonging to the *"island of inversion"*. Hence, it would be of interest to probe the nuclear structures as one proceeds from the valley of stability, on to the island of inversion, through the transitional region, which is expected to have an influence / confluence of both these degrees of freedom.

The positive parity states in these nuclei could be generated due to the excitations of the valence nucleon within the *sd* shell itself. However, there is a possibility that the higher excited states could originate due to the occupation of the *fp* shell by two valence nucleons. Similarly, the negative parity states could only be generated by the excitation of atleast one nucleon into the *fp* shell. It well known that the $f_{7/2}$ orbital ($l = 3$) is a deformation favoring orbital, due to it's high l value. At the same time, these mid-shell nuclei, have enough valence nucleons in the *sd* shell to favor deformed structures [11]. There is a possibility for a synergy between these two deformation favoring conditions, which could result in the observation of deformed structures along with single particle excitations in these nuclei.

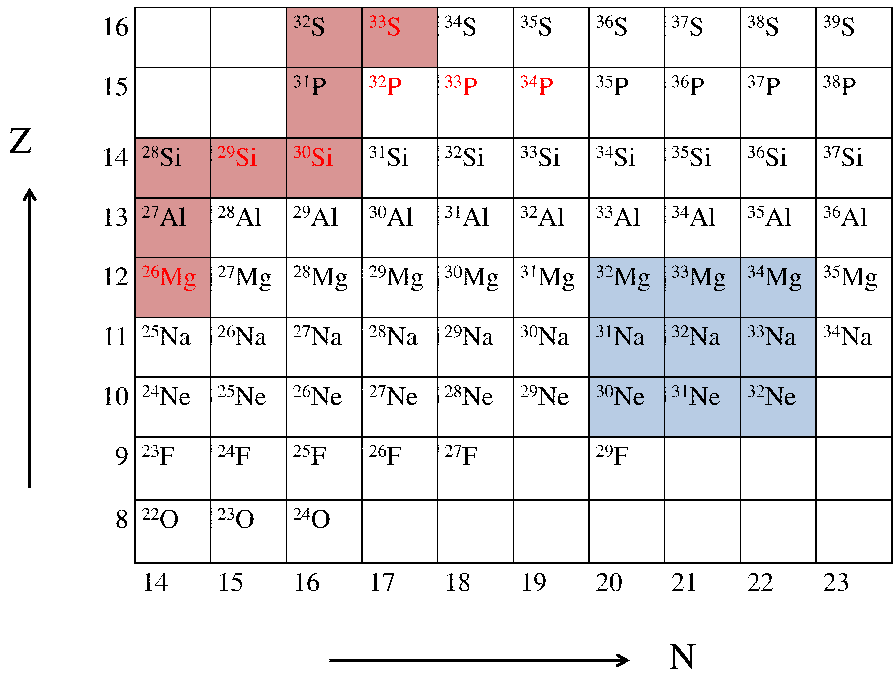

FIG. 3: The figure highlights the portion of N v/s Z plot relevant to the present study. The pink portion of the plot corresponds to the line of stability and blue region corresponds to *"island of inversion"*. The nuclei that has been studied by our group are shown by red color.

Following these considerations nuclei such as ^{26}Mg, ^{28,29}Si etc (this region on the $N - Z$ plot is rendered in the Fig. 3) are seen as the interesting candidates for these investigations. An investigation of the detailed level structure of these nuclei would include determination of the level energy, spin, parity, lifetime etc. Most of the previous studies in these nuclei have been carried out using light ion beams and modest detector setups [12, 13]. In the present thesis work we have used heavy-ion induced high resolution γ-ray spectroscopic techniques to populate and investigate the level structure of these transitional nuclei. We have employed all the text-book tools and techniques prevalent in γ-ray spectroscopy in these endeavors to arrive at a detailed information on the observed level structure of these nuclei.

As mentioned earlier the previous measurements were carried out with modest detector setups [12, 13], and as a consequence there is a considerable amount of uncertainty in the reported measurements. As an example in ^{29}Si, the lifetime of

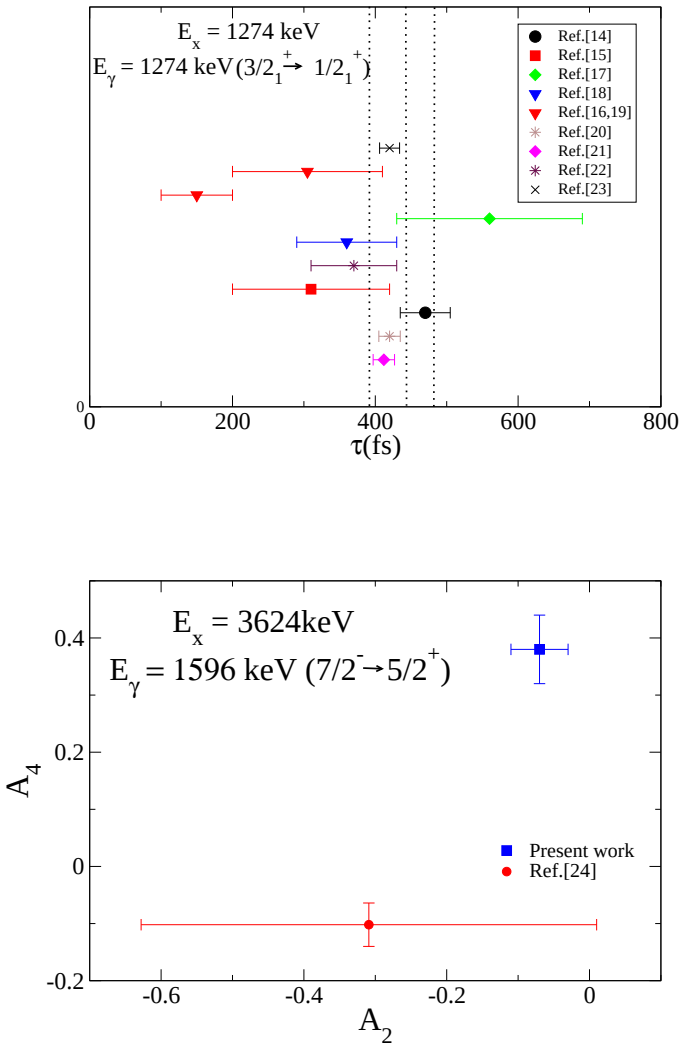

FIG. 4: (Upper panel) The level lifetimes of the 1274 keV ($J^\pi = 3/2^+$) state in the ^{29}Si nucleus from earlier measurements. The results from the present measurement are also included (see text for details). (Lower panel) Angular distribution coefficients for the 1596 keV ($7/2^- \rightarrow 5/2^+$) transition in the ^{29}Si nucleus from the earlier and the present work.

the 1274 keV ($J^\pi = 3/2^+$) level, the first excited state, has been reported by the several researchers [14–22] and have been duly adopted in the NNDC [23] database but they indicate considerably deviations in the central value, with a few of them even having a substantial amount of uncertainty, as illustrated in Fig. 4. Similarly, the multipolarity and the electro-magnetic assignment of the 1596 keV transition, de-exciting the lowest negative parity state (3624 keV, $J^\pi = 7/2^-$), has been in-

vestigated in a previous study [24] carried out with a NaI(Tl) scintillator detector, with the concomitant large uncertainties on the angular distribution coefficients (Fig. 4). This is not a desirable situation, since the negative parity levels in the $sd-pf$ nuclei are of significance as they originate from cross-shell excitations. In particular, probing the lowest negative parity level in these nuclei may provide an indication to the $sd-fp$ shell gap and requires determination of the associated measurables.

This region also provides an excellent testing ground for the spherical shell model calculations. With the availability of updated two-body matrix elements and high computing capabilities, sufficiently large basis spherical shell model can be undertaken which are expected to give an insight into the important underlying microscopic configurations. The large basis shell model calculations are also expected to help us probe the deformation characteristics which are duly expected in these mid-shell (transitional) nuclei.

The thesis reports the results of the investigation on the nuclear structure of transitional nuclei at the interface of the sd and pf shells *viz.* ^{26}Mg, ^{29}Si. The excited states of these nuclei have been populated by using heavy-ion induced fusion-evaporation reaction and their γ-decay studied thru $\gamma-\gamma$ coincidences using a large array of high resolution γ-ray detectors. The level structures of these nuclei have been extended based on measurement of the (i) level energies and intensities, (ii) angular anisotropy and (iii) polarization asymmetry of the γ-ray transition. The latter two measurements elucidate the multipolarity and electro-magnetic nature of the de-exciting γ-rays, thus facilitating assignments of the spin-parity to the observed levels. An analysis of the observed Doppler shapes and shifts for the γ-rays from transitions, following their emissions, while the recoiling nuclei slow down in the target and backing medium, allowed for extraction of the level lifetimes using the Doppler Shift Attenuation Method (DSAM). Large basis shell model calculations involving cross-shell excitations (outside the ^{16}O), have been attempted for the first time in these nuclei. The model predictions are in agreement with the experimental observations. Attempts have been made to investigate the deformation characteristics observed in these mid-shell nuclei, using the large basis spherical shell model calculations, which indeed reproduced qualitatively, the observations, such as the intrinsic quadrupole moment, large value of transition

probabilities, which are usually associated with deformed structures.

The thesis consists of the following chapters -

Chapter One : This introductory chapter introduces to the reader the motivation for the present endeavor, and establishes the canvas pertaining to the present study.

Chapter Two : This chapter presents briefly the operational principles and characteristics of electro-magnetic radiation detectors, along with an introduction to the heavy-ion fusion evaporation reactions that are used in the present work.

Chapter Three : This chapter describes the experimental setup along with the tools and techniques, (with a short outline of the underlying principles) employed for the present analysis of the recorded in-beam data.

Chapter Four : An overview of the spherical shell model, in the context of the present work, is presented in this chapter.

Chapter Five and Six : The results on the level structure of ^{26}Mg and ^{29}Si and the comparison of the observables with the predictions of the large basis spherical shell model are discussed in these chapters. The model calculations for their neighbouring isotopes are also presented to explore the systematics, for these transitional nuclei. The spherical shell model calculations have reasonably explained the observed deformation characteristics in these nuclei.

Chapter Seven : This chapter presents a succinct conclusion from these experimental and theoretical endeavours.

Chapter - 2

Experimental Details

In this chapter we shall discuss briefly about heavy-ion induced fusion evaporation reactions which preferentially populates the high spin (higher angular momentum) states in the residual nuclei of our interest. Such a rapidly rotating system decays to it's ground state following the emission of a sequence of γ-rays. These de-exciting γ-rays are detected using a large array of Compton suppressed HPGe (Clover) detectors. The chapter presents a concise discussion on the principle of detection of radiation and highlights the advantage of composite detectors such as Clover detector, in substantially enhancing the detection efficiency. The chapter also summarizes the results of the simulations for the Clover detector using GEANT4 toolkit, which are in conformity with the experimental observations.

2.1 Fusion Evaporation Reactions

The nucleus being an inert system, information pertaining to the behaviour of the constituent nucleons and their interactions can only be obtained only if we subject this system to an external stimuli, and observe the response of this system, which help us infer about it's properties. Traditionally the external stimuli imposed, is either in the form of excitation energy, angular momentum or temperature. Recently, it has been possible to extend this stimuli to another degree of freedom *viz.* increasing the N/Z (iso-spin) ratio. Heavy-ion induced fusion reactions help us conveniently subject the nucleus to an external stimulus of energy and angular momentum. Fusion is defined as the process wherein the projectile (usually a heavy-ion, heavier than alpha particle) amalgamates with the target nucleus (another heavy-ion), to form a fully equilibrated compound nucleus (CN). The major advantage of heavy-ion fusion reactions is that it results in the formation of a "hot" system, possessing both high excitation energy as well as angular momentum. The total excitation energy of the compound nucleus (CN) is given by the sum of bombarding energy in centre of mass frame and the Q

value of the reaction. The imparted high angular momentum to the system results in the population of very high spin states.

The fusion reaction occurs when two nuclei collide with a small impact parameter (at sufficiently large projectile energy to overcome the Coulomb barrier between the incoming projectile and the stationary target). The compound nucleus is a system where the equilibration in all the degrees of freedom has been attained within the time scale of $\sim 10^{-20}$s. According to Bohr's independence hypothesis the decay of such an equilibrated system into the various open (available) channels is independent of its formation history, and is governed by the conservation laws and the available phase space.

The compound nucleus (as illustrated in Fig. 5) which is excited in terms of both energy as well as angular momentum, prefers to cool-down energetically (loose it's excitation energy) via particle (α, proton and neutron) emission. The particle emission is the most efficient way to lose energy ($\sim$ 5 - 8 MeV per nucleon), however since the particle emission is along the radial direction it does not carry away significant amount of angular momentum (generally $\sim 1/2$ - 2 $\hbar$ is the loss in angular momentum following particle emission). The absence of Coulomb barrier generally favors neutron emission over charged particles such as proton or α emission. The particle emission ceases once the residual nucleus (after emission of the particles), has it's excitation energy reduced below the particle evaporation threshold.

After the particle emission the residual nucleus (which has considerable angular momentum) then de-excites, via the emission of γ-rays. Initially we have the emission of fast statistical γ-transitions (E1, which involves a change in one unit of angular momentum) which usually carry off energy and not much angular momentum. These are also referred to as quasi-continuum transitions, because the nuclear level density of these states is high and individual γ-rays cannot be resolved. After emission of statistical γ-transitions, the subsequent discrete γ-decay takes the nucleus along the *yrast line*, which represents the contour of the lowest energy for a given angular momentum state [25, 26] as shown in Fig. 6. The detailed study of these γ-rays forms the central theme of the present investigations.

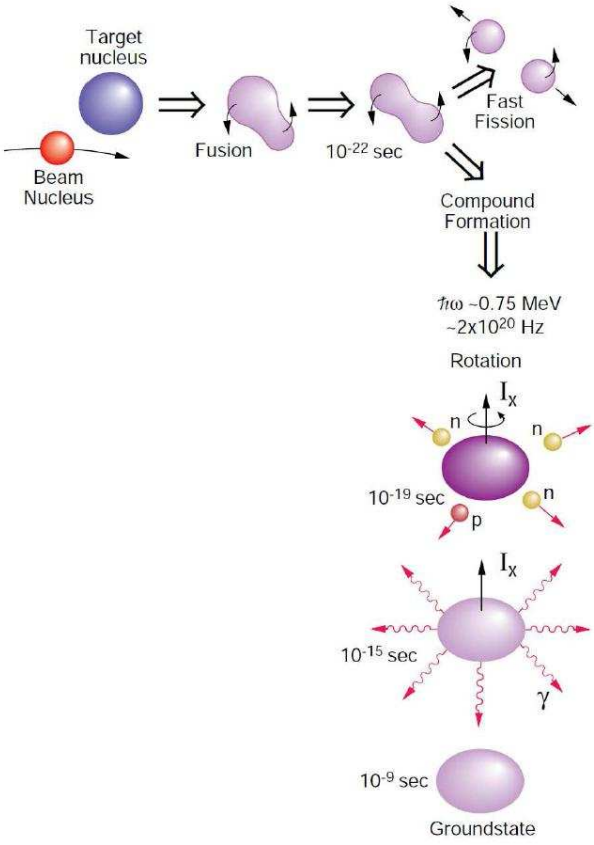

FIG. 5: The schematic diagram for formation and decay of a compound nucleus following heavy-ion fusion evaporation reaction (This figure is taken from the internet).

The crucial parameters which describe / quantify a fusion evaporation reaction would be, the Coulomb barrier, angular momentum transferred to the compound nucleus, to name a few. The Coulomb repulsion between target and projectile nuclei is represented in terms of a Coulomb barrier that can be estimated in the centre of mass frame, using the relation

$$V_c(cm) = 1.44\frac{Z_p Z_t}{R}. \tag{6}$$

Where, Z_p and Z_t are the projectile and target atomic number and R (in units of fm),

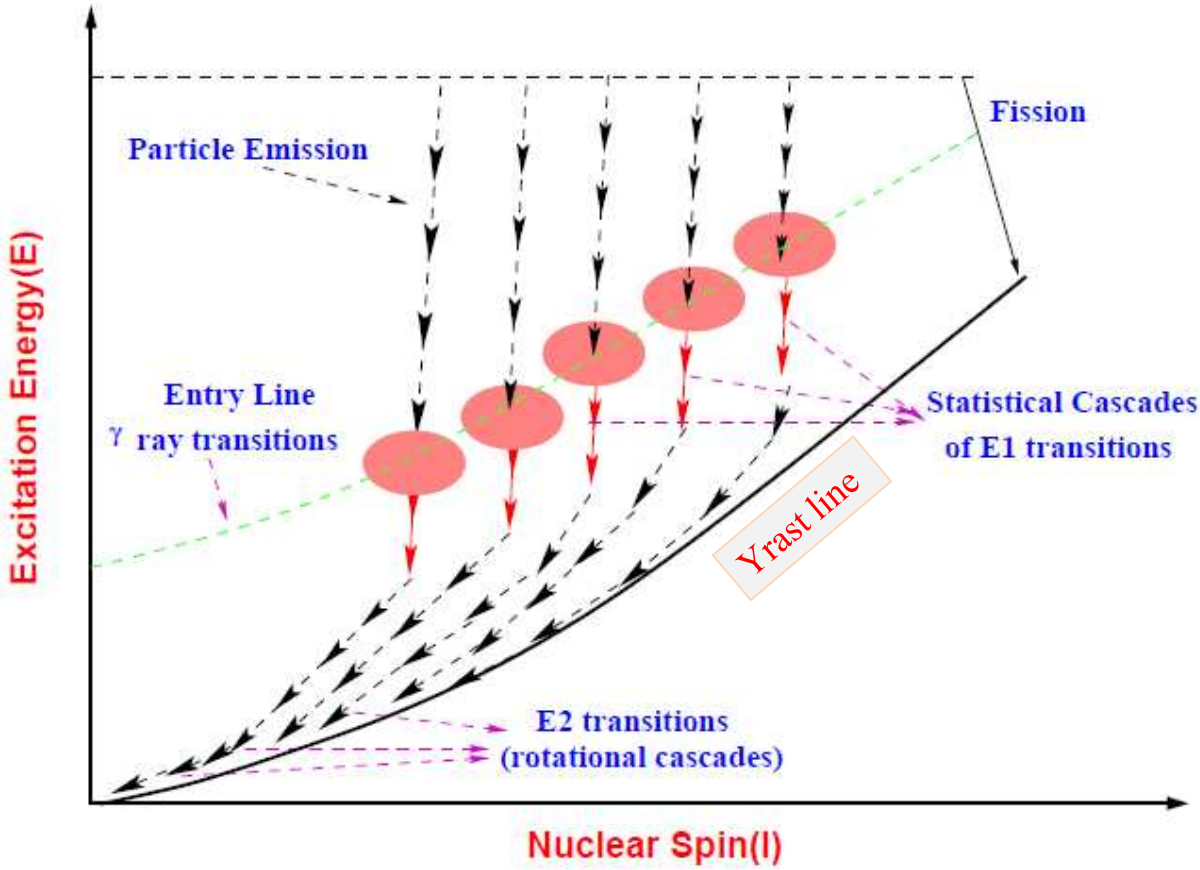

FIG. 6: Illustration for the decay paths available to a rapidly rotating compound nucleus. (This figure is taken from the internet).

is the distance between the two nuclei as they just touch each other, and is given by

$$R = 1.36(A_p^{1/3} + A_t^{1/3}) + 0.5. \tag{7}$$

A_p and A_t represents the mass number of the projectile and the target nucleus. The value of the Coulomb barrier in the laboratory frame then is obtained as

$$V_c(lab) = V_c(cm)(1 + A_p/A_t). \tag{8}$$

From the mass energy conservation the excitation energy of the compound nucleus E_{ex} is calculated using the equation

$$E_{ex} = Q + E(cm). \tag{9}$$

TABLE I: The relevant parameters such as $E(cm)$, Q, E_{ex}, R, $V_c(cm)$, $V_c(lab)$ and l_{max} for the reactions employed in the present thesis.

	Reactions	
Parameters	^{13}C + ^{18}O	^{16}O + ^{18}O
E_{lab} (MeV)	30	34
$E(cm)$ (MeV)	17.5	18.0
Q (MeV)	25.3	24.4
E_{ex} (MeV)	42.7	42.4
R (fm)	7.3	7.4
$V_c(cm)$ (MeV)	9.6	12.3
$V_c(lab)$ (MeV)	16.4	23.2
l_{max} ($\hbar$)	12	11

Where Q and $E(cm)$ are the Q value for the reaction and kinetic energy of the compound nucleus in the centre of mass frame, and are related to $m_p,\ m_t,\ m_{cn}\ and\ E_p$, the mass of the projectile, target, compound nucleus and the the kinetic energy of the projectile respectively as,

$$Q = (m_p + m_t - m_{cn})c^2\ and \tag{10}$$

$$E(cm) = E_p\left(\frac{m_t}{m_p + m_t}\right). \tag{11}$$

The maximum angular momentum (l_{max}), transferred to the compound nucleus in a fusion evaporation reaction is quantified using the equation

$$l_{max}^2 = (E(cm) - V_c(cm))\frac{2\mu R^2}{\hbar^2}. \tag{12}$$

Where, μ, is the reduced mass of the target and projectile system, and is related to the individual masses from the equation given below,

$$\mu = \left(\frac{m_p m_t}{m_p + m_t}\right). \tag{13}$$

As a part of the present thesis, two experiments were performed. Table I, summarizes the essential parameters for these reactions.

The discrete γ-transitions which are emitted by the residual nucleus along the *yrast line* and their genetic relationship help us reconstruct the level sequence for the

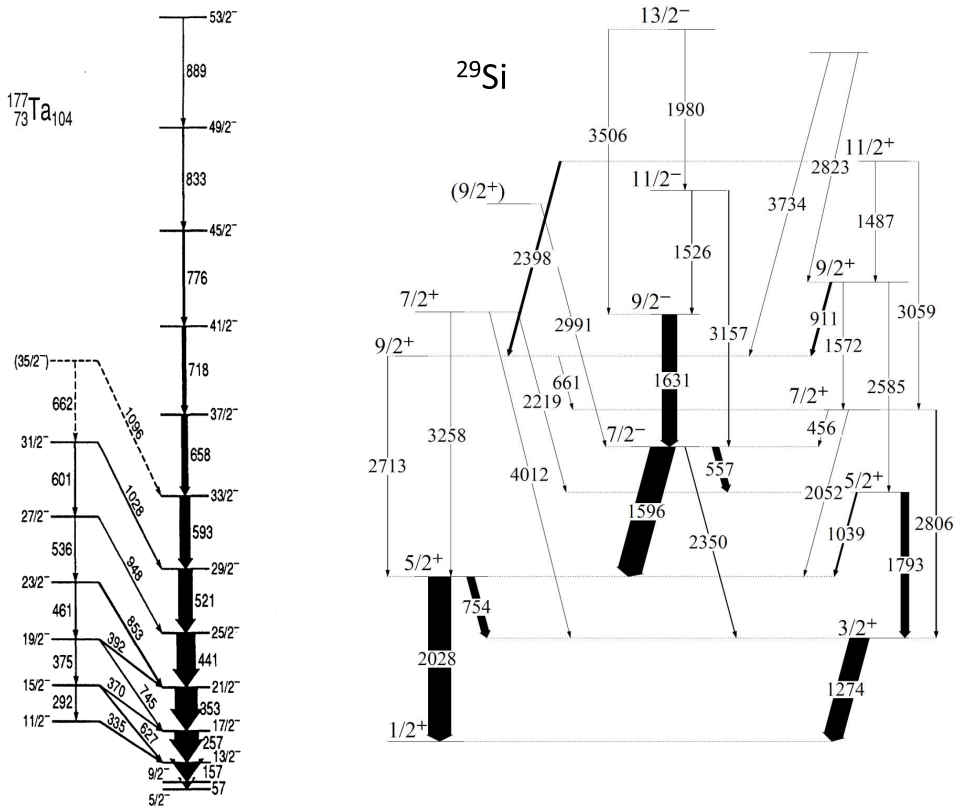

FIG. 7: (Left Panel) Example of a representative decay sequence observed in the ^{177}Ta nucleus from, where the nucleons have collectively responded to the imposed external angular momentum. (Right Panel) Example of irregular decay sequence, which is indicative of the situation wherein a few nucleons have responded to the external stimuli. This decay sequence is observed in the ^{29}Si nucleus.

nucleus as it de-excites to its ground state. This sequence is the finger print as to how the nucleons have responded to the external stimuli of angular momentum. If all the nucleons have collectively responded we obtain a regular sequence / cascade of γ-rays as shown in the left panel in Fig. 7 [27], whereas if only a few nucleons have responded to the rotation, we observe a highly irregular decay pattern as presented in the right panel of Fig. 7 [28].

Thus, it is imperative for us to have a snap-shot of each individual decay sequence. This is achieved by detecting the de-exciting γ-rays using a gamma detector array, preserving the genetic (sequential) relationship during the de-excitation process. The

relevant information (as discussed later) are stored for a detailed analysis offline, wherein we try to construct the detailed level-sequence (de-excitation path) of the nucleus of our interest. Hence all experimental nuclear structure investigations centre around the efficient and detailed detection of the de-exciting γ-rays.

2.2 Interaction of Radiation with Matter

We are able to "see" the γ-ray, without actually "seeing" it is due to the fact that it interacts with the detector medium and subsequently, deposits it's energy within the medium. There are three basis interactions / processes, whereby the incident electromagnetic radiation interacts with the detector medium, resulting in the transfer of energy either complete or partial from the radiation to the detector. These interactions are photoelectric, Compton and pair production, and have a pronounced energy and $Z_{detector}$ dependence. These interactions and the subsequent energy deposited / transferred to the detector are briefly described below.

2.2.A. Photoelectric Process

In photoelectric process a γ-photon ($E_\gamma \geq \phi$, (the work function of the detector material)) interacts with an orbital electron of the atom. The electron is emitted from the atom in conjunction, with the resulting vacancy being filled with an electronic de-excitation from higher orbit accompanied by the emission of low energy photon *viz.* $X - rays$ as shown in Fig. 8. This secondary low energy photon also under goes photoelectric absorption in the detector. Hence, these two simultaneous processes ensures, that the full-energy of the incident photon is transferred to the electron and we are able to obtain the full-energy information of the incident radiation (Fig. 8). Since, the interaction between the radiation and the detector is a purely probabilistic process, even if we were to assume ideal conditions, we would have a slight spread (uncertainty) in the energy deposited, as detailed later. The spread in the energy deposited is a combination of several factors, such as the detector resolution, electronic noise to name a few. Hence the deposited energy can be represented by a Gaussian distribution,

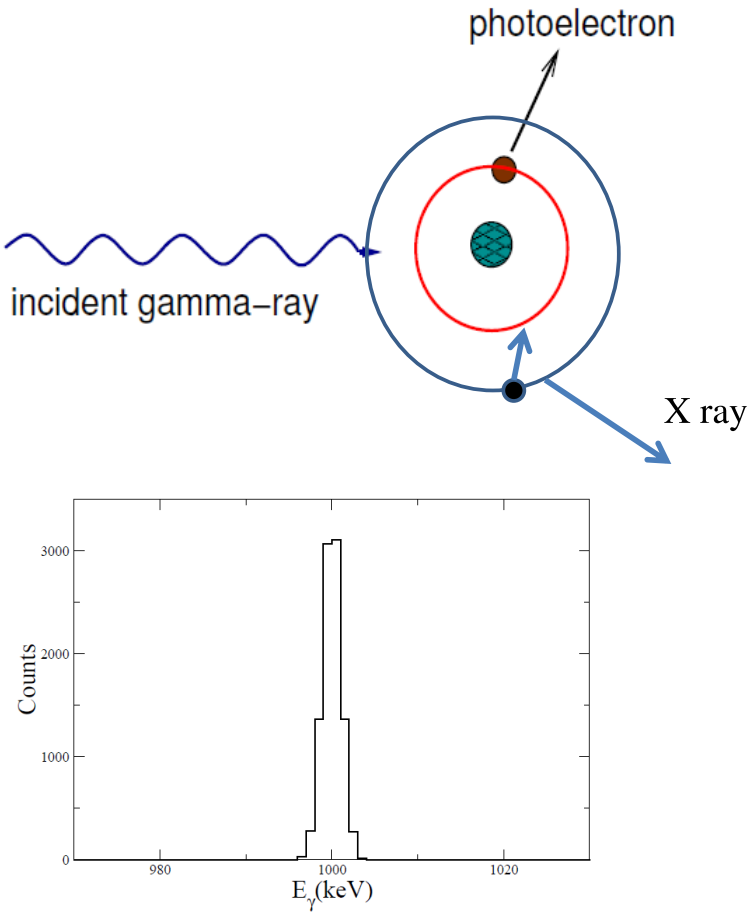

FIG. 8: Schematic diagram for the photoelectric process is shown in the upper panel and its corresponding energy deposited (E_γ = 1 MeV) within the detector is shown in the lower panel, obtained from the GEANT4 simulations wherein only the photoelectric interaction was the allowed / permitted interaction mechanism.

and it is desirable to minimize the fluctuations around the central value. The cross-section (interaction probability) for photoelectric interaction is dependent on the Z of the detector material as well as on the incident γ-ray energy E_γ, and is quantified by the equation :

$$\sigma = constant \frac{Z^{(4-5)}}{E_\gamma^3} \tag{14}$$

Thus photoelectric interaction is the most preferred interaction, since it results in a complete energy deposition from the radiation to the detector material.

2.2.B. Compton Scattering

This process occurs when the γ-photon with incident energy $h\nu_0$ collides with an electron in an atom, as shown in Fig. 9 which is treated as being at rest. The incident photon imparts a part of its energy to the electron which is then emitted along with a scattered secondary photon of energy $h\nu$. This process results in the sharing of the incident energy between the electron and the scattered photon, which manifests as a continuous energy distribution. From energy and momentum conservation the energy of the scattered photon is

$$h\nu = \frac{h\nu_0}{1 + h\nu_0/m_0c^2(1 - cos\theta)}. \tag{15}$$

Where m_0c^2 (= 0.511 MeV) is the rest mass energy of the electron and θ is the angle between the plane of the incident photon and scattered photon. The kinetic energy of the electron represents the energy difference between the incident photon and scattered photon and is given by

$$E_e = h\nu_0 - h\nu = h\nu_0\left(\frac{(h\nu_0/m_0c^2)(1 - cos\theta)}{1 + h\nu_0/m_0c^2(1 - cos\theta)}\right). \tag{16}$$

From the above equation it is clear that the energy of the electron is θ dependent. When the value of $\theta = 0^o$ then, we have $h\nu_0 = h\nu$ and in this situation, no energy transferred to the electron. Further, if $\theta = \pi$ the amount of energy transferred to the electron is maximum and the incident photon is back scattered. The maximum energy of this electron is known as "Compton edge". The energy of the back scattered γ-photon is given by

$$h\nu(\theta = \pi) = \left(\frac{h\nu_0}{1 + 2h\nu_0/m_0c^2}\right). \tag{17}$$

So from the above equation we see that the energy of the back scattered photon is minimum at $\theta = \pi$. If $h\nu_0 = 1\ MeV$ then the energy of the back scattered photon is $\sim 200\ keV$, and hence the energy deposited in the detector is around 800 keV. Thus even at the "Compton edge" (which corresponds to the maximum energy deposited following a Compton interaction) the energy does not correspond to the full-energy of the incident radiation. As all scattering angles between $\theta = 0^o$ to $\theta = \pi$ are allowed and as a consequence the energy spectrum following Compton scattering is continuous distribution. The Compton scattering cross-section is independent of the atomic

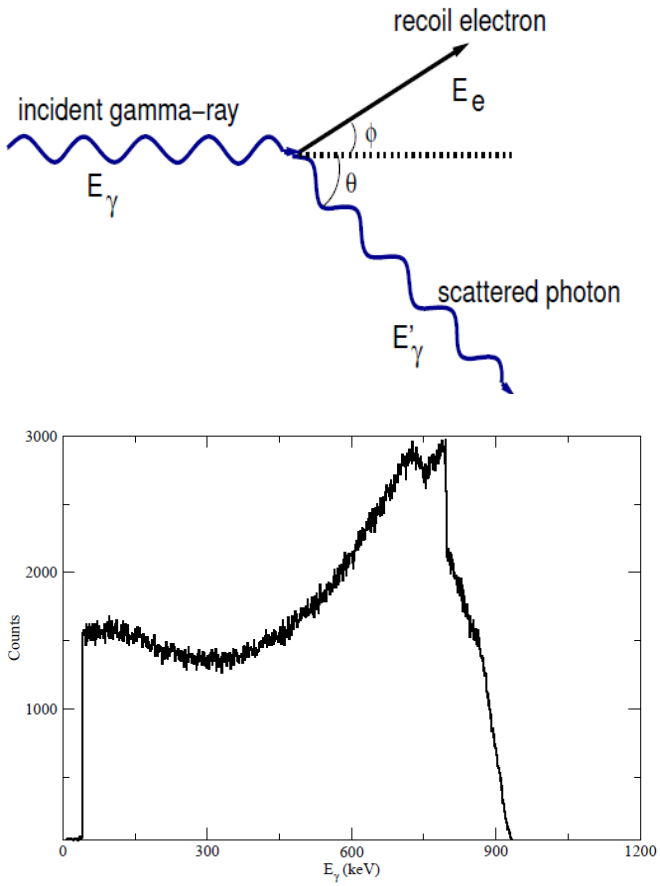

FIG. 9: Schematic diagram for the Compton scattering process is shown in the upper panel and its corresponding energy spectra (for $E_\gamma = 1$ MeV), simulated using the GEANT4 toolkit, with Compton interaction as the only permissible interaction is shown in the lower panel.

number of the material of the medium and has an approximate constant cross section at energies of interest ($E_\gamma \leq 4$ MeV). Thus, this process is the most dominant process at photon energies of our interest.

2.2.C. Pair Production

When the incident energy (E_γ) of the electro-magnetic radiation is ≥ 1.02 MeV (twice the rest mass energy of electron or positron) then it may interact via pair-

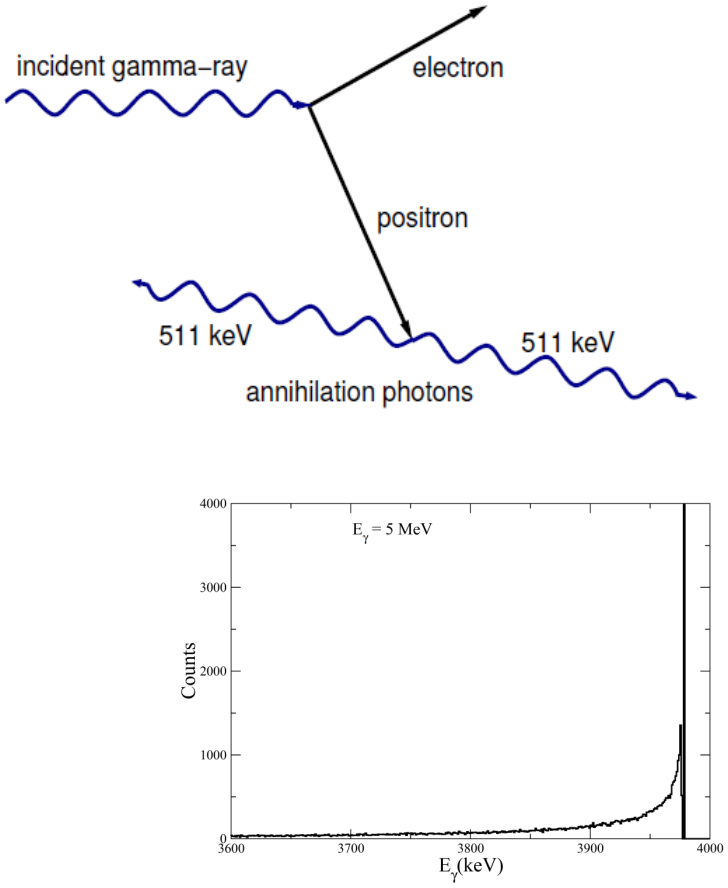

FIG. 10: Schematic diagram for the pair production process is depicted in the upper panel and the energy deposited in the detector (for $E_\gamma = 5$ MeV), following the pair-production interaction (using GEANT4 simulation toolkit) is illustrated in the lower panel.

production. For this process the presence of an atomic nucleus is essential, to ensure conservation of both the energy and momentum. In this interaction, the energy of the incident radiation is used to create an electron and positron pair. The excess energy is imparted as their kinetic energy. The annihilation of the positron results in the formation of two γ-rays each with E_γ = 511 keV. If one of the annihilated photon escapes from the detector, then we observe a peak at E_γ - 511 keV and this termed as "single escape peak". If the both the annihilated photons escape out of the detector then the resultant peak is observed at E_γ - 1.02 MeV and is termed as double escape peak. However, it is observed that this interaction is of relevance only at $E_\gamma \geq 4$ MeV

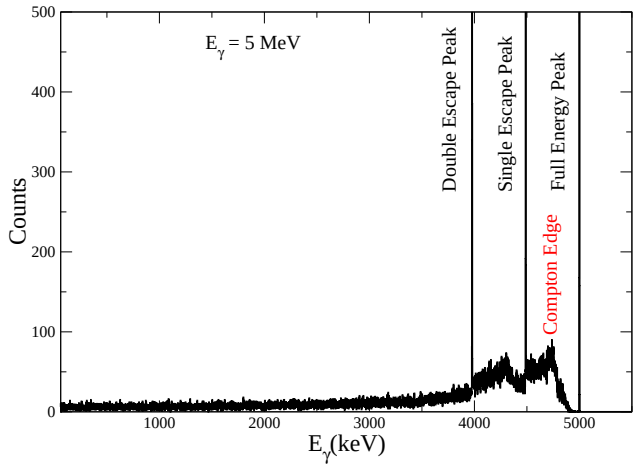

FIG. 11: Representative energy deposition within the detector for an incident photon with E_γ = 5 MeV (using GEANT4 simulation toolkit).

and the pair production cross section is proportional to Z^2 (atomic number). Hence, following this interaction, the energy deposited in the detector would correspond to $E_\gamma - 1.022$ MeV, as depicted in Fig. 10.

The interaction of the incident γ-ray with the detector material, finally culminates in the observation of the energy spectrum presented in Fig. 11. As is evident from the figure, we observe, the characteristics full-energy, and escape peaks along with their corresponding Compton Edge. Thus the interaction of the radiation results in a transfer of energy from the incident radiation to the detector material. This is then converted into a proportional electrical signal, which encodes the signature(s) of the incident radiation. Hence, a radiation detector, is a "transducer", which converts the incident radiation into an equivalent and measurable electrical signal.

2.3 Radiation Detectors

The γ-rays are detected by using different types of radiation detectors such as semiconductor and scintillator detectors. These detectors have different working principles. Scintillator detectors [29] consists of scintillating material which is op-

tically coupled to a photomultiplier tube (PMT). The interaction of radiation with the scintillating material, results in the excitation the atoms or molecules of the scintillator, whose subsequent de-excitation causes light to be emitted. This light output is incident on a photo cathode, which results in the emission of electrons. The photo-multiplier tube, results in the multiplication of electrons, which forms the final electrical signal pulse. The semiconductor detector is a fully depleted reverse biased diode, which ensures that the production of electron-hole pairs as the information carriers for the incident radiation, occurs only in the presence of the radiation. Since the depletion zone has to extend to the entire active volume of the detector, and a large volume Ge crystal (typically volume of $\sim$ 100 cc) is required for efficient detection of γ-rays with $E_\gamma \sim 1$ MeV, we have to apply a substantial higher reverse bias voltage to achieve a fully depleted detector. This requires the level of impurities in the Ge crystal to be extremely low (better than 1 part in 10^{12}) and hence the name Hyper Pure Germanium (HPGe). Fabrication of a large volume crystal of hyper pure germanium till date remains a technological challenge, though not a limitation.

Ideally in case of mono energetic γ radiation fixed number of information carriers are expected to be created, so the pulse height spectrum (generated following the processing of the electronic pulse from the detector) should be represented by a delta function. Since the interaction of radiation with matter is purely statistical process, and no two interactions are expected to result in an identical energy deposition in the detector, the corresponding pulse amplitudes (assuming a full-energy deposition in the detector) would exhibit a fluctuation around the mean value. The energy spectrum could be represented by the conventional Gaussian distribution, which would be centered around the full-energy (photo-peak) value and the Full Width at Half Maximum (fwhm) would correspond to the energy resolution at that energy.

A few important / crucial operating parameters for the radiation detectors are briefly discussed below. These are :

2.3.A. Energy Resolution

The energy resolution (R) of a detector quantifies it's ability to resolve closely lying γ radiations. The resolution of the detector depends critically on the "W" value of the material, which is the minimum energy required to produce one pair of information carrier, subsequent to the energy transfer from the radiation. For scintillator detector the "W" value is $\sim 10's\ of$ eV whereas for semiconductor detector it is ~ 1 eV. So the resulting number of information carriers per unit of incident energy for semiconductor detectors far exceeds the corresponding number for a scintillator detector. This results in an considerably superior energy resolution for semiconductor (HPGe) detectors. Typical energy resolution of a scintillator detector (NaI) is $\sim 40 - 60\ keV$ at 662 keV and the value for HPGe detector, which is traditionally reported at $E_\gamma = 1$ MeV, is $\sim 2\ keV$. Hence HPGe detectors are the preferred choice in high resolution γ-ray spectroscopic investigations. Energies closer than the energy resolution cannot be identified and hence this parameter is one of the most crucial operational parameters for a radiation detector. A convenient way of quantifying the energy resolution, is **F**ull **W**idth at **H**alf **M**aximum, which is given by

$$FWHM = 2.335\sigma. \tag{18}$$

where σ is the standard deviation for a Gaussian distribution. The $FWHM$ originates due to the statistical fluctuation in the information carriers generated, and also has a contribution from the noise in the detector and pre-amplifier. It also exhibits a $\sqrt{E}$ dependence on the incident energy, and hence the energy resolution deteriorates with an increase in the incident energy.

2.3.B. Efficiency

The efficiency of a detector is its ability to detect radiation, and is usually quantified in terms of the absolute full-energy (photo-peak) efficiency and the intrinsic efficiency. The absolute full-energy efficiency is defined as :

$$\epsilon_{abs} = \frac{Total\ no\ of\ recorded\ full-energy\ peak\ events}{Total\ no\ of\ events\ emitted\ isotropically\ by\ the\ source}. \tag{19}$$

This is a function of the detector geometry and the probability of an interaction with in the detector. The intrinsic efficiency is defined as

$$\epsilon_{int} = \frac{Total\ no\ of\ recorded\ full-energy\ peak\ events}{Total\ no\ of\ events\ incident\ on\ the\ detector}. \tag{20}$$

This is dependent on the interaction cross-section for the incident radiation on the detector material and it is independent of detector geometry. The intrinsic and absolute full-energy peak efficiency are related as,

$$\epsilon_{int} = \epsilon_{abs}\frac{4\pi}{\Omega}. \tag{21}$$

Where Ω is the solid angle subtended by the detector at the source position. In our present case a point source is located along the axis of a circular cylindrical detector and in this case the solid angle (after some simplification) is defined by the equation below,

$$\Omega = 2\pi\left(1 - \frac{d}{\sqrt{d^2 + a^2}}\right). \tag{22}$$

Where the source and detector are at a distance d apart and the radius of the detector is a. The value of the absolute full-energy peak peak efficiency of a single crystal HPGe (dimension of $\sim 51 \times 71$ mm), which have been used in the Gamma Detector Arrays such as the GDA at IUAC, New Delhi, is $\sim 2.89 \times 10^{-4}$ when the ^{60}Co source is placed at a distance of ~ 25 cm from the front face of the detector.

The efficiency of the detector is directly proportional to the detector size, since a larger detector under identical conditions subtends a larger solid angle at the target position. Hence, it is desirable to construct a larger sized detector which would correspondingly increase the detection efficiency. Difficulties will arise in increasing the detector volume (size) as discussed in below,

1. It is not easy to grow a Hyper Pure Germanium Crystal of the desired dimensions. However this technological difficulty has been over come as of now, and as such is not a major stumbling block.

2. The increase in the detector size, results in a substantial increase in the detector opening angle subtended at the target. This results in a considerable degradation

of the energy resolution of the detector which is, referred to as Doppler broadening. We know that

$$E_\gamma \propto cos\theta$$
$$\Delta E_\gamma \propto sin\theta \tag{23}$$

For a single crystal detector, to achieve a relative full-energy peak efficiency of $\sim$ 125% (with respect to a $3'' \times 3''$ NaI(Tl) scintillator) for E_γ = 1 MeV, the cylindrical detector would have a dimension of $\sim 10cm \times 70mm$. For the routinely encountered experimental situation wherein the detector is placed at an approximate distance of 25 cm, from the target, this large volume detector would subtend an opening angle of $\pm\ 7^o$. If the recoils are moving with a velocity which equals 3% of c ($\beta = v/c = 3\%$), then, due to the Doppler broadening, the $E_\gamma = 1$ MeV, would have an energy spread of about 8 keV shown in Fig. 12 this will result in a substantial deterioration of the energy resolution. Composite detectors which are configured using granular (smaller sized) detectors within the same cryostat ensures a relatively smaller opening angle, with a corresponding decrease in the degradation of the energy resolution. The increase in the detector size also results in a substantial degradation in the timing properties. In a large volume detector, the charge collection time, as expected is more compared to single crystal detector, which affects the timing properties of such large volume detectors. Further, if the charges are produced in a region of weaker / non-uniform electric field, then the collection times for these is substantially higher than the rest of the charges, often resulting in an insufficient charge collection, from such events. This further affects the timing performance, an important operational characteristics in a coincidence measurement. Therefore, the use of a single large volume detector is ruled out.

2.3.C. Clover Detector

Composite detectors provide an attractive alternative to circumvent this problem *viz.* to have a detector with higher detection efficiency, maintaining the excellent energy

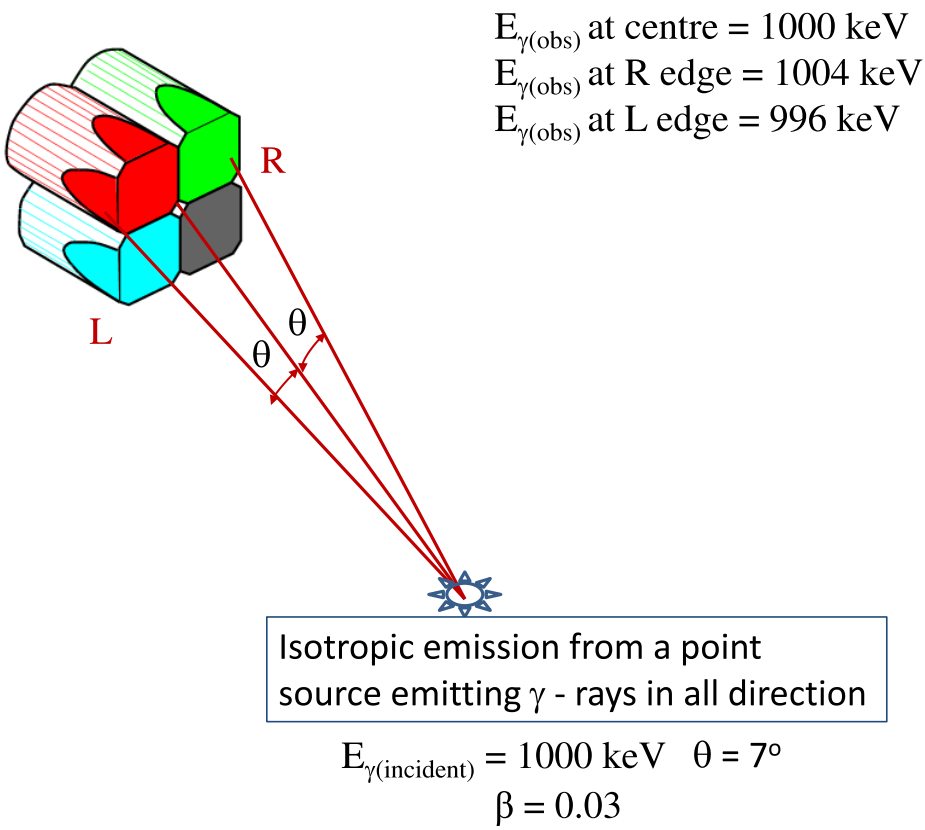

FIG. 12: Energy spread observed in a large volume single crystal detector due to the large opening angle subtended at the target.

and timing resolution. These detectors are composed of smaller single-crystals, housed in a common cryostat. Since the crystals are physically separated, they present a much smaller opening angle and hence reduce the Doppler broadening effect. Compton scattering being the most dominant interaction at energies of relevance, the partial γ-ray energy deposited within the individual crystals, due to Compton scattering, could then be summed up appropriately, if they are time correlated, to recover the full-energy of the incident γ radiation. Thus the crystals together provide a very large "effective" volume, without any increase in the detector opening angle, and thereby increasing the total detection efficiency. The smaller sized individual crystals do prevent any deterioration in the timing properties. However, the major advantage of the Clover detector is that the it allows us to perform linear polarization measurements (which are discussed in details in the subsequent chapters) to uniquely obtain the information on the electro-magnetic nature of the transition. Hence, the Clover detector

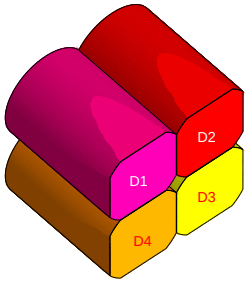

FIG. 13: Geometrical arrangement of the crystals in a Clover detector.

forms the main workhorse for most of the present day gamma detection systems [30–32].

Since, the Clover detector has been extensively used in the present endeavors, it is of interest to simulate it's performance and understand it's operational parameters. The characteristics of the Clover detector *viz.* the add-back factor, efficiency to name a few have been experimentally established [31–34]. As a part of the present thesis, an attempt was made to simulate these using the GEANT4 [35] toolkit. These simulations are expected to corroborate the experimental observables, besides helps us in energy domains which are inaccessible using conventional radio-active sources. The Clover detector has a complex geometry for the individual single crystals. For example, the bevels at the front edge generate a semi-elliptical surface. The other two sides of each crystals are mostly flat to allow for a close packing of the adjacent crystals. Thus, the front face of the crystal has a quasi-square shape while its rear face is quasi-circular in shape.

In the present simulations, the complex geometry and shape of the crystals, was successfully reproduced using a simplistic geometrical approximation. The shape was arrived at through a Boolean operation of a box, trapezoid and a cylinder, so as to conserve the volume at $\sim$ 118 cc (the actual volume of the individual crystal) as presented in (Fig. 13). The crystals, were housed in an Al casing of thickness of 1.5 mm, and the front face of the crystals was positioned at a distance of $\approx$ 4 mm inside the casing. The inter crystal spacing was $\approx 4 - 5\ mm$, with the source to detector (front face) distance of 25 cm.

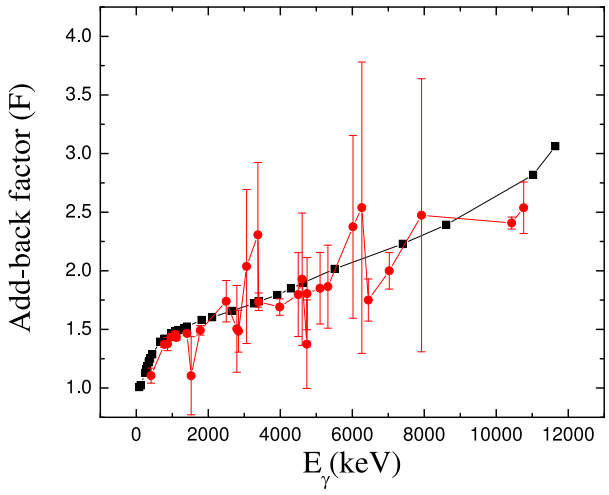

FIG. 14: Variation of the add-back factor as a function of the incident γ-ray energy. The line connecting the points is drawn to guide the eye.

In the add-back mode, the summation of time correlated Compton scattered events results in the recovery of full-energy information. Hence in this mode, we observe an increase in the number of full-energy events in comparison with a single crystal, where such events contribute to the Compton background. This enhancement in the detection efficiency is quantified using the parameter, "add-back factor" (F), which, for a given energy, is defined as

$$F = \frac{full - energy - peak - counts\ in\ add - back\ mode}{\sum_{i=1}^{4} full - energy - peak - counts\ in\ crystal(i)}. \tag{24}$$

The add-back factor F, has been experimentally determined up to $\sim$ 12 MeV [31–34, 36]. The comparison of the experimental and simulated add-back factor as a function of E_γ is presented in Fig. 14, which indicates an excellent conformity between the two. The points with error bar denotes the experimental values are taken from Ref.[31, 32].

The F factor, for $E_\gamma = 1332$ keV, is measured to be be typically 1.56 ± 0.03 [34] and the simulated value has been found to be 1.51, which represents a reasonable agreement. The F-factor is typically $\sim$ 1.15 upto $E_\gamma = 275$ keV. This indicates that there is no additional gain in the full-energy efficiency of the Clover, in the add-back mode, at these energies, beyond what is obtained from the simple summation of the individual crystal information. This is because at low energies, the photoelectric absorption is

the dominant interaction compared to the Compton scattering, hence most of the low energy γ-rays deposit their full-energy within a single crystal, with a minimal scattering into the neighbouring crystal. Above 250 keV, the F-factor varies linearly with E_γ up to $\sim$ 4 MeV, beyond which there is a sharp increase in the F-factor up to about 12 MeV. The initial linear increase in this factor with energy ($250\ keV \leq E_\gamma \leq 4000\ keV$) may be attributed to the significant contribution from the Compton scattering which is expected to be the dominant mode of interaction at these energies. At $E_\gamma = 1000$ keV, for Ge the attenuation coefficients for photoelectric and Compton processes are 0.0007 cm^2/g and 0.0565 cm^2/g respectively indicating the expected dominance of Compton interaction in this energy regime. Above $E_\gamma = 4$ MeV, the pair-production, which may also represent partial energy deposition in multiple crystals of a Clover detector, is expected to contribute significantly. At $E_\gamma = 5.0$ MeV, for Ge the attenuation coefficients for photoelectric, Compton and pair-production processes are 5.52×10^{-5} cm^2/g, 0.022 cm^2/g and 0.0095 cm^2/g respectively. A synergy between these two processes *viz.* Compton and pair-production, with the contribution from Compton scattering having a nearly constant energy response, results in an appreciable gain in the add-back mode of the Clover for $E_\gamma \geq 4$ MeV. At $E_\gamma = 20$ MeV, the predicted F factor is 4.1, which is supported by the measurement of M. Lipoglavšek and co-workers [30].

Hence, the reasonable agreement between the predicted and experimental F factor as a function of E_γ presents a yard-stick for the modeled shape and the simulation philosophy. It is expected that these endeavors would help us comprehend the operational features of these composite detectors and help in our future (subsequent) array design.

2.4 Compton Suppression

We know that Compton scattering dominates at energies of relevance. This interaction results in a partial energy deposition in the germanium crystal, thus generating a Compton tail in the recorded energy spectrum. If one were to use a composite detector, some of the Compton scattered events are recovered in the add-back mode,

to yield the full-energy information. A further reduction in the Compton background is obtained if one were to place a Compton suppression shield (also referred to as Anti Compton Shield (ACS)) around the Clover detector, and demanding an anti coincidence between the primary HPGe signal and the Compton shield, ($HPGe.\overline{ACS}$). It is worth mentioning that while the Compton suppression procedure rejects the Compton scattered events, that are not recorded in the data, whereas the add-back technique reconstructs such events into the full-energy information.

During the simulations, the Anti Compton Shield was modeled by using a Boolean operation with a box and a trapezoid. The simulations did not include the scintillation and photo-multiplication process, which do not contribute critically to the Compton suppression. Hence the simulations are expected to be in qualitative agreement with the experimental observations, which indeed is the case. In Fig. 15 the experimental spectra for a Compton suppressed Clover is compared with the simulations for (a) single crystal (b) sum mode (time uncorrelated) (c) add-back mode (time correlated), and the agreement between the two is reasonable. The simulated P/T ratio for single crystal (Compton suppressed Clover) was obtained as 0.23 and in the add-back mode it was 0.45, which are in agreement with the reported experimental results of 0.22 and 0.44 respectively. As seen from Fig. 15, the add-back results in the recovery of the partial energy events originating from multiple Compton scattering into the total (photo-peak) energy. The two *"rabbit-ears"*, corresponding to the Compton edge for the 1173 keV and 1332 keV are distinctly visible in the *"add-back"* spectrum (Fig. 15). Thus the Compton suppression helps us reduce the background, which in turn helps us detect weak full-energy events, which otherwise would have been buried under the Compton continuum.

Thus a Compton suppressed Clover detector forms the integral part of a modern high efficiency gamma detection system. Since we have to preserve the genetic relationship between the de-exciting γ-rays, we require an array of detectors, to record the sequential decay path of the de-exciting nucleus, the detailed philosophy followed is presented in the subsequent chapters.

The Indian National Gamma Array (INGA) [37, 38] comprises of a large number

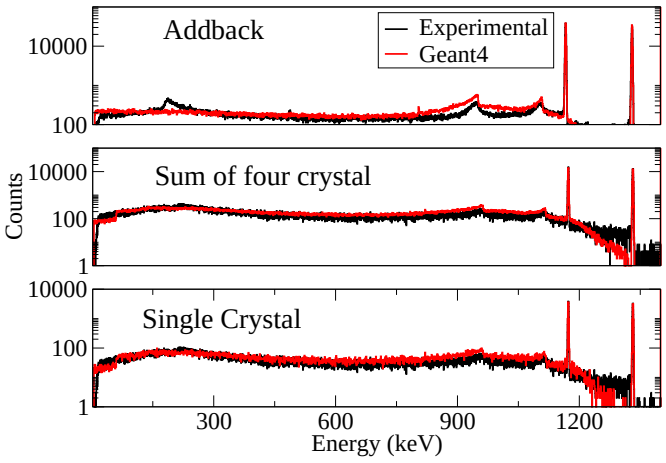

FIG. 15: Comparison of the simulated (depicted in red) and experimental (depicted in black) spectra using ^{60}Co source in single crystal, add (time unco-related summation) "add-back" (time co-related summation of events) mode. The source to detector distance is 25 cm.

(15-18) of Compton suppressed Clover detectors and the experimental investigations in the present thesis have been undertaken using this state of the art facility.

2.5 The Indian National Gamma Array

The Indian National Gamma Array (INGA) set up (shown in Fig. 16) for use in the Indian accelerators and has been successfully used for over a decade. INGA resulted from a collaboration of the University Grants Commission - Department of Atomic Energy, Consortium for Scientific Research, Kolkata Centre, Tata Institute of Fundamental Research, Inter University Accelerator Centre, Bhabha Atomic Research Centre, Saha Institute of Nuclear Physics, Variable Energy Cyclotron Centre and several Universities across the country. The Indian National Gamma Array consists of large number of Compton suppressed Clover detectors. The Clover detectors are placed at different angles with respect to the beam direction and thus allow us to record the angular anisotropy of the γ-rays which helps in the assignment of the dominant multipolarity of the de-exciting γ-ray, as well as in the extraction of the level lifetimes. Whereas, the Clover detectors at 90^o are useful for the linear polarization mea-

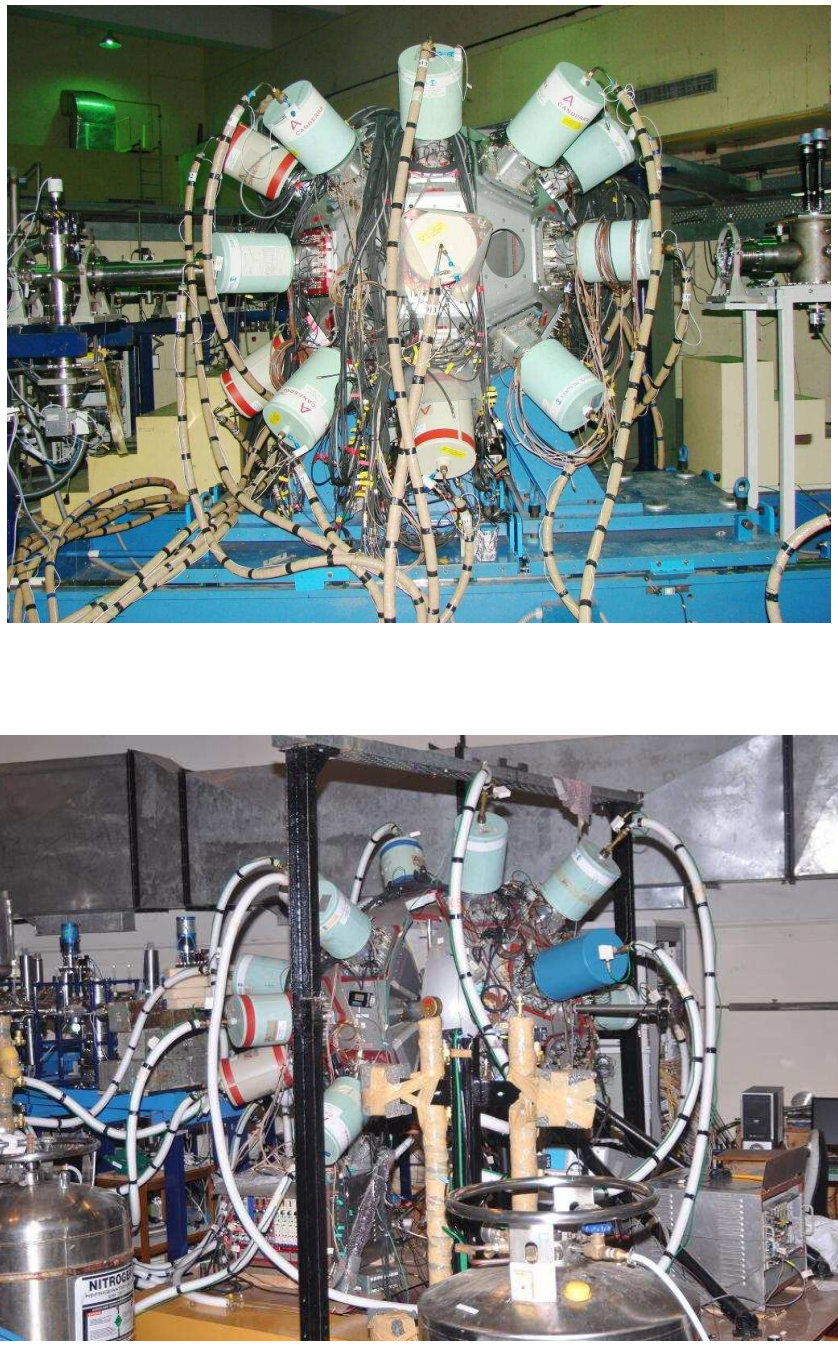

FIG. 16: Pictorial view of Indian National Gamma Array (INGA) at IUAC New Delhi (upper panel) and TIFR, Mumbai (lower panel).

surements, which yield unique information on the electro-magnetic nature of the γ-rays.

The first experiment for the present thesis work was undertaken using the ^{18}O(^{16}O,xnypzα) reaction. The ^{16}O beam at an incident energy of 34 MeV was delivered by the 15UD Pelletron at the Inter University Accelerator Centre (IUAC), New Delhi. The target to detector distance was $\sim$ 25 cm. At the time of the experiment, the array comprised of 18 Compton suppressed Clover detectors. Three of these detectors were placed at $\theta = 32^o$, four were at $\theta = 57^o$, five were at $\theta = 90^o$, three were at $\theta = 123^o$ and three were at $\theta = 148^o$ with respect to the beam direction. The expected total full-energy peak detection efficiency for this configuration was $\sim 5\%$.

The second experiment for the present thesis work was undertaken at the BARC-TIFR Pelletron Linac facility at Mumbai. The reaction used was ^{18}O(^{13}C,xnypzα) at an incident beam energy of 30 MeV. At the time of the experiment, the array comprised of 15 Compton suppressed Clover detectors. Three of these detectors were placed at $\theta = 40^o$, two were at $\theta = 65^o$, four were at $\theta = 90^o$, two were at $\theta = 115^o$, two were at $\theta = 140^o$ and two were at $\theta = 157^o$ with respect to the beam direction. The expected total full-energy peak detection efficiency for this configuration was $\sim 4\%$.

The list-mode data, an event by event information was recorded online, which was then subjected to a detailed offline analysis (as detailed in the subsequent chapters) to develop the level scheme of the nucleus of interest, which established the detailed decay sequence / pathway of the excited residual nucleus to it's ground state.

Chapter - 3

Data Reduction and Analysis

In this chapter we shall attempt to discuss briefly, some of the experimental details, such as the schematic of the electronics set up to acquire the $\gamma-\gamma$ coincidence data. The details of data analysis tools and techniques for example calibration and gain matching would also be presented. The sorting of the coincidence information into the $E_\gamma - E_\gamma$ matrices (symmetric and antisymmetric) and their application in the subsequent data analysis is also outlined. The theoretical aspects underlining the measurements such as angular distribution, polarization and lifetime measurements are also briefly touched upon.

3.1 Electronics for $\gamma - \gamma$ Coincidence

A rapidly rotating residual nucleus is populated following fusion evaporation reaction, which de-excites by emission of a cascade of discrete γ-ray transitions, that is atleast two or more γ-ray transitions are in coincidence with in very small interval of time, assuming the absence of any long lived isomeric state ($\tau \sim 100's$ of ns), between them. This de-excitation pattern (decay sequence) encodes the finger print(s) for the response of the nucleons (nucleus) to the imposed stimulus of angular momentum and reveals the interaction between the constituent nucleons. Hence, it is crucial that we faithfully reconstruct this decay sequence from the recorded data, an exercise which is analogous to the solution to a conventional cross-word puzzle. Just as in a cross-word puzzle two clues are required to arrive at an unambiguous solution, we require that atleast two γ-rays are observed in prompt coincidence (within say 200 ns) to reconstruct the decay-sequence. This coincidence condition, referred to as the *Master Gate* is usually set in the hardware during the implementation of the pulse processing electronics along with the data acquisition system. A signal corresponding to $HPGe.\overline{ACS}$ is generated from each Compton suppressed Clover, which indicates that the energy deposited in the Clover detector does not originate from a Compton event.

This signal being a conventional NIM signal has an amplitude of about 50 mV, with a pulse duration of around 200 - 300 ns. These signals from the individual detectors are then used as inputs to an analog adder circuit, whose output is proportional to the number of Compton suppressed Clovers which have non-zero data (this is also referred to as *Clover Multiplicity*). For example if two detectors have recorded data, then the output of this module would be $\sim$ 100 mV, whereas in case of a triple coincidence, the value would be $\sim$ 150 mV. This analog sum is the used as the input to a discriminator, whose threshold can be adjusted to obtain an output when the desired Clover Multiplicity is achieved [37]. For example, if we desire a two-fold coincidence between the Clovers, then the threshold is set at $\sim$ 75 mV, resulting in an output when we have atleast two Clovers firing simultaneously. The schematic representation of this pulse processing philosophy using the conventional analog electronics is presented in Fig 17. This output then is used to generate a *Master Gate*, the signal which validates that the given event has satisfied the experimental conditions, and we can record or store these non-zero energies. We also record the individual Clover timings with respect to some reference, which is usually the Master Gate. The data acquisition for one of the experiments was configured using CAMAC systems as the interface standard. The electronics consisted of the indegeniously developed Clover module at IUAC, New Delhi Ref.[37].

Thus the aim of the pulse processing methodology, is to extract the information regarding the energy of the detected γ-ray, its arrival time with respect to a reference, to name a few. We would also like to suppress unwanted events, *ie.* events which do not qualify our experimental requirements such as Compton scattered events, low multiplicity events, such as singles, etc. and then to compress information from valid events in a compact format, which saves both disk space and pre-sorting time, this was achieved using a combination of the conventional NIM analog electronics for pulse processing and CAMAC or VME as the interface standards for the data acquisition.

Recently, digital pulse processing has made it possible to replace the afore detailed philosophy implemented using discrete analog electronics, with an equivalent and efficient processing in the digital domain. This is referred to as Digital Pulse Processing (DPP), which is a signal processing technique wherein the preamplifier pulse (output)

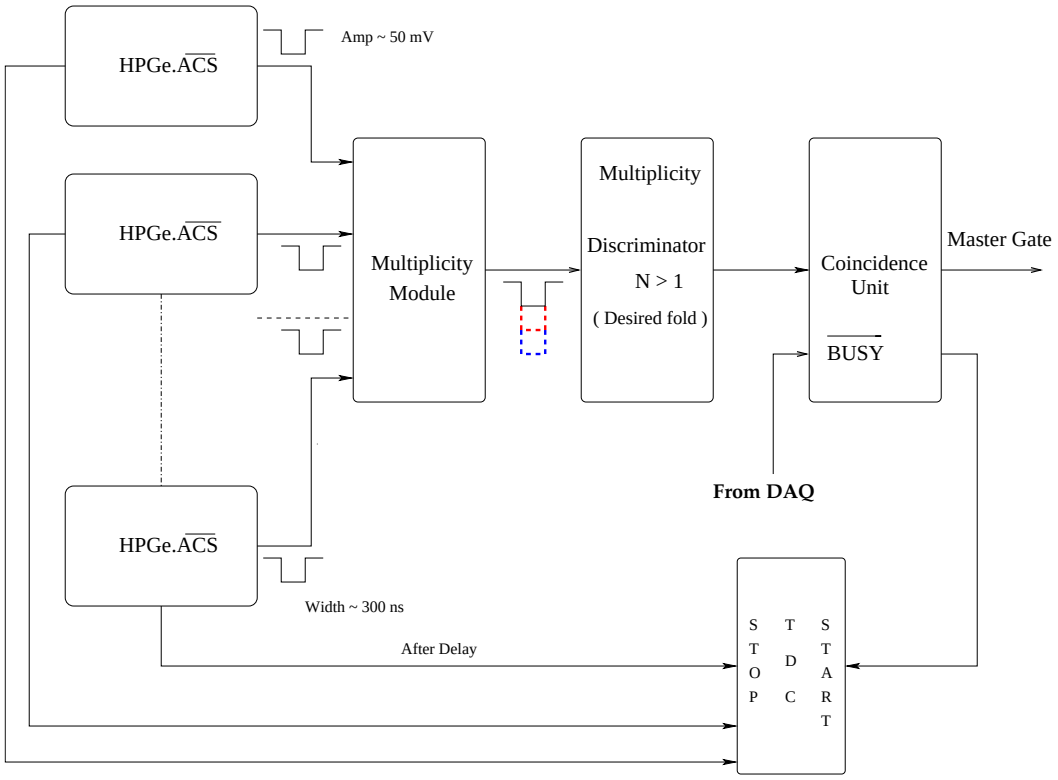

FIG. 17: Block diagram for Compton suppressed Clover Clover coincidence circuit.

from the detector is directly digitized using fast ADC, which are economically available. This digitized signal, is then subjected to digital filters to achieve all fast (timing) and slow (energy) channel operations, using either algorithms implemented within the programmable hardware, or later using offline processing software. Besides making the system highly compact the DPP has several advantages such as a faster system response time, *ie* a significant lower dead-time, which increases the throughput, the ability to upgrade the system software to handle pulses from various detectors, thereby achieving an almost detector independent hardware.

Recently, for the INGA campaign at TIFR, Mumbai, a DSP based pulse processing and DAQ, from M/s XIA, referred to as PIXE-16 was used [38]. One single Pixie - 16 card (which is housed in a VXI crate) has a provision to accept 16 preamplifier pulses and hence could handle 4 Clovers within the same card. Since the energy and timing information is derived from the same signal, we do not require two pre-amplifier output signals from each clover. The preamplifier signal is digitized with a 12 bit 100 MHz

Flash Analog to Digital Converter (FADC). When the digitized data stream enters the signal processing unit where it is shaped accordingly, to obtain the energy and timing information. The signal from the Anti-Compton Shield was input as a veto after a preliminary processing it through conventional NIM electronics. This signal is then converted using a LVDS converter. Time stamped data which satisfied the given user defined criteria was then stored for subsequent analysis. Since the number of Clovers used in the experiment was around 20, the data was acquired using 5 PIXE-16 cards, and hence the event was constructed using the data from the various cards, which was time merged, and then subjected to the conventional analysis using the MARCOS [39] programe.

The online data which is archived for analysis typically has the following format

1. File Header
2. **Event ID**, Parameter-Id, Energy, Time; Parameter-Id, Energy, Time;...
3. **Event ID**, Parameter-Id, Energy, Time; Parameter-Id, Energy, Time;...
4. ...
5. EOF

where the Parameter-Id encodes the detector identity, followed by the corresponding energy and time information. It is assumed that the data from these detectors satisfy the experimental pre-requisite such as the desired detector multiplicity. If an excited nucleus, which is populated in a typical heavy-ion fusion experiment, were to decay to it's ground state, by following the sequence, presented in Fig. 18, then, it would emit the following sequence of γ-rays :

1. γ_8, γ_6, γ_5, γ_2
2. γ_8, γ_6, γ_7

Hence γ_7 and γ_5 or γ_2 would never be in coincidence. The aim of any in-beam gamma-ray spectroscopic investigation is to develop this level scheme, from the observed coincidence relation between the de-exciting γ-rays. Due to the limitation on the number

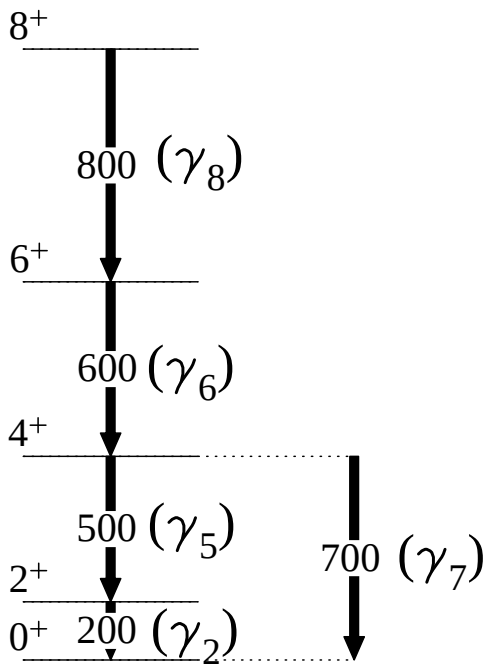

FIG. 18: A hypothetical decay scheme of a nucleus.

of detectors that can be physically housed in the array, which in turn constrains the solid angle covered by the detectors, it is not possible to detect all these emitted coincidence γ-rays. If we have about 20 detectors in the array, at a distance of about 25 cm from the target, which approximately corresponds to about a $4-5\%$ coverage of the total solid angle, we typically would detect atleast two of the coincidence partners. Accordingly, our Master Gate (valid event) is configured to accept atleast two detectors which are in prompt coincidence (typically within 100 - 200 ns). We then would have a data set which generally corresponds to the following events,

1. $Event-1$, γ_8, γ_6
2. $Event-2$, γ_8, γ_7
3. $Event-3$, γ_8, γ_5, γ_6
4. $Event-4$, γ_8, γ_2
5. $Event-5$, γ_6, γ_7
6. $Event-6$, γ_6, γ_5

7. $Event - 7$, γ_6, γ_2

8. $Event - 8$, γ_5, γ_2

9. ...

It is to be noted that the above does not represent the exact structure of the recorded event by event coincidence data (and is a purely generic representation of the recorded info), which is eventually sorted (stored) into a E_γ^N histogram as detailed in the subsequent section. A detailed analysis of this data set, is aimed to extract the observed genetic (sequential) relationships between the de-exciting γ-transitions and this information is then amalgamated with the intensity arguments. The level scheme, is thus developed following a rigorous and meticulous analysis of the recorded $\gamma - \gamma$ coincidence information.

3.2 Analysis of Gamma Gamma Coincidence Data set

The signal from the detector, following the detailed pulse processing, is used as the input to the ADC (Analog to Digital Converter), which digitizes the information for subsequent storage. The information from the ADC is purely in terms of a channel number, which is related to the energy of the observed γ-ray. The process of energy calibration establishes this relationship between the recorded ADC channel and the corresponding E_γ, using radio-active sources (^{152}Eu, ^{133}Ba). However, these sources span an energy range from $\sim$ 80 keV to $\sim$ 1408 keV only. If one were to observe high energy γ-rays, then we have have to incorporate the beam-off radioactivity data which usually contains a few higher energy ($E_\gamma \geq 2$ MeV at $A \sim 30$ region) transitions as calibration points. The Energy (E_γ) - Channel (x) relation is usually parametrized as

$$E_\gamma = a_0 + a_1 x + a_2 x^2 + a_3 x^3 + a_4 x^4 + a_5 \sqrt{x}. \tag{25}$$

Where x^3 term is of relevance at high energy ($\geq$ 1.5 MeV) and $\sqrt{x}$ term is crucial at low energies ($\leq$ 200 keV) [40, 41]. Thus using the constants, known as calibration

constants, we have mapped the ADC channel numbers to their corresponding energies. Once the data has been calibrated, the next process known as *gain matching*, which ensures that the data obtained from each detector has a constant energy dispersion, thereby eliminating the detector dependence on the data. The gain matching process can be mathematically represented using the equation

$$x_{gm} = \frac{1}{epc} \times (a_0 + a_1 x + a_2 x^2 + a_3 x^3 + a_4 x^4 + a_5 \sqrt{x}). \tag{26}$$

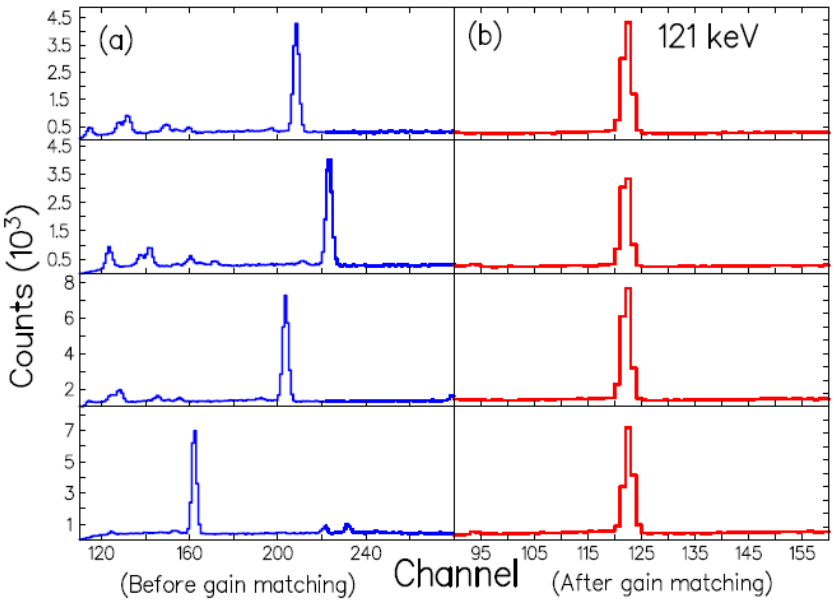

FIG. 19: Corresponds to the spectra (a) before gain matching and (b) after gain matching.

Where E_γ is the energy corresponding to the ADC channel x, "epc" corresponds to the energy per channel and x_{gm} represents the gain matched channel. The results of this procedure, for a 1 keV/channel gain matching (*eg* for E_γ = 121 keV, where the peak centroid would correspond to channel number 121), are presented in Fig. 19. As seen from the figure, following a painstaking, calibration and gain matching, the energies from all detectors are aligned (the recorded energy E_γ in all the detectors are, observed at the same channel number), thereby ensuring that the data is now detector independent.

3.2.A. Development of Level Scheme

The primary requisite to develop the level scheme is to ensure that we detect atleast two γ-rays which are in coincidence (within a time window of 100 - 200 ns), during the de-excitation, of the rapidly rotating nucleus to its ground state, thereby preserving the correlation between them. Such correlations can be conveniently, investigated in detail, if one were to store the coincidence information, say a two parameter coincidence information, in a 2D histogram, which stores the number of events corresponding to a particular combination of the two recorded energy values. Hence, in a $E_\gamma - E_\gamma$ matrix each element $M(i,j)$ contains the number of recorded coincidences between E_{γ_i} and E_{γ_j} Ref.[42]. If the two dimensional array is formed without any pre-condition on the detector (such as angle of the detector) where the axes do not correspond to specific detectors then it is termed as "symmetric matrix". Suppose, the decay sequence is such that we have the following cascade $E_{\gamma_i} \rightarrow E_{\gamma_j}$, results in two coincident γ-rays E_{γ_i} & E_{γ_j} and the detection of this sequence would increment the contents of the location having address (i,j) in the histogram ($M(i,j) = M(i,j)+1$)). However, it is quite possible that the same event is recorded as E_{γ_j} & E_{γ_i}, then this event would increment the contents of the (j,i) cell in the 2D histogram. Thus the contents of the (i,j) and (j,i) cells in the matrix correspond to the same decay sequence (event). Hence, such matrices, need to be symmetrized before analysis, *i.e*, $M(i,j) = M(i,j) + M(j,i)$, thus, in practice we usually store the symmetrized or folded matrices for detailed analysis. The level sequence presented in Fig 18 would result in the 2D histogram shown in the upper panel of Fig 20. As seen from the figure the cells corresponding to the γ-rays which are not in coincidence, do not record any data. This histogram is best viewed or analyzed using 1D spectra, *i.e*, we project this information along one axis say *X-axis*, (shown in the middle panel of Fig 20), which is identical to the *Y-axis*, under the constraints of two limits on the other axis. This exercise, reveals the energy of the gamma-rays which are in coincidence with the gamma-ray specified by the limits. The limits are referred to as "gate", and the spectrum obtained is termed as "gated spectrum" (shown in the bottom panel of Fig 20). This procedure establishes the genetic relationship between the gamma-rays, and helps us in constructing the level sequence. The exact ordering of the γ-rays are based on intensity considerations.

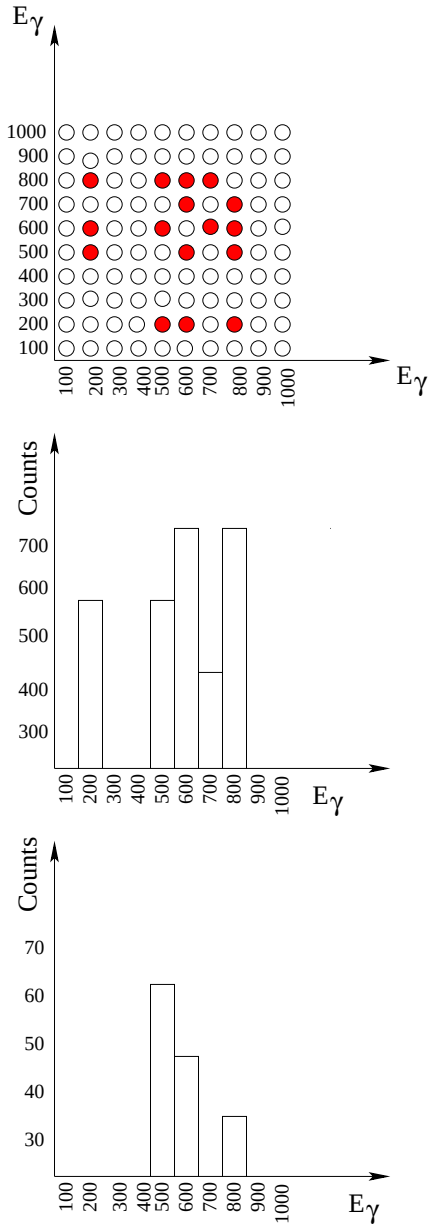

FIG. 20: The upper panel corresponds to the schematic representation of the two dimensional matrix (based on the level scheme shown in Fig 18) and using this matrix we construct the level scheme that we have discussed in the text. The middle panel corresponds to the x projection spectra of the above matrix. The lower panel corresponds to the 200 keV gated spectrum.

When gated on a particular transition all transitions above it, have their intensities in decreasing order, whereas the transitions below it have nearly the same intensity. However, the intensities are calculated after incorporating the efficiency corrections as described in details by R. Chakrabarti *et. al* [43].

It is often required, to analyze the coincidence information, between a certain set of detectors, for example we may require to look at the coincidences between detectors at 90^0 and 132^0 (where the angles are defined with respect to the beam-direction). These matrices which correspond to non-identical detectors along the individual axes are known as "asymmetric matrices" and are primarily of relevance in establishing the spin-parity and the level lifetime of the level.

The dimension (channels) of the 2D histogram is typically 4096×4096. If the matrix memory allocation is either 2 or 4 bytes per channel then the memory requirement is $4096 \times 4096 \times 2$ $(or 4) = 32$ MBytes or 64 MBytes ([44, 45]). Usually the software gain matching is typically 0.5 keV/channel then using 4096 channels, we shall observe gamma-rays with $E_\gamma \leq 2$ MeV. If we expect to observe, high energy gamma-rays (routinely observed in the light mass nuclei) we have to use an energy dispersion of 1.0 keV/channel so as to cover an energy range upto 4 MeV.

Thus the 2D histograms both symmetric and angle dependent provide an efficient way to represent the coincidence correlations among the recorded quantities, which in-turn help us develop the level schemes.

Each event we record could originate from either a photo-peak interaction (P_i), or background (B_i). Therefore, when we record a coincidence between two events, we have a combination of $(P_i, B_i) \otimes (P_j, B_j)$, thus the 2D histogram would contain events such as (P_i, P_j), (P_i, B_j), (B_i, P_j), (B_i, B_j), of which only the (P_i, P_j) events are of our interest as they correspond to full-energy coincidences [40, 41].

Several techniques [40, 41] have been devised to estimate the (P_i, B_j), (B_i, P_j), (B_i, B_j), events which contribute to the observed background in the 2D histograms. These background subtraction procedures when applied to the raw $E_\gamma - E_\gamma$ matrix, results in the preservation of mostly the photo-peak photo-peak information. Such a background subtracted data set is then used for the subsequent analysis (shown in Fig. 21) which is free from spurious / contaminant peaks. As seen from the Fig. 21 in the background unsubtracted gated spectrum we find peaks originating from

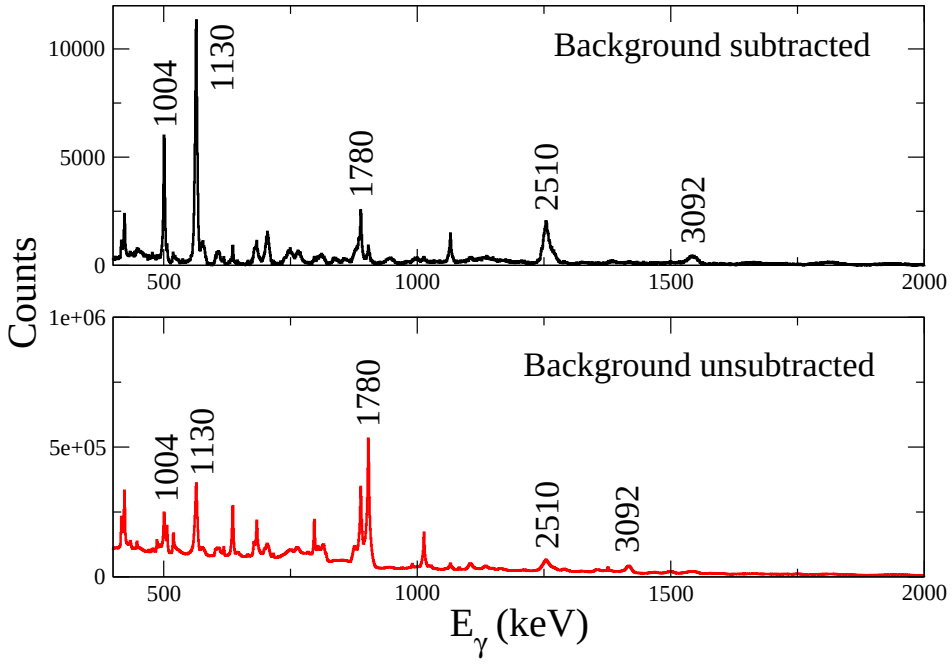

FIG. 21: The background subtracted gated spectrum (1809 keV ($2^+ \rightarrow 0^+$) transition of ^{26}Mg nucleus) is shown in the above panel and background unsubtracted gated spectrum is shown in the lower panel.

contaminants, whereas in the background subtracted gated spectrum we essentially find peaks pertaining to the nucleus of our interest.

3.2.B. Multipolarity Determination

The mere placement of the transitions in the level sequence does not give us the complete information on the level sequence. The spin parity assignments of the levels are essential to have a comprehensive understanding of the level structure. The state with angular momentum and parity (J_i and π_i) decays to a final state characterized by (J_f and π_f). The angular momentum and parity selection rules for the l th order

multipole have to be followed for the $J_i \rightarrow J_f$ transition, *viz.*

$$|J_f - J_i| \leq l \leq (J_f + J_i) \; and \tag{27}$$

$$\begin{aligned} \Delta\pi = \; no: \; even \; electric, \; odd \; magnetic \\ \Delta\pi = \; yes: \; odd \; electric, \; even \; magnetic. \end{aligned} \tag{28}$$

For $J_i = J_f = 0$, the selection rule demands a $l = 0$ transition, hence such a radiative transition will be forbidden as the photon cannot be emitted with zero angular momentum [46]. The states will decay via emission of orbital electron and it is accompanied with the emission of X-rays. A stretched transition is one in which photon carries the algebraic difference between the angular momentum of the initial and final state. The lowest permitted multipoles are usually the most preferred modes of emission. Hence, if we can determine the change in angular momentum Δl associated with a particular transition, then from the knowledge of J_i, the J_f can be assigned (or vice-versa). The γ-ray emitted during the $J_i \rightarrow J_f$ de-excitation, would have would have an angular dependence, which is governed by the associated change in angular momentum, Δl. Hence, the transition would have an angle dependent intensity distribution. This information is used to arrive at the multipolarity assignment for the given transition.

Now let us consider the $1^+ \rightarrow 0^+$ transition. The initial angular momentum state $J_i = 1^+$ has three m sub-states ($m_i = +1, \; 0, \; -1$) and the final state has only one such sub-state ($m_f = 0$). The selection rules allow for transitions connecting all the initial m sub-states $m_i = +1, \; 0, \; -1$, to the final $m_f = 0$ state. As all the m sub states are degenerate (under the present circumstances), thus the resulting γ transition would have an identical energy. Although the transitions have same energy but they possess different characteristics distribution ($F_J^m(\theta)$) whose value depends on the angle (θ) between the emitted γ-ray and the Z-axis (whose choice is arbitrary). This distribution function is essentially obtained by calculating the Poynting vector (energy flow) as a function of θ, such that

$$F_J^m(\theta) = F_J^{-m}(\theta) \tag{29}$$

$$\int F_J^m(\theta) = 8\pi \tag{30}$$

In case of dipole transition [47] we have:

$$F_1^0(\theta) = 3sin^2\theta \tag{31}$$

$$F_1^{\pm 1}(\theta) = 3/2(1 + cos^2\theta) \tag{32}$$

Since all the above three components are equally probable, hence the resultant angular distribution is given by the equation,

$$W(\theta) = 1/3(F_1^1(\theta)) + 1/3(F_1^0(\theta)) + 1/3(F_1^{-1}(\theta)) \tag{33}$$

$$W(\theta) = 1/3 \times 3/2(1 + cos^2\theta) + 1/3 \times 3sin^2\theta + 1/3 \times 3/2(1 + cos^2\theta) \Longrightarrow W(\theta) = 2 \tag{34}$$

From the above calculations we find that $W(\theta)$ is constant, and hence the intensity would be isotropic. Similarly for quadrupole transition we have,

$$F_2^0(\theta) = 5/2(6cos^2\theta - 6cos^4\theta) \tag{35}$$

$$F_2^{\pm 1}(\theta) = 5/2(1 - 3cos^2\theta + 4cos^4\theta) \tag{36}$$

$$F_2^{\pm 2}(\theta) = 5/2(1 - cos^4\theta) \tag{37}$$

$$W(\theta) = 1/5(F_2^0(\theta)) + 1/5(F_2^{+1}(\theta)) + 1/5(F_2^{-1}(\theta)) + 1/5(F_2^{+2}(\theta)) + 1/5(F_2^{-2}(\theta)) \tag{38}$$

We find that, as in the case of a dipole transition, $W(\theta)$ is also constant for quadrupole transition hence the intensity has no angle dependence. However, if we were to preferentially populate one of the the m_i sub-states, say for example the $m_i = 0$ state, for the $J_i = 1^+ \rightarrow J_f = 0^+$ transition, [47] then

$$W(\theta) = 0 \times (F_1^1(\theta)) + 1 \times (F_1^0(\theta)) + 0 \times (F_1^{-1}(\theta)) \tag{39}$$

$$W(\theta) = 1 \times (F_1^0(\theta)) \Longrightarrow W(\theta) \propto sin^2\theta \tag{40}$$

Thus, the resultant intensity depends on the value of $sin^2\theta$, it implies that the intensity has an angular dependence. Similarly, for quadrupole transition if we were preferentially populate the $m_i = 0$ state, then

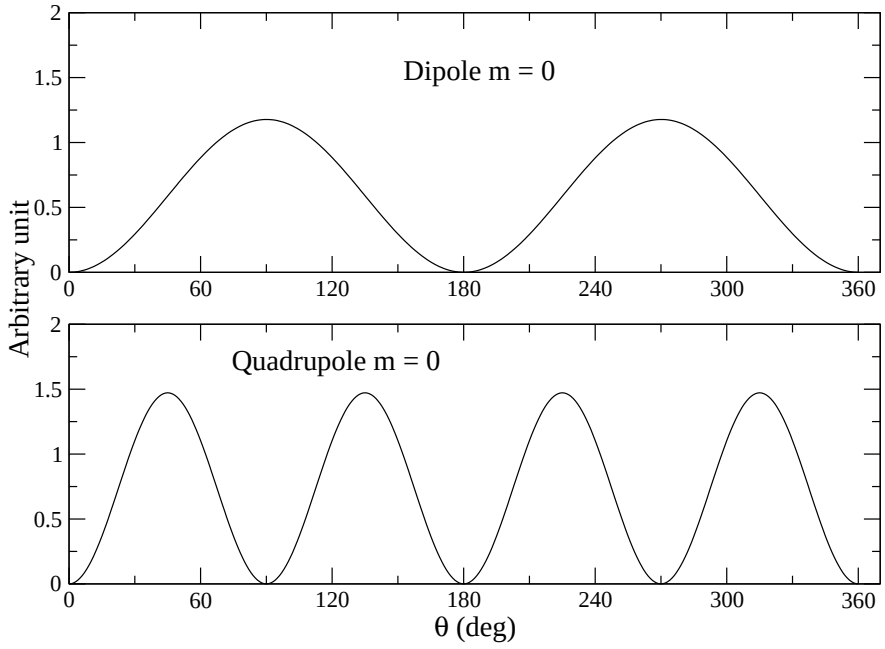

FIG. 22: The intensity distribution for dipole and quadrupole transitions.

$$W(\theta) = 1 \times (F_2^0(\theta)) + 0 \times (F_2^{+1}(\theta)) + 0 \times (F_2^{-1}(\theta)) + 0 \times (F_2^{+2}(\theta)) + 0 \times (F_2^{-2}(\theta))$$
$$W(\theta) = 5/2 \times (6cos^2\theta - 6cos^4\theta) = 5/2 \times 6cos^2\theta(1 - cos^2\theta) \Longrightarrow W(\theta) \propto cos^2\theta sin^2\theta \tag{41}$$

Thus, the resultant intensity of a quadrupole transition depends on the value of $cos^2\theta sin^2\theta$. In the above calculations, we have ignored the normalization constant $1/8\pi$. Such states, wherein we have a preferential population of m sub-states, are referred to as *oriented states*. The gamma-ray emission from such states, would have an angular anisotropy for the observed intensity, which is dependent on the multipolarity (l) of the gamma-ray. Hence, dipole and quadrupole transitions originating from oriented sources, are expected to have a distinct angular anisotropy for the intensity, *ie.* $I_\gamma(\theta)$. The angular distribution for a dipole radiation ($m = 0$) is illustrated in the upper panel of Fig 22, where as, a quadrupole radiation for ($m = 0$), is shown in the bottom panel of Fig 22. As seen from the figures, the intensity of the two radiation quanta have a distinct angular dependence. Such measurements in turn, help

us identify the multipolarity of the radiation.

One of the technique to produce such oriented states, is to use heavy-ion induced fusion evaporation reactions. These reactions preferentially populate $m_i = 0$ states, since the angular momentum is constrained within a plane perpendicular to the reaction plane.

The angular distribution (variation of intensity as a function of the angle) [47] for the $\gamma - \gamma$ cascade for $J_i \rightarrow J \rightarrow J_f$, in which both the γ-rays are of multipole order L_1 and L_2 respectively and are pure, is conventionally represented by the following equation,

$$W(\theta) = 1 + A_{22}P_2(cos\theta) + A_{44}P_4(cos\theta) \tag{42}$$

Where $W(\theta)$ is the γ-ray intensity is measured at angle θ to the beam direction, A_{22} and A_{44} are the angular distribution coefficients and $P_2(cos\theta)$ and $P_4(cos\theta)$ are the Legendre polynomials. The values of the angular distribution co-efficients, for pure multipoles can be written as

$$A_{22} = (F_2(L_1L_1J_iJ) * F_2(L_2L_2J_fJ)), A_{44} = (F_4(L_1L_1J_iJ) * F_4(L_2L_2J_fJ)) \tag{43}$$

Now, if the transitions are mixed *ie.*, two multipole components l and $(l+1)$ contribute to each of the γ-transitions, then the contribution of dominant individual component is quantified by the mixing ratio δ,

$$\begin{aligned} \delta^2(M(l+1)/E(l)) &= \frac{W(M(l+1))}{W(E(l))} \\ \delta^2(E(l+1)/M(l)) &= \frac{W(E(l+1))}{M(E(l))} \end{aligned} \tag{44}$$

Where δ, $W(\lambda l)$ are the mixing ratio and the transition probability respectively and F co-efficients ($F_{2,4}(L_iL_jJ_iJ_f)$) depend on the angular momenta involved in the transition and have been tabulated in Refs.[48]. The co-efficients for mixed transitions are expressed as

$$\begin{aligned} A_{22} &= \frac{1}{1+\delta^2}(F_2(L_1L_1J_iJ) + 2\delta F_2(L_1L_1'J_iJ) + \delta^2 F_2(L_1'L_1'J_iJ)) \\ A_{44} &= \frac{1}{1+\delta^2}(F_4(L_1L_1J_iJ) + 2\delta F_4(L_1L_1'J_iJ) + \delta^2 F_4(L_1'L_1'J_iJ)) \end{aligned} \tag{45}$$

Since the nuclei are partially aligned after their formation, to include this effect, we use

a multiplicative factor α_j, known as the "attenuation co-efficients", where

$$\begin{aligned} A_{22}(cal) &= A_{22}\alpha_2 \\ A_{44}(cal) &= A_{44}\alpha_4 \end{aligned} \tag{46}$$

The values of $\alpha_{2,4}$ coefficients are listed in the Ref.[49]. Efficiency corrected angle dependent intensities are used to obtain angular distribution coefficient. The experimental mixing ratio can be obtained from the χ^2 minimization procedure [50], where the value of χ^2 is defined by the equation,

$$\chi^2 = \frac{[A_{22}(expt) - A_{22}(cal)]^2}{3[\Delta A_{22}(expt)]^2} + \frac{[A_{44}(expt) - A_{44}(cal)]^2}{3[\Delta A_{44}(expt)]^2} \tag{47}$$

Where $\Delta A_{22,44}(expt)$ are the uncertainties in the experimentally observed angular distribution coefficients and $A_{22,44}(expt)$ are defined as

$$\begin{aligned} A_{22}(expt) &= \frac{A_{22}}{A_{00}} \\ A_{44}(expt) &= \frac{A_{44}}{A_{00}} \end{aligned} \tag{48}$$

Angular distribution measurements have been used in the present thesis to deduce the information on the multipolarity (and the mixing ratio) of the γ-ray, and are presented in the subsequent chapters. However, the angular distribution measurement, is a *singles measurement*, [1] and therefore, such measurement has its inherent limitation. In a heavy-ion induced fusion evaporation reaction a large number of nuclei are populated, in addition to a reaction specific characteristic continuum background, making it difficult to identify the weak transitions of interest in the singles spectrum. As a consequence, it is very difficult to perform the angular distribution measurement for these transitions.

Since, the fusion reaction preferentially populates $m = 0$ sub-states, we would observe an anisotropy in the angle dependent intensity. Hence, if we were to sort the data observed at two angles, then all transitions which have the same multipolarity would have a similar angular dependence of their respective intensities.

For example, if we set a gate on a quadrupole ($\Delta J = 2$) transition, say $E_\gamma = 2167$ keV ($2^+ \rightarrow 0^+$) [23] transition in ^{38}Ar, and we observe that, the intensity of $E_\gamma = 777$

[1] A singles measurement corresponds, to recording the data in all the N number of detectors, when anyone of the detectors has a non-zero data, hence this data set corresponds to an uncorrelated set of events.

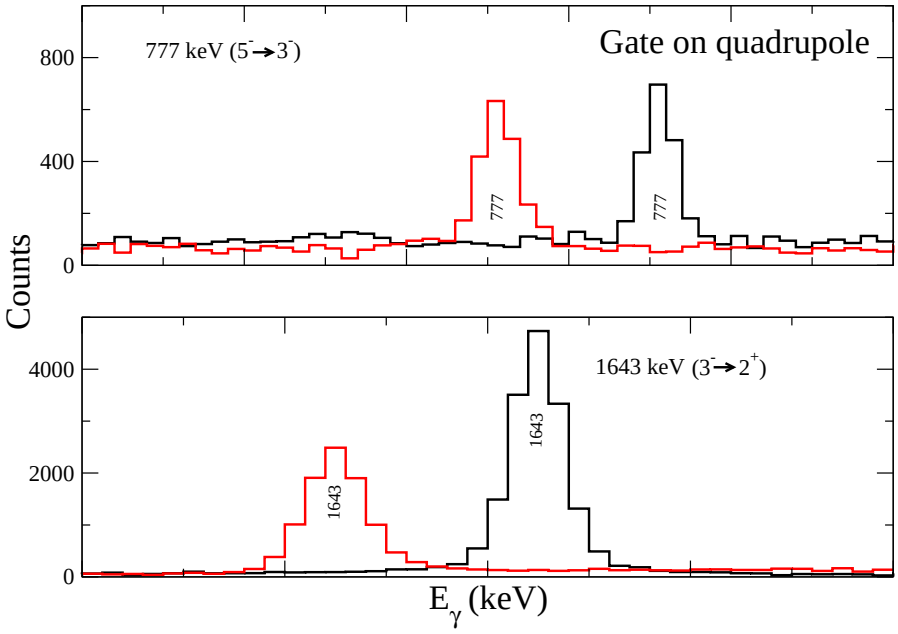

FIG. 23: Quadrupole gated spectrum black spectra corresponds to the 90° and red one corresponds to the spectrum at forward angle (here 32°). The spectra are displaced with respect to each other for clarity.

keV is nearly identical at both 90^o and 32^o (shown in Fig 23), which indicates that this transition also involves a $\Delta J = 2$, change in angular momentum. Indeed, this transition is a quadrupole transition, $(5^- \rightarrow 3^-)$. However, the intensity of $E_\gamma = 1643$ keV transition, differs by almost a factor of two (from Fig 23), at the two angles. This implies that this transition is a dipole in nature, and indeed it is so $((3^- \rightarrow 2^+))$. Thus this procedure merely identifies the change in angular momentum, ΔJ and is not sensitive to the electromagnetic nature of the transition. Thus $M1$ and $E1$ would exhibit to a similar angular intensity pattern.

This angular intensity anisotropy which is referred to as R_{DCO} (directional correlation from oriented nuclei) is extracted from the angle dependent $\gamma - \gamma$ matrices, where one axis contains the energy recorded in detectors placed at an angle θ_1 (with respect to beam axis) and the other axis corresponds to the coincident energy recorded in the

detectors placed at an angle (θ_2). Then the R_{DCO} is defined as :

$$R_{DCO} = \frac{I^{\gamma 2}_{\theta_1}[Gate^{\gamma 1}_{\theta_2}]}{I^{\gamma 2}_{\theta_2}[Gate^{\gamma 1}_{\theta_1}]}. \tag{49}$$

Where, for example, $I^{\gamma 2}_{\theta_2}[Gate^{\gamma 1}_{\theta_1}]$ represents the intensity of transition $\gamma 2$ as recorded in detectors at the angle θ_2, when energy gate is set on $\gamma 1$ in detectors at θ_1, and vice-versa for $I^{\gamma 2}_{\theta_1}[Gate^{\gamma 1}_{\theta_2}]$. Assuming, the commonly encountered stretched transitions [2], and if we know the multipolarity of the gated transition then :

1. If the value of $R_{DCO} \sim 1$ then the observed transition has a similar multipolarity as the gated transition.

2. If the value of R_{DCO} is $\sim$ 0.5 or $\sim$ 2 then observed and gating transition have opposite multipolarity .

The above described technique, demands that the gate to be set on a detector at an angle (forward or backward $w.r.t$ the beam direction). This technique has one limitation, if the observed transition exhibits a Doppler shape (which originates when the stopping time of the recoils is $\sim$ or greater than the level lifetime, due to which the emission occurs in flight). It is not possible to properly set gate on γ-rays with shapes at forward and or backward angle, since the gates would then be quite wide, which in turn would introduce considerable contaminants in the gated spectrum. Besides, it is not easy to precisely determine the gating limits for such transitions. In view of these difficulties, it is not possible to set gates on the transitions at angles other than 90°, to extract the R_{DCO} value. To circumvent this problem we define a parameter known as Anisotropy Ratio [9],

$$R_{anisotropy} = \frac{I_{\gamma 1}\ (at\ \theta_1\ gated\ by\ \gamma 2\ at\ 90^\circ)}{I_{\gamma 1}\ (at\ \theta_2\ gated\ by\ \gamma 2\ at\ 90^\circ)}. \tag{50}$$

The advantage of this procedure is that the gates are always set on transitions at detectors placed at 90^o, thus avoiding the Doppler shapes. The intensity of the coincident γ-rays are noted at two different angles other than 90^o. This prescription was followed to obtain the information on the dominant multipolarity of the de-exciting transition and is detailed in the subsequent chapters.

[2] stretched transitions involve the algebraic difference of the initial and final spins

Thus the coincidence angular anisotropy helps us deduce information on the multipolarity of the de-exciting transition.

3.2.C. Linear Polarization Measurements

The use of Clover detectors uniquely facilitates the measurement of linear polarization of the observed γ-ray transitions which helps in determining the electro-magnetic nature of the transition. Each crystal of the Clover detector acts as a scatterer and the adjacent two crystals are the absorbers, along the perpendicular and parallel direction, with respect to the reaction plane. The distinction between the electric and magnetic transition can be obtained from the observed asymmetry between the number of perpendicular and parallel Compton scattered events for a given γ transition. For example, the 1596 keV ($7/2^- \rightarrow 5/2^+$), transition in ^{29}Si, is predominantly an electric transition with $\delta = 0.14 \pm 0.04$ [28]. Hence, it should have a preferential scattering along the perpendicular direction (with respect to the reaction plane), which indeed is observed by us as presented in the Fig 24. Similarly, an magnetic transition is expected to have a preferential scattering along the parallel direction, which is observed (in the lower panel in Fig 24) for the 670 keV ($4^- \rightarrow 3^-$) transition in ^{38}Ar nucleus.

The asymmetry between the perpendicular and the parallel scattering is quantified as,

$$\Delta_{Pol} = \frac{aN_{\perp} - N_{\parallel}}{aN_{\perp} + N_{\parallel}}, \tag{51}$$

where $N_{\perp}$ and $N_{\parallel}$ are the number of photons scattered in the perpendicular and the parallel direction respectively. The parameter *"a"* denotes a correction factor due to the asymmetry in the geometrical response of the Clover segments in the array. It is measured by using unpolarized γ-ray emission, and the following equation as detailed in Ref.[51].

$$a = \frac{N_{\parallel}}{N_{\perp}}. \tag{52}$$

The value of the asymmetry factor is energy dependent ($a(E_\gamma) = a_0 + a_1 E_\gamma$) and the parameters a_0 and a_1 are determined using radioactive sources and beam-off radioactivity under identical experimental conditions (source position etc.) as the in-beam

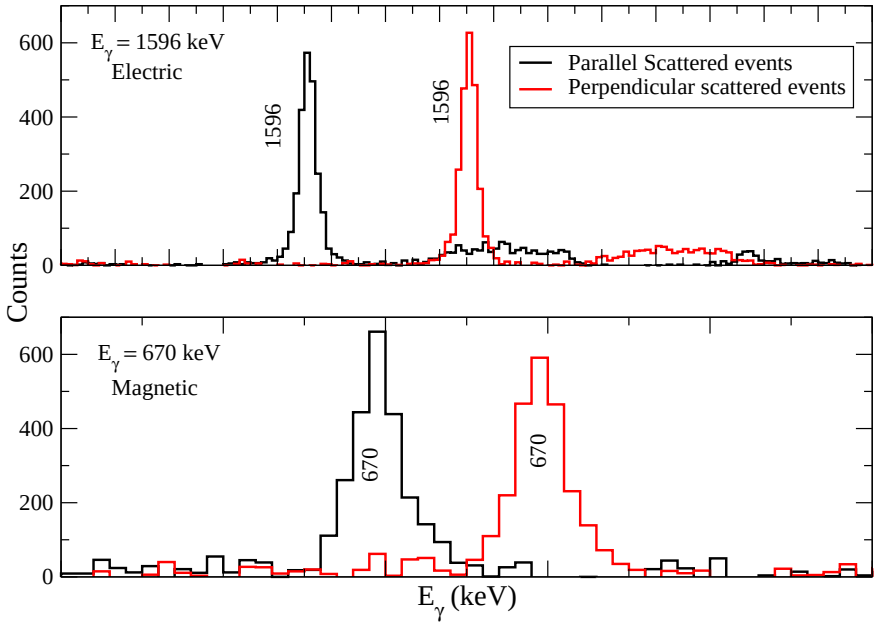

FIG. 24: The intensity variation for electric and magnetic transitions, in the perpendicular and parallel scattered events. The spectra are displaced with respect to each other for clarity.

measurements. This asymmetry is anticipated to be nearly independent of the γ-ray energy and hence the expected values of the constant are $a_0 \sim 1$ and $a_1 \sim 1{\times}10^{-6}$. For the present experiment, the typical value of the fitting parameters are, $a_0 = 1.003 \pm 0.002$ and $a_1 = 1.0 \pm 4.0 \times 10^{-6}$ $(keV)^{-1}$. Owing to the very small value of the a_1 coefficient ($\sim 10^{-6}$) it was not considered in the present work. The value of the Δ_{Pol} is extracted from the two asymmetric γ - γ matrices where the Y-axis contains the parallel (perpendicular) scattered events in detectors at 90° and X-axis contains the coincident events in all other detectors. Gates are applied on X-axis and counts corresponds to the parallel ($N_{\parallel}$) and the perpendicular ($N_{\perp}$) scattering are obtained from the resulting spectra. The value of Δ_{Pol} is indicative of the electro-magnetic nature of the γ-transition. For a pure electric transition Δ_{Pol} is positive while a negative value of Δ_{Pol} implies a magnetic transition. A near zero value of Δ_{Pol} is suggestive of the mixed nature for the transition. The polarization asymmetry is related to the degree of

linear polarization (P) as

$$P = \frac{\Delta_{Pol}}{Q(E_\gamma)}, \tag{53}$$

where $Q(E_\gamma)$ [51] is the energy dependent polarization sensitivity,

$$Q(E_\gamma) = (CE_\gamma + D)Q_0(E_\gamma) \tag{54}$$

where,

$$Q_0(E_\gamma) = \frac{(\alpha+1)}{(\alpha^2+\alpha+1)}, \tag{55}$$

with,

$$\alpha = \frac{E_\gamma(MeV)}{0.511}, \tag{56}$$

The theoretical value of polarization ($P(\theta = 90^o)$) [52] can be expressed as

$$P(\theta = 90^o) = \pm\frac{3A_{22}(cal)H_2 - 7.5A_{44}(cal)H_4}{2 - A_{22}(cal) + 0.75A_{44}(cal)} \tag{57}$$

Where θ is the angle of emission of the γ-rays from an oriented source with respect to the orientation axis, and $H_{2,4}$ are functions that depend on the initial and final spins and the mixing ratio. The $A_{22,44}(cal)$ are the angular distribution coefficients. The + (-) sign applies for a transition without (with) change in the parity. The value of polarization attains a maximum value at $\theta = 90^o$. The value of $P = \pm 1$ for completely polarized γ-rays and is 0 for unpolarized γ-rays. For pure transition (M1 or E1) the value of $H_{2,4}$ are 1, -1/6 respectively. For a mixed dipole and quadrupole transition the values of $H_{2,4}$ are given by

$$H_2(1,2) = \frac{F_2(1,1) - (2/3)\delta F_2(1,2) + \delta^2 F_2(2,2)}{F_2(1,1) + 2\delta F_2(1,2) + \delta^2 F_2(2,2)} \tag{58}$$

and

$$H_4(1,2) = -1/6. \tag{59}$$

Similarly for an admixture of $\Delta J = 2$ & 3 the values are

$$H_2(2,3) = \frac{-F_2(2,2) - \delta F_2(2,3) + (2/3)\delta^2 F_2(3,3)}{F_2(2,2) + 2\delta F_2(2,3) + \delta^2 F_2(3,3)} \tag{60}$$

and

$$H_4(2,3) = \frac{5F_4(2,2) - 2\delta F_4(2,3) + 20\delta F_4(3,3)}{30(F_4(2,2) + 2\delta F_4(2,3) + \delta^2 F_4(3,3))}. \tag{61}$$

As a part of the present thesis, the linear polarization measurements were performed for several transitions in ^{26}Mg and ^{29}Si to uniquely assign their electro-magnetic nature. The polarization asymmetry Δ_{pol}, were experimentally obtained, and this allowed us to determine the experimental polarization, which was successfully compared with the predicted theoretical polarization values, and a reasonable agreement was noted.

Hence, the angular intensity anisotropy and the asymmetry between the parallel and perpendicular scattering (with respect to the reaction plane) helped us assign unambiguously the spin and parity of the levels de-exciting with the corresponding γ transition. Thus we were able to obtain a detailed information of the level scheme of the nucleus under study. However, a more complete and unique information on the underlying configuration of the observed levels is obtained from the measurement of the level lifetimes. The measurement techniques are dependent on range of the expected time scale for the level lifetimes.

3.2.D. Lifetime Measurements

The fast moving excited residual nuclei are slowed down and eventually stopped in the backing medium, and the stopping process typically requires about few tens of fs to few ps. If the residual nucleus emits a γ-ray while in motion, which are detected either in the forward or backward direction (with respect to the beam direction) before it stops, the energy of the detected γ-ray exhibits Doppler effect (shape or shift). The measurement of this Doppler shape or shift coupled with the slowing down history of the recoils, with an appropriate inclusion of the reaction kinematics, can used to extract the lifetime of the level de-excited by the emitted γ-ray transition. This is the principle of the Doppler Shift Attenuation Method (DSAM) for determining the level lifetimes in the range of few tens of fs to few ps. The transition strengths deduced from these measurements, are connected with the initial and final wave-functions of the involved levels, and provide us with a stringent test for the validity of nuclear model, which elucidate the observed level structure.

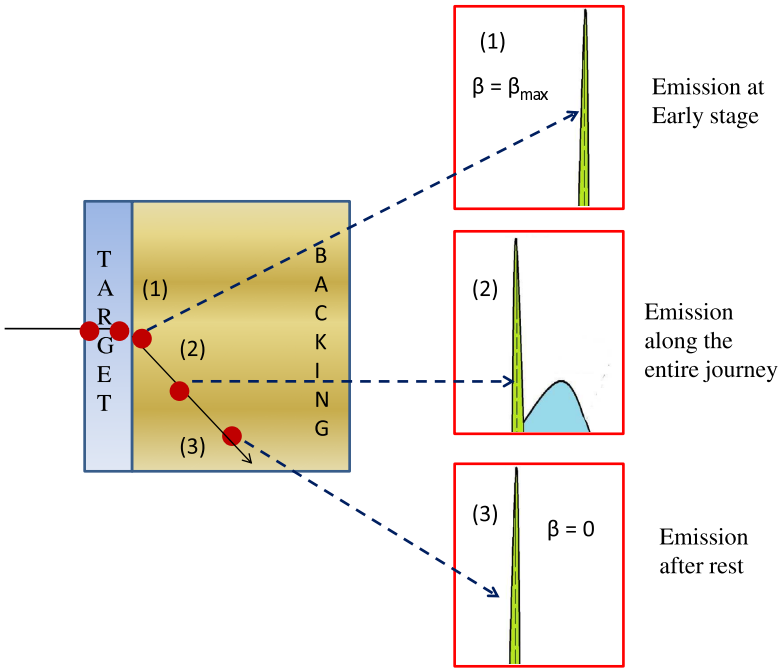

FIG. 25: The schematic diagram for observed energy of γ-ray as viewed by the (forward) detector when the residue emit γ-rays in flight.

DSAM exploits the observed Doppler effects during the slowing down of the recoiling nuclei, in an elemental high-Z backing, while de-exciting with the emission of γ-ray transitions. If the lifetime of the level is less than or comparable with the stopping time then the γ-ray emitted from such an excited nucleus with recoiling velocity $\beta(= v/c)$ will undergo a Doppler effect (non relativistic) given by,

$$E_{obs} = E_0[1 + \beta \cos\theta] \tag{62}$$

where E_{obs}, is the energy of the observed γ-ray, E_0 is the energy of γ-ray emitted by a nucleus decaying at rest, and θ is the angle between the direction of recoil and that of the emitted γ-ray. In case of very short-lived states (lifetime << stopping time) and detector at angles $\neq 90^\circ$, the γ-ray transition peak in the spectrum is shifted, compared to the actual energy, to higher (lower) energies when observed at forward (backward) angles with respect to the direction of the recoiling nuclei. For levels with lifetime $\sim$ stopping time, the peak has a stopped component at the actual energy and an accompanying shape, extending to higher (lower) energies for detectors at forward (backward) angles.

The LINESHAPE [53] code is widely used to extract the level lifetimes form the observed Doppler shapes and shifts using the Doppler Shift Attenuation Method. This method requires a thin target backed with a high Z **elemental backing**. The thin target ensures that the residue do not loose appreciable energy while traversing the target, and the **elemental backing** ensures that the uncertainties in the simulation of the slowing down process is minimized. However, in the present measurements we had a thick molecular Ta_2O_5 target, which in contradistinction to the conventional scenario. Hence, the LINESHAPE code was extensively modified to cater to our specific experimental requirements which are circumstantiated in Ref.[7]. Least squares fitting of the observed shapes to the calculated ones was carried out simultaneously at different angles for determination of the level lifetimes. The parameters for the fitting procedure included the level lifetime, the side-feeding time, the peak height, the contaminant peak(s), and the background parameters etc. The results are elaborated in the subsequent chapters.

Following this conscientious analysis, we develop the level scheme of the residual nucleus of interest, along with details such as the level excitation energy, spin, parity, and the level lifetime. All these then help us to corroborate the model predictions, and or rarefy the same. Thus this exercise of a detailed description of the de-exciting process culminates finally, in undertaking the appropriate model calculations, relevant to the nucleus under investigations.

Chapter - 4

Nuclear Shell Model

The final aim of any investigation in nuclear structure, is an attempt to describe the observed level structure within the purview of a nuclear model. This would require us to solve the Schrödinger Equation (SE) to obtain the wave function of the nuclear system. Mathematically it is next to impossible to analytically solve the SE, for this few body system, wherein the major hurdle stems from (i) the fact that as discussed earlier that the exact nature of the nuclear potential is not well known, (ii) computational limitations. Thus we employ *nuclear models*, which are based on the comparison (similarities) between the nucleus and simpler (analogous) systems which can be adequately modeled mathematically. All nuclear models, must encompass the diverse aspects *viz.*, the microscopic as well as universal aspects, of nuclei. A microscopic model description based on the solid foundations of first principles, ensures a reliability for extrapolation to region currently inaccessible to experimental endeavours. On the other hand the universal description to the nuclear properties provided by the model ensures a kind of simplicity while providing a coherent prediction for properties across the nuclear landscape. The caveat for any nuclear model is that the model proposition limit it's range of applicability. In this chapter we have attempted to summarize the nuclear shell model, one of the most fundamental nuclear model, which has been exhaustively used in the present thesis.

To explain the various properties of the atomic nucleus, the different models are developed. The macroscopic properties such as the Binding energy, shape etc were reasonably explained within the framework of the liquid drop model. On the other hand, the microscopic property of the nucleus such as nuclear spin, parity and magnetic moment etc. can be explained from the nuclear shell model. Like the atomic shell structure the nucleus exhibit a similar kind of shell structures. For a certain number of electrons, the atomic shell exhibits its inert nature (shell closure). A similar kind of nature has been observed in case of atomic nucleus also. It was observed that in case of certain nucleon number when the neutrons or protons = 2, 8, 20, 28, 50, 82, 126 the binding

TABLE II: Classifications of the various nuclear models of contemporary relevance.

Classification	Semiclassical	Quantum Mechanical
Independent Particle Models	Fermi Gas Model	Spherical Shell Model
Collective Models	Liquid Drop Model	Rotational Model Vibrational Model

energy per nucleon had a sharp increase as compared with it's immediate neighbour, indicating enhanced stability for these nuclei. Several additional experimental evidence was found to support the nuclear shell structure and are discussed in the subsequent section.

4.1 Early Nuclear Models

Since, the nucleus is a few body system, which at times manifests itself as a two body system (wherein the nuclear properties are primarily explained through the interactions of a small / few nucleons only), while otherwise it presents itself as a collective ensemble, wherein the observed properties can only be explained if one were to consider the behaviour / contribution from a substantial number of nucleons. Hence, the models are naively classified as Independent Particle Models, where all nucleons are considered to be different, and Collective Models, which assumes all nucleons are similar, and examines the macroscopic properties of the nucleus such as it's size, binding energies etc. Table II summarizes the classification of the prevalent nuclear models, routinely used in nuclear structure investigation.

The earliest nuclear models could be traced to the Liquid Drop and the Fermi Gas Model. The Fermi Gas model is expected to be valid for the nucleus which comprises of interacting fermions, which obey Fermi Dirac Statistics. This model assumes that since neutrons and protons are distinguishable fermions and hence are situated in two separate potential wells, wherein the binding potential is generated by all the nucleons. The nuclear potential can be considered as a rectangular well, since the nucleons inside do not experience net force, whereas the unequal ambiance for the surface nucleons results in them experiencing a net force. All the available energy states are filled by

pairs of nucleons, and the energy of the highest occupied level (state) is referred to as *Fermi Energy* (E_F). This model could predict the average binding energy, which is defined as the energy difference between the top of the well and the Fermi level to be $\sim 7 - 8$ MeV. This model however, could not reproduce the microscopic details such as the spin and parity of the observed levels. This model has proved to be a good starting point for our understanding of this intriguing few body system *viz.* the nucleus.

The Liquid Drop model was one of the earliest nuclear model, which attempts to understand the macroscopic properties of the nucleus, such as the binding energy, nuclear size, to name a few. It is a Semi Empirical model, which did posses predictive powers. This model attempts to understand the nuclear properties, based on an analogy with a drop of liquid.

4.2 Spherical Shell Model

When one investigates the properties of atoms, it is observed that elements with atomic numbers $Z = 2,\ 10,\ 18,\ 36...$ show enhanced stability, *ie* they have unusually high electron ionization energy, they do not react to form molecules, to name a few. The concept of atomic shell helps us understand this observation. Hence, it seemed appropriate to develop an analogous (similar) shell structure (model) for the nucleus, based on the following experimental observations.

1. The nucleus for which neutron or proton numbers or both are magic numbers ($N, Z = 2,\ 8,\ 20,\ 28,\ 50,\ 82,\ 126$), such as ^{4}He, ^{16}O, ^{40}Ca and ^{208}Pb are particularly more stable and have greater binding energy than its immediate neighbours.

2. The high natural abundance of nuclei with neutron or proton number or both equal to the nucleon magic number.

3. Sudden increase of $\bar{B}$ (binding energy per nucleon) as a function of A for nuclei such as ^{4}He, ^{88}Sr, ^{140}Ce and ^{208}Pb.

4. There are large number of stable isotopes or isotones of nuclei having neutron or proton or both equal to the magic number.

5. The nuclei with magic neutron number have low neutron capture cross-section.

6. The nuclei with magic neutron or proton number or both have a higher excitation energy for the first excited state.

These observations hint at the existence of shell structures in the nucleus that forms the basis of the nuclear shell model. Maria Goeppert Mayer developed this model, which explains the existence of structured shells in which nucleons are distributed within the nucleus. For this work, she shared the 1963 Nobel Prize in Physics [4–6]. Goeppert Mayer is only the second woman to receive the Nobel Prize in Physics. According to the shell model, each nucleon in the nucleus experiences a *one-body mean field*, due to the motion of all other nucleons. Each nucleon moves independently and Pauli's exclusion principle, ensures that they do not collide with each other. The shell model classifies the energy levels in terms of quantum numbers $n,\ l,\ j$ following an analogous prescription to atomic physics. For a spherically symmetric potential the wave function for nucleon whose polar co-ordinates are (r, θ, ϕ) has the following analytical form

$$\Psi_{nlm} = R_{nl}(r)Y_l^m(\theta, \phi). \tag{63}$$

Till date the exact nature of the nuclear potential is not well known. We usually model this potential and the choices are

- 3-D spherical harmonic oscillator, which has the familiar form

$$V(r) = -V_0 + (1/2)(m\omega^2 r^2) \tag{64}$$

  Where ω is the harmonic oscillator frequency, m is the mass of the nucleon and V_0 is the depth of the potential well.

- Spherical infinite square well, which is represented by

$$V(r) = \begin{cases} -V_0 & \text{for} \quad +\infty \leq r \leq R \\ +\infty & \text{for} \quad r > R \\ \text{R is the nuclear radius} \end{cases} \tag{65}$$

- Woods Saxon potential, as a function of the distance r from the center of nucleus, is

$$V(r) = -\frac{V_0}{1 + exp(\frac{r-R}{a})} \tag{66}$$

where V_0 (having dimension of energy) represents the potential well depth. The constant nucleon density in the nuclear interior justifies the flat central part for the potential. The potential can be solved numerically, and it tends to zero at distances well beyond the nuclear radius. At the halfway radius R, we have $R = R_0 A^{1/3}$ (A, is the mass number of the nucleus and $R_0 \sim 1.2$ fm). It is customary to have the value of diffuseness a to be $\sim 0.5 - 0.8$ fm.

The Schrödinger equation for the single particle levels is given by.

$$\sum_{i=1}^{A} \Big(-\frac{\hbar^2}{2m}\nabla_i^2 + V(r_i)) \Big)\psi_i = \epsilon_i \psi_i \tag{67}$$

The first term represents the kinetic energy of the individual nucleons and the second term corresponds to the potential energy. The ψ_i corresponds to the single particle wave function and ϵ_i represents to the single particle energy of the i-th particle. After substituting the appropriate choice of potential, for example either the Wood-Saxon, or the harmonic oscillator, in the above Schrödinger equation we obtain the energy eigenvalues,

$$E_N = -V_0 + (N + 3/2)\hbar\omega \tag{68}$$

$$with \begin{cases} N = 2(n-1) + l & \\ \quad n = 1,\ 2,\ 3... & \text{principal quantum number} \\ \quad l = 0,\ 1,\ 2... & \text{orbital angular momentum} \end{cases} \tag{69}$$

The energy eigenvalues are degenerate in magnetic quantum number m. The energy levels are usually bunched together (for a given N) and are referred to as *shells*. Levels corresponding to different N are well separated in energy, and the gap between two major principal quantum numbers is referred to as a *shell gap*. The maximum number of nucleons in each energy level is $2(2l + 1)$, where the factor 2 corresponds to the $+1/2, -1/2$ spin states of the nucleon. For example, the lowest level designated as $1s$, and would correspond to $n,\ l\ = 1,\ 0$ and would have a maximum occupancy of two nucleons, whereas the next level $1p$ ($n,\ l\ = 2,\ 1$) would have a maximum occupancy of

6 nucleons. Thus the number of nucleons in each major shell would then correspond to 2, 8, 20, 40, 70, 112, 168. This exercise resulted in the reproduction of the lowest three magic numbers, but failed in it's representation (interpretation) of the higher magic numbers.

The major difficulty one could envisage while porting the atomic shell concept to nuclear shells, is that nucleus contains particles with spin up and spin down ($m_s = \pm 1/2$) and as a result, the total angular momentum j has the magnitude $j = l + (1/2)$ & $l - (1/2)$. So in a sense, spin, could be either parallel or anti-parallel to the orbital angular momentum. Once, this effect was incorporated into the nuclear potential, a seminal milestone achieved by Mayer *et al* [4–6], all the nuclear magic numbers could be reproduced naturally. Their formalism resulted in the re-distribution (ordering) of the orbitals and the recalculation of the shell closures that now complied with the experimental observations for magic numbers. They introduced the the strong nuclear spin orbit interaction (spin orbit potential is proportional to $\vec{l}.\vec{s}$), in the nuclear potential. Hence the effective potential in which the nucleons move is now given by the equation

$$V_{eff}(r) = V(r) - V_{ls}\frac{\partial V(r)}{\partial r}\vec{l}.\vec{s} \tag{70}$$

Where V_{ls} is the strength of the spin-orbit interaction. The inclusion of the spin-orbit term results in a wider nuclear potential (wider well results in lowering the energy of the states) for nucleons with spin parallel to the orbital angular momentum, and a narrower potential for nucleons with spin opposite to the orbital angular momentum.

The $\vec{l}.\vec{s}$ term causes the degenerate energy levels with same l to split into $j = l \pm 1/2$ levels with degeneracy $(2j + 1)$. Each orbitals contains $(2j + 1)$ number of nucleons. For example, the $2p$ $(l = 1)$ level would now split into $p_{3/2}$, $(l + 1/2)$ and $p_{1/2}$, $(l - 1/2)$ levels, with and the $2p_{3/2}$ orbital contains $(2 \times 3/2 + 1) = 4$ number of nucleons. The total angular momentum of a nucleon is given by

$$\vec{j} = \vec{l} + \vec{s} \tag{71}$$

and hence

$$\vec{l}.\vec{s} = 1/2(j^2 - l^2 - s^2) \tag{72}$$

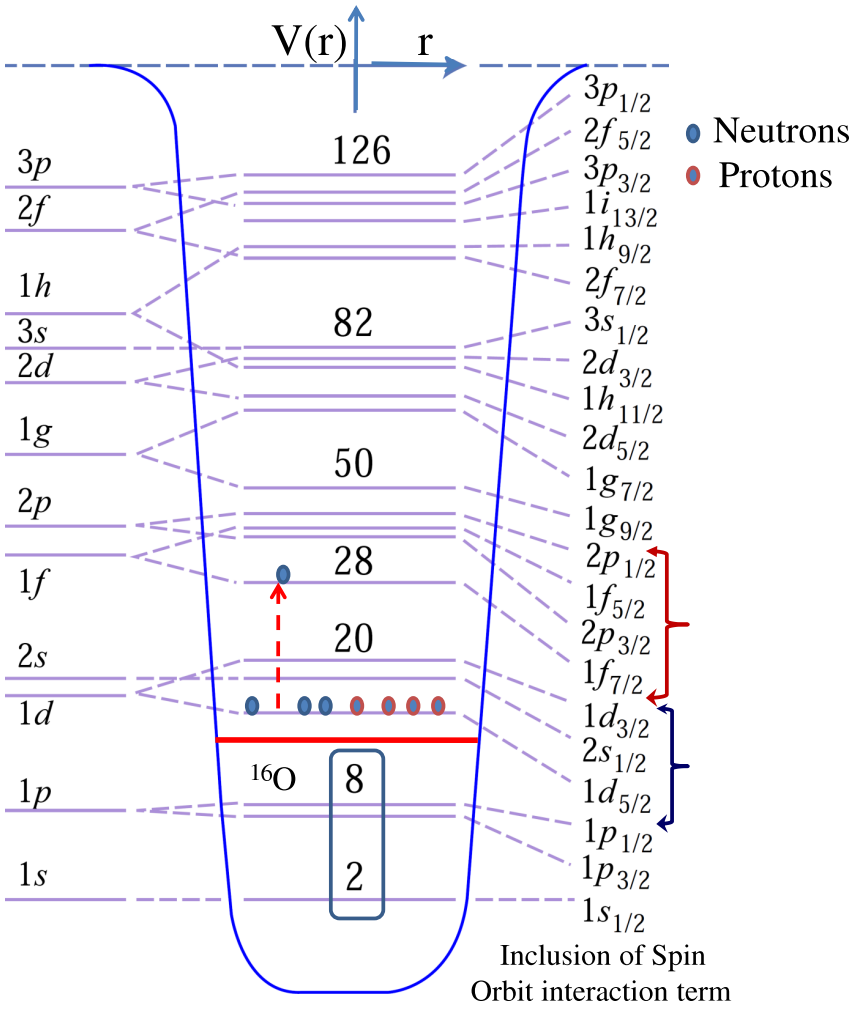

FIG. 26: Energy levels for Nuclear Shell Model. The right hand side of the figure corresponds to energy levels after incorporation of the Spin Orbit interaction term. (Adapted from Meyerhof).

It's average value is given by

$$\left\langle \vec{l}.\vec{s} \right\rangle = 1/2(\left\langle j^2 \right\rangle - \left\langle l^2 \right\rangle - \left\langle s^2 \right\rangle) \tag{73}$$

$$\left\langle \vec{l}.\vec{s} \right\rangle = \frac{l}{2}\hbar^2 \ for \ j = l + 1/2 \tag{74}$$

and

$$\left\langle \vec{l}.\vec{s} \right\rangle = -\frac{(l+1)}{2}\hbar^2 \ for \ j = l - 1/2. \tag{75}$$

The energy difference between these two states is then given by $1/2(2l+1)\hbar^2$.

After incorporation of the spin orbit interaction term the l degeneracy is removed, and the energy levels split into $l \pm (1/2)$ levels as shown in Fig. 26. The large spin-orbit

effect leads to crossing over of energy levels into different shells resulting in a faithful representation of the observed magic numbers at 2, 8, 20, 28, 50, 82, 126, which are in conformity with the experimental observations.

The greatest success of the shell model is it's satisfactory representation of properties of nuclei in and around the magic numbers. The level excitation energies, spin, parity, magnetic and quadrupole moments for the ground state and low-energy excited states are satisfactorily predicted / reproduced by this model.

The shell model reproduces the properties of nuclei in and around the nucleon magic numbers assuming that a single nucleon is placed in an orbit above a closed shell or that a single nucleon is removed from an orbit below a closed shell. The orbits gets filled up in the sequential order $1s \rightarrow 1p \rightarrow 1d,\ 2s....$ The shell model can predict the ground state spin and parity of a given nucleus. In case of even-even nuclei the ground state spin is 0. As all the particles gets paired up (all the magnetic sub-states are filled, $m_j = -j,\ (-j+1), ... + j$) and hence have the total angular momentum as zero. The parity for a given state is given by $(-1)^l$. In even-even nuclei parity is always positive. Hence the ground state spin and parity of a given even-even nucleus is given by $J^\pi = 0^+$.

Now let us consider the nucleus ^{24}Mg($Z = N = 12$). The nucleons would be distributed as

$$(\pi \rightarrow ((1s_{1/2})^2, (1p_{3/2}, 1p_{1/2})^6) \otimes (1d_{5/2})^4)$$
$$(\nu \rightarrow ((1s_{1/2})^2, (1p_{3/2}, 1p_{1/2})^6) \otimes (1d_{5/2})^4)$$

Hence, this nucleus would have $J^\pi = 0^+$ as it's ground state. The valence nucleons can be distributed within the $1d_{5/2}, 1d_{3/2}, 2s_{1/2}$ orbitals. Since these orbitals have an even l, the resulting states would have a positive parity. The distribution of these nucleons within the *sd* orbitals, would result in a maximum angular momentum of $J^\pi = 12^+$, which originates from the configuration $(\nu((1d_{5/2})^3, (1d_{3/2})^1))(\pi((1d_{5/2})^3, (1d_{3/2})^1))$. The negative parity states would however originate from the excitation of a single nucleon from *sd* orbital into the next major oscillator shell *i.e.* into the *pf* orbital. Hence, the energy of the lowest (first) negative-parity state encodes the information about the $sd - pf$ shell gap.

For even-odd nucleus or odd-even nucleus the ground state spin and parity is determined from the spin and parity of the unpaired nucleon. For example in case of ^{25}Mg nucleus the unpaired neutron would occupy the $1d_{5/2}$ orbital, which has a even l. Hence, it's ground state spin would be $J^{\pi} = 5/2^{+}$. However, for odd-odd nucleus the ground state spin and parity is determined following the Nordheim rule [54]. For such a nucleus, if j_n and j_p correspond to the resultant angular momentum from the partially filled neutron and proton shells, and l_p and l_n are the orbital angular momentum quantum number for partially filled proton and neutron orbitals, then the total spin J of the ground state for the odd-odd nucleus is given by the following rules :

$$\begin{aligned} J = |j_p - j_n|, \quad if \quad l_p + j_p + l_n + j_n \; is \; even \\ |j_p - j_n| < J \leq j_p + j_n, \quad if \quad l_p + j_p + l_n + j_n \; is \; odd \end{aligned} \tag{76}$$

Example ^{32}P we have, $Z = 15$ & $N = 17$, and the last unpaired nucleon occupies the $2s_{1/2}$ and $1d_{3/2}$ orbitals. Hence $l_p = 0$ & $l_n = 2$ and $j_p = 1/2$ & $j_n = 3/2$, and $l_p + j_p + l_n + j_n = 4$, and therefore the ground state spin would be 1^{+} (parity is positive as the orbitals under consideration are have even l). Thus this model adequately describes the level properties of nuclei in the immediate vicinity of magic numbers.

4.4 Large Basis Shell Model Calculations

With the recent advances in computational power, it is now feasible to undertake the spherical shell model calculations for nuclei with a few valance nucleons outside the magic core. The aim of such a computationally intense calculations is to arrive at a detailed understanding of the observed level structure including the excited levels. The Shell Model Hamiltonian is written as

$$\begin{aligned} H &= T + V \\ &= \sum_{i=1}^{A} [\frac{p_i^2}{2m}] + \sum_{i>k=1}^{A} V_{ik}(r_1, r_2) \\ &= \sum_{i=1}^{A} \left[[\frac{p_i^2}{2m}] + U_i(\vec{r}) \right] + \sum_{i>k=1}^{A} V_{ik}(r_1, r_2) - \sum_{i=1}^{A} U_i(\vec{r}) \end{aligned} \tag{77}$$

Where the shell model assumes that most of the effects of the two body interactions $V_{ik}(r_1, r_2)$ can be absorbed into an equivalent one-body central potential $U_i(\vec{r})$, such

that

$$
\begin{aligned}
H &\approx H_1(r_1) + H_{12}(r_1, r_2) \\
H_1(r_1) &= \sum_{i=1}^{A} \left[[\frac{p_i^2}{2m}] + U_i(\vec{r})] \right] \\
H_{12}(r_1, r_2) &= \sum_{i>k=1}^{A} V_{ik}(r_1, r_2) - \sum_{i=1}^{A} U_i(\vec{r})
\end{aligned}
\tag{78}
$$

The calculations that follow assumes that $H_{12}(r_1, r_2)$ is small enough to be treated as a perturbation. The methodology adopted for such calculations is detailed in Ref.[55], and could be summarized as:

1. Choice of $H_1(r_1)$, the central potential, which is usually assumed as the sum of a spherical harmonic oscillator potential, a spin-orbit interaction $(\vec{l}.\vec{s})$, and a term proportional to l^2.

2. Choice of inert core and the model space, (the orbits available to the valence nucleons).

3. Calculation of the one-particle eigenstates of $H_1(r_1)$ in the desired model space.

4. Construction, of the multi-nucleon eigenstates, of H, for a given number of nucleons.

5. Specification of a residual two-body interaction of $H_{12}(r_1, r_2)$, for the desired model space.

6. Evaluation of the matrix elements of $H_{12}(r_1, r_2)$ and calculation of the eigenvalues and eigenvectors of this matrix.

For a set of calculations, we specify H_1 and H_{12}, and define the valence orbits that are to be included in the model space for computation. This in turn decides the inert core. Given this information there are a number of computer codes, such as OXBASH [56], NuShellX@MSU [57], Antoine [58] with which it is possible to construct the complete set of basis states, calculate the matrix elements of H_{12}, and then diagonalize H_{12} in this basis. With the matrix diagonalized, we solve for the eigenvectors and values,

$$
H|\Psi >= E|\Psi > . \tag{79}
$$

The eigenvectors can then be used to compute the matrix elements of other operators which yield predictions of strengths for observables, *i.e.* the electric, $B(EL)$, and magnetic, $B(ML)$, multipole (L) transition probabilities and the singular or multiple nucleon transfer spectroscopic factors.

In reality, the exact eigenvectors and eigenvalues of the nucleus can, in principle, be obtained by solving the Schrödinger equation of the exact nuclear (assuming the particles are free to move in all the orbits)

$$H|\Psi_i >= E|\Psi_i > . \tag{80}$$

However, such calculations are computationally intensive to the extent that they are impossible. The shell model circumvents this problem by assuming that there is an effective Hamiltonian $\mathcal{H}$ appropriate for the truncated model space $|\phi\rangle$, a practical subset of the complete nuclear Hilbert space $|\Psi\rangle$, such that

$$\mathcal{H}|\phi_i >= E|\phi_i > . \tag{81}$$

Hence, all practical shell model calculations which utilize the effective Hamiltonian, $\mathcal{H}$ it is imperative to use analogous effective operators $\grave{O}$ on the wave functions of the states, to calculate the value of the any observable $i.e < \Psi_f|O|\Psi_i > \rightarrow < \phi_f|\grave{O}|\phi_i >$.

Electromagnetic interaction, which is a weak interaction, is well understood with the help of perturbation theory. The transition rates are calculated from the perturbation theory using the Fermi's golden rule, where the transition probability is given by:

$$W = \frac{2\pi}{\hbar} |\langle \Psi_f| |H_{em}| |\Psi_i\rangle|^2 \rho(E_f) \tag{82}$$

Where initial and final states of the wave functions are $\langle\Psi_i|$ and $\langle\Psi_f|$ respectively, $\rho(E_f)$ is the density of final states, the number of states per unit energy interval and H_{em} is the electro-magnetic perturbation. Hence, the transition probability [25, 46] from a state j_i to final state j_f connected by a γ-ray of energy E_γ, of multipole order l is given by:

$$W(\lambda l) = \frac{8\pi(l+1)}{\hbar l((2l+1)!!)^2} \left(\frac{E_\gamma}{\hbar c}\right)^{(2l+1)} B(\lambda l : J_i \rightarrow J_f) \tag{83}$$

Where $B(\lambda l : J_i \rightarrow J_f)$ is the reduced transition probability, and for an electric and magnetic transition, it can be expressed as

$$B(El) = \frac{1}{2J_i+1} |\langle J_f || \hat{Q}^l || J_i \rangle|^2 \tag{84}$$

and

$$B(Ml) = \frac{1}{2J_i+1} |\langle J_f || \hat{M}^l || J_i \rangle|^2. \tag{85}$$

Where $\hat{Q}^l$ and $\hat{M}^l$ are the electric and magnetic multipole operators respectively. For transition $|f\rangle \rightarrow |i\rangle$ the reduced transition probability is denoted by $B(\lambda l \downarrow)$ and for the transition $|i\rangle \rightarrow |f\rangle$ the reduced transition probability is denoted by $B(\lambda l \uparrow)$ are related as

$$B(\lambda l \uparrow) = \left(\frac{2J_f+1}{2J_i+1}\right) B(\lambda l \downarrow). \tag{86}$$

The transition probability $W(\lambda l)$, is expressed as the number of decays per unit time. If $B(El)$ and $B(Ml)$ are expressed in units of $e^2 fm^{2l}$ and $\mu_N^2 fm^{2l-2}$ respectively, then $W(\lambda l)$ and $B(\lambda l)$ are related as

$$W(\lambda l) = \alpha \hbar c \frac{8\pi(l+1)}{\hbar l((2l+1)!!)^2} \left(\frac{E_\gamma}{\hbar c}\right)^{(2l+1)} B(\lambda l) \; in \; e^2 fm^{2l} \tag{87}$$

and

$$W(\lambda l) = \alpha \hbar c \left(\frac{\hbar c}{2m_p c^2}\right)^2 \frac{8\pi(l+1)}{\hbar l((2l+1)!!)^2} \left(\frac{E_\gamma}{\hbar c}\right)^{(2l+1)} B(\lambda l) \; in \; \mu_N^2 fm^{2l-2}. \tag{88}$$

Where $e^2 = \alpha \hbar c = 1.44 \; MeVfm$, $\alpha = 1/137$ is the fine structure constant and m_p is the mass of proton and $\mu_N = e\hbar/2m_p c^2$ is the nuclear magneton. After substituting all the values in above equations the transition probability for the three lowest multipole order is given by [59]

$$\begin{aligned}
W(E1) &= 1.59 \times 10^{15} \; E_\gamma^3 B(E1) \\
W(E2) &= 1.23 \times 10^{9} \; E_\gamma^5 B(E2) \\
W(E3) &= 5.71 \times 10^{2} \; E_\gamma^7 B(E3) \\
W(M1) &= 1.76 \times 10^{13} \; E_\gamma^3 B(M1) \\
W(M2) &= 1.35 \times 10^{7} \; E_\gamma^5 B(M2) \\
W(M3) &= 6.31 \times 10^{0} \; E_\gamma^7 B(M3).
\end{aligned} \tag{89}$$

The reduced transition probability can be calculated from the experimentally obtained lifetime (τ), branching ratio (BR), mixing ratio (δ), conversion coefficient (α) and the gamma energy (E_γ). The reduced transition probability for electric and magnetic transition can be expressed in units of e^2fm^{2l} and $\mu_N^2 fm^{2l-2}$ respectively and E_γ is in MeV.

$$\begin{aligned}
B(E1) &= \frac{0.693}{E_\gamma^3}\frac{BR}{\tau(1+\alpha)}\frac{\delta^2}{1+\delta^2}, (\tau\ is\ in\ fs)\\
B(E2) &= \frac{816}{E_\gamma^5}\frac{BR}{\tau(1+\alpha)}\frac{\delta^2}{1+\delta^2}, (\tau\ is\ in\ ps)\\
B(E3) &= \frac{1760}{E_\gamma^7}\frac{BR}{\tau(1+\alpha)}\frac{\delta^2}{1+\delta^2}, (\tau\ is\ in\ \mu s)\\
B(M1) &= \frac{56.8}{E_\gamma^3}\frac{BR}{\tau(1+\alpha)}\frac{1}{1+\delta^2}, (\tau\ is\ in\ fs)\\
B(M2) &= \frac{74.1}{E_\gamma^5}\frac{BR}{\tau(1+\alpha)}\frac{1}{1+\delta^2}, (\tau\ is\ in\ ns)\\
B(M3) &= \frac{0.158}{E_\gamma^7}\frac{BR}{\tau(1+\alpha)}\frac{1}{1+\delta^2}, (\tau\ is\ in\ s).
\end{aligned} \tag{90}$$

As mentioned earlier, the shell model wave functions are then used to calculate the overlap of the initial and final states, where operated by either electric and/or magnetic operator [60]. The $M1$ operator is

$$(M1)^{op} = \sqrt{\frac{3}{4\pi}}\sum_{i,\tau_z}\left[g_{s\tau_z}\vec{s}_{i,\tau_z} + g_{l\tau_z}\vec{l}_{i,\tau_z} + g_{t\tau_z}\sqrt{8\pi}\left[Y^2(\hat{r}_{i,\tau_z})\otimes\vec{s}_{i,\tau_z}\right]^{(1)}\right]\mu_N \tag{91}$$

Now, the $M1$ transition matrix elements, which is an observable is given by

$$M(M1) = \langle\Psi_f|\,|(M1)^{op}|\,|\Psi_i\rangle \tag{92}$$

For an electric transition, we have

$$(E2)^{op} = \sum_{i,\tau_z} e_{\tau_z} r_{i,\tau_z}^2 Y^2(\hat{r}_{i,\tau_z})e \tag{93}$$

Now, the $E2$ transition matrix elements, which is an observable is given by

$$M_p = \langle\Psi_f|\,|(E2)^{op}|\,|\Psi_i\rangle \tag{94}$$

The transition matrix elements, in turn are related to the corresponding transition probabilities [60] as

$$\begin{aligned}
B(M1) &= \frac{[M(M1)]^2}{(2J_i+1)}\\
B(E2) &= \frac{{M_p}^2}{(2J_i+1)}
\end{aligned} \tag{95}$$

As mentioned earlier, the use of a restricted model space, demands, that we use effective values for the charges, g-factors etc. These would be model dependent hence, are not universal, and may have to be obtained from a consistent fit to the experimental observables, for a given model space.

In the present thesis the shell model calculations have been performed using the code NuShellX@MSU [57]. For example, if we wish to predict the level structure of the positive parity states in ^{24}Mg, then from a purely practitioners hands-on-approach to a shell model calculation, we would

1. Identify the inert core, which is this case would be ^{16}O. Hence we have total 8 valence nucleons.

2. Identify the valence orbits in which the nucleons outside the core are free to move *i.e* choose the model space. The 8 valence nucleons would be allowed to occupy the $2s_{1/2},\ 1d_{3/2},\ 1d_{5/2}$ orbitals, which have $l = 0,\ 2$, and hence would generate positive parity sequences only. The negative parity sequences, would require the excitation of a single nucleon from the *sd* orbitals into the fp orbitals, and the model space would have to be accordingly expanded to include these orbits, which is schematically represented in Fig. 26.

3. Identify the two-body matrix elements for this model space. Usually we have a one-to-one correspondence between the model space and the two-body matrix elements. Hence the choice of the two is kind of inter-leaved.

4. Run the shell model code with the above inputs to obtain the energy eigenvalues and use the wave functions (within the same model space and interaction) to calculate the overlaps, when operated by an effective operator to deduce an observable.

For the above example, we shall use the *sd* model space, and the recently developed interaction codenamed $USDA$ [61], in the code NuShellX@MSU [57]. Since, unrestricted shell model calculations are feasible for this model space, no truncation scheme was adopted. The calculations have predicted the ground state energy as -87.13 MeV, which is in excellent agreement with the experimental value of -87.10 MeV. The

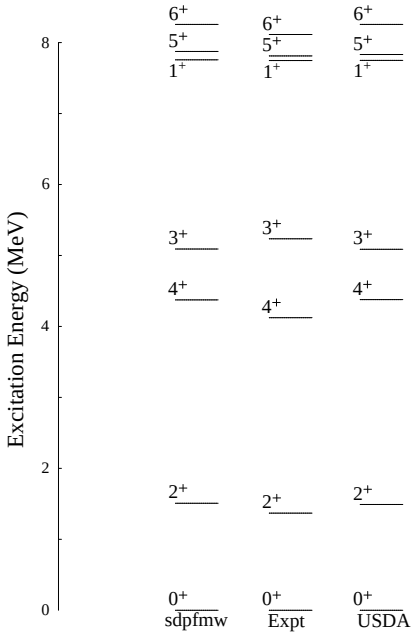

FIG. 27: Comparison of experimentally observed and shell model calculated energy levels in ^{24}Mg nucleus by using $USDA$ and $sdpfmw$ interactions (only for positive parity states).

calculated excitation energies for the low-lying positive parity states (up to $J^{\pi} = 6^{+}$) are compared with the reported [23] value in Fig. 27. The same exercise was extended to a larger model space which now encompasses the $sd - pf$ shells. The corresponding interaction chosen, was codenamed $sdpfmw$ [9]. Unrestricted calculations within such a large model space was not computationally feasible. Hence, the model space was internally truncated by considering no nucleon excitation into the *fp* orbits *i.e*, we used the $0\hbar\omega$ restriction (0 refers to the number of nucleons excited across one major shell). The predicted ground state energy is -87.08 MeV, which is in excellent agreement with the experimental observation. This is indicative of an appropriate truncation scheme used. The predicted excitation energies are also compared in Fig. 27 with the reported values.

The detailed shell model calculations for both the positive and negative parity states for isotopes of Mg and Si are detailed in the subsequent chapters. The model calculations helps us elucidate the underlying microscopic configurations for the established levels.

Chapter - 5

Spectroscopic Study of Mg Isotopes

The present thesis work details for the first time, a high resolution $\gamma - \gamma$ coincidence spectroscopic study of the ^{26}Mg nucleus populated following heavy-ion induced fusion-evaporation reaction involving ^{13}C + ^{18}O, with ^{13}C beam of energy 30 MeV. The de-exciting γ-transitions were detected using the multi-detector array, Indian National Gamma Array (INGA). The experimental findings, are presented in this chapter. Further, large basis shell model calculations, involving cross-shell excitations have been carried out for ^{26}Mg and the neighboring isotopes to gauge the evolving shell structure in this region.

5.1 Introduction

Nucleus, being a few-body system, provides us with a unique laboratory to explore the two extreme degrees of freedom *viz.* single particle and collective excitations, as well as their interplay. The spherical shell model is one of the fundamental microscopic models, to help us understand the nuclear structure and it's behaviour under extreme conditions of excitation energy and angular momentum. The spectroscopy of *sd* shell nuclei, provide us an appropriate testing ground for the validity of the spherical shell model. It has been well established that the shell model predictions are expected to be very close to the experimental observations, for nuclei with nucleons near the shell closure. Increase in the the number of nucleons in the valence orbitals (outside the inert core) leads to the development of collectivity. The shell model being a fundamental microscopic model can in principle be used to interpret the evolving nuclear structure as we progress from the vicinity of shell closure towards the mid-shell region (as we increase the number of valence nucleons). The main bottle-neck in performing these calculations is the numerical difficulty of computing wave functions and elements for

very large-scale shell model calculations. However, the nuclei in the *sd* and at the interface of the *sd-pf* shells require a moderately smaller number of valence nucleons compared to the rare earth nuclei, to successfully attempt an unified interpretation of the observed single particle and collective excitations within the shell model. From this perspective, the nuclei at the vicinity of the *sd-pf* shells such as Mg, Si isotopes offer us a rather unique region to explore the aforementioned features, both experimentally as well as within the theoretical framework. The generation of negative parity states, in the *sd* (*even* l) shell nuclei, demands atleast one nucleon excitation into the *fp* (*odd* l) shell. The occupation of the high j ($f_{7/2}$) orbital is expected to lead to the onset of deformation in these nuclei. Further, the nuclei occupying the mid-shell region, such as ^{26}Mg, ^{29}Si have sufficient nucleons within the *sd* shell, which could support the commencement of deformation, even for positive parity levels.

The isotopic chain of Mg isotopes, exhibit evolving structural characteristics [62–64] (changes in shape as well as deformation) as a function of the neutron number. These isotopes also span the crucial region, in the nuclear landscape where a transition is expected from the prolate to oblate deformation. The $N = Z$, ^{24}Mg isotope displays a deformed ground state and ^{25}Mg is an ideal candidate of quadrupole deformed nuclei [64]. The experimentally observed level energies and the γ-decay branches of ^{25}Mg [64] are in agreement with the shell model calculations. Further the addition of neutrons leads to quite rapid changes in the shape, deformation and the spin structure. The next even-even Mg isotope, ^{26}Mg displays shape coexistence indicating both a prolate and an oblate minima corroborating the highly transitional behaviour assigned to it. The calculations using constrained Hartree-Fock-Bogoliubov + QRPA model demonstrate the β and γ-soft character of the nucleus [65]. The positive parity states of ^{27}Mg nucleus were successfully described by Brendler *et al.* [62] within the framework of the spherical shell model, and the negative parity states were elucidated by the rotational model. In all these nuclei, the lowest negative parity level has a significant connotation, as it encodes the information of the shell gap between the *sd* and *fp* orbitals. This gap has a crucial bearing on our understanding the origin of the *island of inversion*.

Further, all the earlier experimental investigations were carried out using modest number of detectors, and light-ion reactions. Recent advances in the available com-

putational resources coupled to the development of updated and realistic residual interaction used to approximate the nucleon-nucleon interaction, have made large basis shell model calculations feasible for these nuclei. Hence, there is a need to revisit the level structure of nuclei ($A \sim 30$), which belong to the interface of the *sd* and *fp* shells, using the available state-of-the-art facilities, both experimental as well as theoretical.

5.2 Previous Investigations on Mg Isotopes

The Mg isotopes provide us with one of the earliest and best examples of nuclei exhibiting an intriguing interplay between the single particle as well as collective degrees of freedom. As we increase the number of neutrons, one expects the onset of deformation, which indeed in observed in Mg isotopes. However, the isotopes with mass number $A = 27 - 29$, cover a critical region, where the transition from prolate to oblate deformation is observed [62]. For example, the earlier investigations on the level structure of ^{25}Mg nucleus were carried out using α-induced reactions [63, 66] and heavy-ion induced reaction ^{12}C(^{14}N,pγ)^{25}Mg at 23.5 MeV [64], but the investigations were limited due to the use of modest detector setups (such as scintillator or Ge(Li) detectors) , even though they exploited the power of particle gated gamma spectroscopy. Christiansson and co-workers [66] also performed coincidence measurements, using a Ge(Li) detectors. The experimental findings are discussed in terms of rotational model based on both the single particle and $2p - 1h$ excitations [63]. The low lying states of ^{25}Mg were grouped into rotational bands, labeled by the K ($K^\pi = 5/2^+$, $K^\pi = 1/2^+$, $K^\pi = 1/2^-$) quantum number. As expected some of the sequences exhibited a single particle nature, but for one of the band the excitation energies follow the $J(J+1)$ trend, reminiscent of a rotational nature.

All the previous investigations on the level structure of ^{26}Mg were performed using light ion induced reactions. The reactions primarily used were ^{25}Mg(n,γ), ^{25}Mg(d,pγ), ^{26}Mg(p,p$'$), ^{24}Mg(t,p), ^{23}Ne(α,pγ) which are summarized in [23]. In the present work we shall essentially restrict our discussions to the work of Glatz and co-workers [13], who utilized the ^{23}Na(α,pγ) reaction at 14.2 and 16 MeV energy to populate and

investigate the high spin states in ^{26}Mg. They established the level structure upto $E_x \sim 12.5$ MeV and $J^\pi = 8^+\hbar$. The use of an annular $E - \Delta E$ telescope at 180^o with respect to beam facilitated detection of protons, in coincidence with the γ-rays which were detected by two 120 cm^3 Ge(Li) detectors. The proton gated γ-ray spectrum was used to establish the level scheme. The γ-ray angular correlations, measured at 14.2 MeV energy were used to obtain information on the multipolarity of the de-exciting γ-transitions. Mixing ratios were also extracted from these measurements. In absence of polarization measurements, the electro-magnetic nature, was arrived at from elimination of unrealistic transition rate considerations, for example the parity changing character was excluded if the M2 transition rate exceeds the recommended upper limit of 3 W.u. Lifetime measurements using the DSAM technique were also attempted by Glatz *et al.*. The measurements were aimed for the short lifetimes which are expected for higher excited states, to establish the collective features of the level structure.

The spherical shell model was the obvious choice to elucidate the observed level structure. The shell model calculations were performed using the unified $s - d$ shell Hamiltonian, for the positive parity states and the predicted excitation energies were in close agreement with the experimental observations. The presence of enhanced in-band $E2$ transitions, were indicative of the possibility of rotational nature to the established level structure of ^{26}Mg. Accordingly, Glatz and co-workers identified five rotational bands, with respective band-head as 0^+_1, 2^+_1, 3^+_1, 0^+_2, $(2)^+_2$ and 3^-. Shell model calculations within the *sd* model space, are indicative of the collective behaviour in this mid-shell nucleus. The shell model wave functions were used to obtain the transition probabilities, from where the intrinsic quadrupole moment, $|Q_o|$ was deduced. The changing sign and magnitude of the intrinsic quadrupole moment provided indications to a corresponding shape evolution. Thus presenting us with evidence for the existence of soft deformation, which is characteristic of such mid-shell nuclei.

The investigation of the level structure of ^{27}Mg was carried out primarily using the $^{26}Mg(d,p)$ reaction by Brendler *et al.* [62], upto $\sim$ 8 MeV in excitation energy. The γ-rays were detected by using the earlier generation detectors such as Ge(Li) and NaI(Tl) detectors. Brendler and co-workers, also studied the proton-γ-ray angular correlations, and based their spin parity assignments on these measurements. The

low-lying level structure ($E_x \sim 5$) MeV, could be reasonably explained using the spherical shell model calculations within the *sd* shells. It is interesting to note that the rotational model was successful in explaining the negative parity states. These model calculations were indicative of an oblate deformation for this nucleus.

The experimental information available on the level structure of ^{28}Mg, is very sparse, and is limited to studies using light-ion induced reactions. Recently, the level scheme of ^{28}Mg nucleus was extended upto $E_x = 8.4$ MeV and $J^\pi = 6^+$, [67] using deep-inelastic and multi-nucleon transfer reactions, wherein ^{26}Mg beam at an energy of 160 MeV was made incident on a thin ^{150}Nd target. The positive parity sequences could be explained within the shell model framework. However, the calculations using the adiabatic model for triaxially deformed rotor, were also successful in interpreting the observed level sequences in this nucleus. Recent microscopic calculations with antisymmetrized molecular dynamics [68] are suggestive of molecular states in this region. The results signified the dominance of nucleon clusters in these nuclei.

However, all aforementioned shell model calculations, were restricted to positive parity states, since, the generation of negative parity levels, demands the occupation of the *fp* shell, and the resulting model space was beyond the computational facilities available in the late 80's. The earlier investigations on these nuclei have established, the presence of both single particle as well as deformed states, even at moderate spins and excitation energies. Presence of such diverse structural characteristics open them up as the chosen subjects for several contemporary pursuits, as in the present thesis.

5.3 Present Work on Spectroscopy of ^{26}Mg

The ^{26}Mg nucleus for the present study was populated by using the ^{18}O(^{13}C,αn) reaction. The predictions of the statistical model code, PACE4 [69] for this reaction is presented in Fig. 28. The incident beam energy was chosen as 30 MeV, owing to the predicted significant population at this energy for nuclei of interest in this work, such as ^{29}Si and ^{26}Mg. The ^{13}C beam was provided by the BARC-TIFR Pelletron

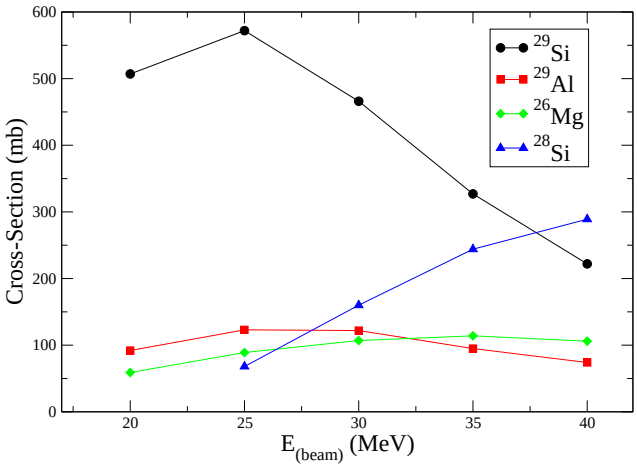

FIG. 28: Predictions of the statistical model PACE4 for the ^{13}C + ^{18}O reaction depicting the production cross sections for ^{26}Mg, ^{29}Al and $^{28,29}Si$ nuclei.

Linac facility at Mumbai. The beam current during the experiment as monitored in the last Faraday cup was typically $8 - 10$ nA during the experiment. The terminal potential was at 5.974 MV. The neutron rich ^{18}O target was prepared by heating a 50 mg/cm^2 thick Ta foil in an atmosphere of enriched ^{18}O in the form of Ta_2O_5. The total equivalent thickness of ^{18}O was estimated to be $\sim$ 1.6 mg/cm^2 considering both the sides of Ta foil. The thickness of the Ta foil was sufficient to stop the beam and hence the reaction occurred only on the side facing the beam while the ^{18}O layer on the opposite side (away from the beam) did not contribute to the reaction. The de-excited γ-rays are detected using the Indian National Gamma Array (INGA) (pictorial view of this setup has been presented in chapter 2) which at the time of the present experiment consisted of 15 Compton suppressed Clover detectors. The distance from the target to the front face of the detector is $\approx$ 25 cm.

The detectors were placed at 40^o, 65^o, 90^o, 115^o, 140^o and 157^o with respect to the beam direction. The typical rates in the individual Clover crystals, during the experiment were $\sim 5 - 6$ kcps. The expected total full-energy peak detection efficiency for this configuration was $\sim$ 4%. Two and higher fold Clover coincidence events were recorded with the help of a digital data acquisition system based on the Pixie-16 modules from M/S XIA LLC [38]. The DAQ system comprised of 4 Pixe-16 modules,

where each module processed the inputs from 4 Clovers. The data from each module was stored in individual files, which were later merged to form a single file for each run. This data was then subjected to a rigorous data analysis, to establish the detailed level structure of ^{26}Mg. In total we have recorded about 1.6×10^9 two and higher fold coincidence events.

Due to the dominance of single particle excitations in these nuclei, we expect high energy γ-transitions ($E_\gamma \geq 2$ MeV). Hence, the energy calibration was carried out using source data and residue radioactivity, which would provide us data points in the high energy regime. The energy calibration has been done using a polynomial of fourth degree and a square root term, ($E_\gamma = a_0 + a_1x + a_2x^2 + a_3x^3 + a_4x^4 + a_5\sqrt{x}$) using the *ROOT* package [70]. The results for one such representative exercise is illustrated in the Fig. 29. Following the energy calibration, the data was gain matched to an constant energy dispersion of 1 keV per-channel (*epc* = 1). This ensures that the individual detector and electronic dependence has been eliminated. A correct gain matching is of importance when we obtain the add-back spectra. Any errors in the calibration and the gain matching exercise would result in a deterioration of the peak centroid and *fwhm* in the add-back spectrum, which is used in the final analysis. The results of this exercise for one representative Clover detector data is pictorially depicted in the Fig. 30 for $E_\gamma = 356$ & 1408 keV. As is evident from the figure, the peaks from individual channels have been aligned and the add-back spectrum does not indicate any broadening in the *fwhm* or a shift in the *centroid*. This ensures that all the necessary pre-sorting has been correctly performed. The data was then sorted into the conventional symmetric and angle dependent E_γ - E_γ matrices using the *"MARCOS"* [39] and analyzed using the RADWARE [45] package. The placement of the γ-transitions in the level scheme was based on the observed $\gamma - \gamma$ coincidence relationships.

The information on the dominant multipolarity of the γ-transition is obtained from the observed coincidence angular anisotropy (as discussed in chapter 3). The presence of a Doppler shift / shape does not allow us to set the gates at either the forward or backward angles. As seen in the Fig. 31, the observed Doppler shape at angles other than 90^o, demands that we set a considerable wide gate, as a result the resultant gated spectrum would have considerable contamination from neighbouring peaks from other

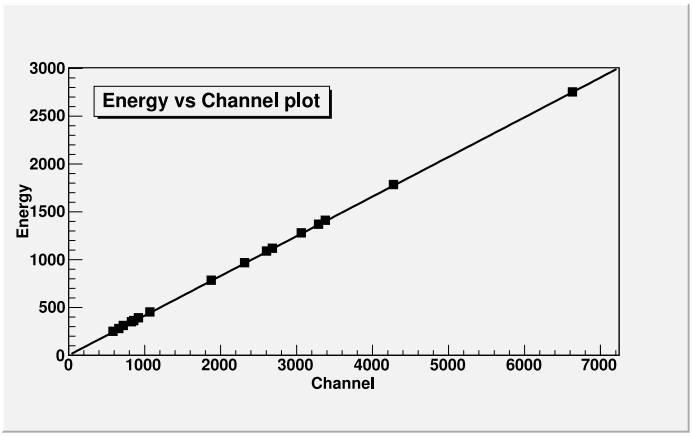

FIG. 29: Energy calibration : relation between *channel* and E_γ.

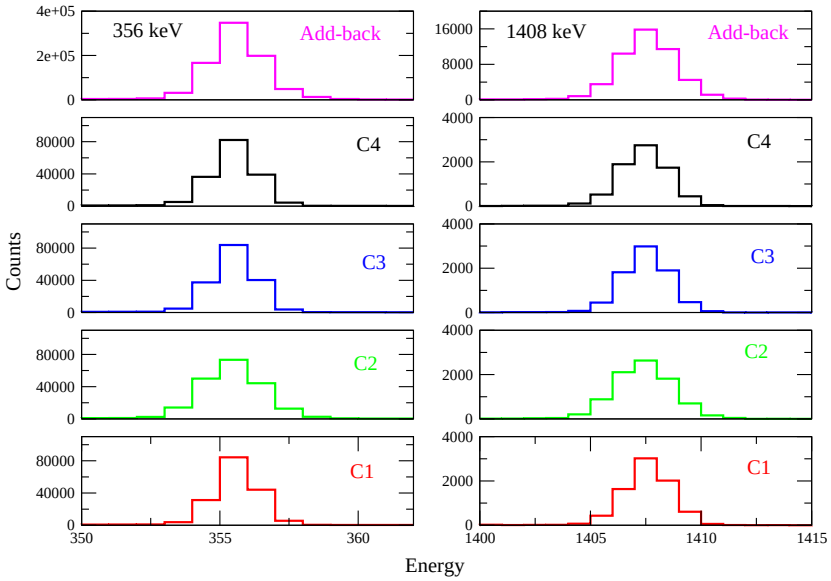

FIG. 30: Spectra from 4 crystals (C1 - C4) of a Clover depicting the 356 & 1408 keV peaks after the gain matching procedure. As is evident from the figure, the data is now detector independent. The add-back spectrum, shows no appreciable deterioration in the *fwhm* and the energy peak is at the desired position.

nuclei.

To circumvent this problem of determining the R_{DCO} values (which requires gates to be set on either the forward or backward angles *w.r.t* beam direction), a parameter termed as anisotropy ratio [9], defined below, was used for assigning multipolarity of

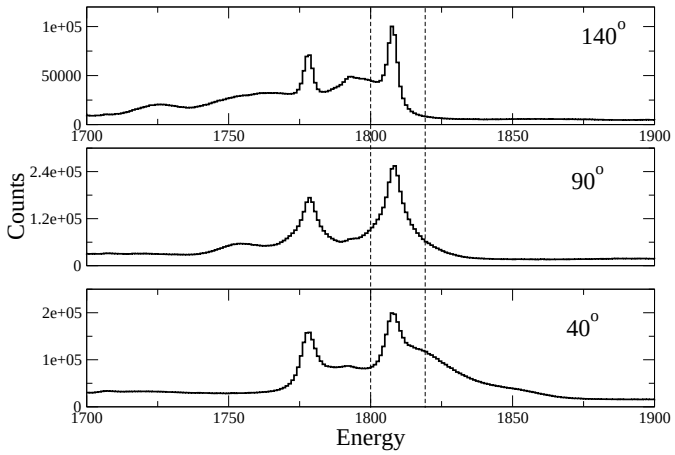

FIG. 31: Part of the projection spectra at 140^o, 90^o, 40^o, highlighting the prominent Doppler shapes, which does not permit us to set gates at various angles.

the observed γ-transitions.

$$R_{anisotropy} = \frac{I_{\gamma 1}\ (at\ 40^\circ\ gated\ by\ \gamma 2\ at\ 90^\circ)}{I_{\gamma 1}\ (at\ 65^\circ\ gated\ by\ \gamma 2\ at\ 90^\circ)}. \tag{96}$$

The anisotropy ratio ($R_{anisotropy}$) for the transitions of interest is obtained from matrices with detectors at particular angles (say at 40°, or 65° with respect to the beam axis) on the Y-axis, and 90° detectors on the X-axis. The results for transitions of known multipolarity are shown in Fig. 32. The expected $R_{anisotropy}$ for dipole and quadrupole transitions was determined from the weighted average of the experimental $R_{anisotropy}$ for transitions of known multipolarity and for dipole transitions has been found to be 0.95 (in a dipole gate) and 1.13 (in a quadrupole gate), while that for quadrupole transitions has been calculated to be 1.82 (dipole gate) and 1.68 (quadrupole gate). $R_{anisotropy}$ values for the remaining transitions were determined in the appropriate gates, following which the multipolarity was assigned to them. The results are presented in Fig. 32. The figure, establishes the feasibility of the the anisotropy method to distinguish between transitions of different multipolarities. However, it is not easy to unambiguously determine the mixing ratio from the $R_{anisotropy}$ measurements.

As discussed in chapter 3, it is possible to extract the mixing ratio, from the angular distribution measurements. This method requires the efficiency corrected

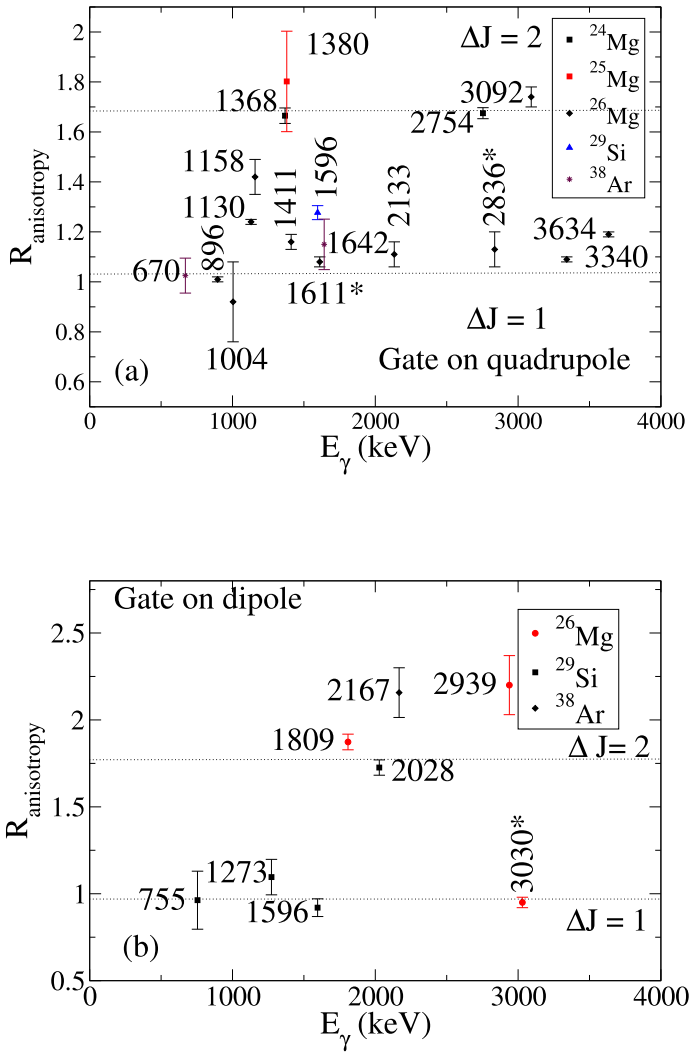

FIG. 32: The experimental $R_{anisotropy}$ values for transitions in ^{24,25,26}Mg, ^{29}Si and ^{38}Ar. The newly identified γ-rays in ^{26}Mg are marked with an asterisk. To guide the eye lines corresponding to the weighted average of $R_{anisotropy}$ for transitions of known multipolarity have been drawn.

angle dependent intensities preferably from the singles measurements to obtain the angular distribution coefficients (A_{22} and A_{44}). Fig. 33 illustrates the fit to the angular distribution data for the 1130 keV ($2_2^+ \rightarrow 2_1^+$) transition in ^{26}Mg nucleus obtained in the present work. The mixing ratio (δ) has been obtained following the conventional χ^2 minimization [50]. Fig. 33 depicts the χ^2 plot for this transition. Following the convention of Rose and Brink, the obtained mixing ratio, is $\delta = 0.14 \pm 0.05$, which is in conformance with the reported value of 0.12 ± 0.02 [23]. The contaminations from the other channels, Doppler effects and sparse statistics, prevented us from applying

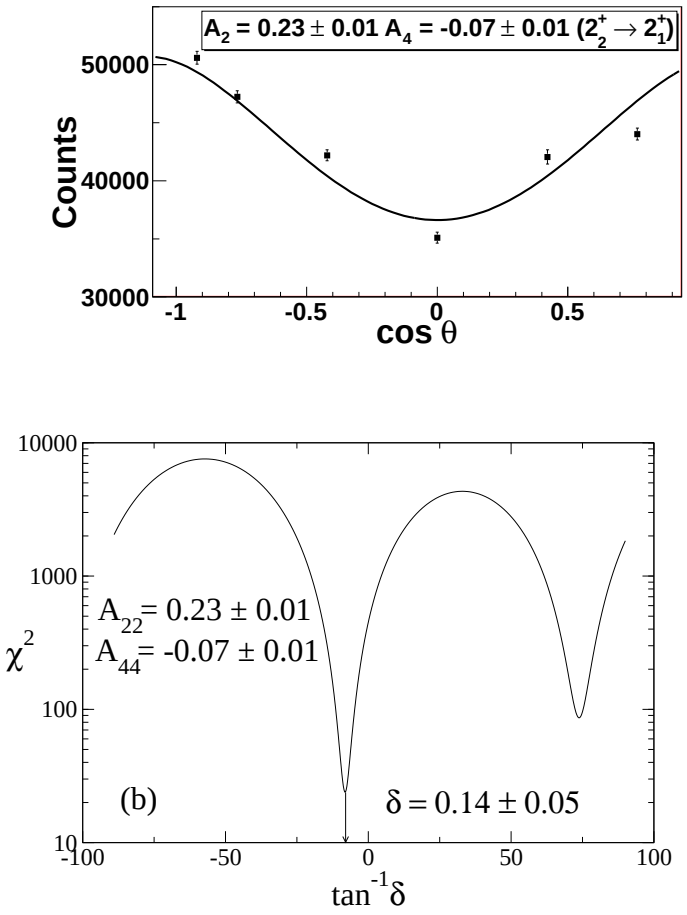

FIG. 33: Angular distribution fit for 1130 keV ($2_2^+ \rightarrow 2_1^+$) transition in ^{26}Mg and the χ^2 analysis to obtain the corresponding mixing ratio.

this technique to other transitions in ^{26}Mg.

One of the unique advantage of the Clover detector due to it's composite character is it's efficient use as a Compton polarimeter. Linear Polarization measurements help us to uniquely conclude about the electro-magnetic nature of the γ-ray transitions. Each crystal of the detector is the scatterer with the adjacent two crystals as absorbers along the perpendicular and parallel direction, with respect to the reaction plane. Electric and magnetic transition can be distinguished from the observed anisotropy between the number of perpendicular and parallel Compton scattered events, which is quantified from the value of $\Delta_{Pol}\big(= \frac{aN_\perp - N_\parallel}{aN_\perp + N_\parallel}\big)$, which besides the scattering anisotropy, depends on the geometrical asymmetry factor $a(E_\gamma)$ for the particular experimental configuration.

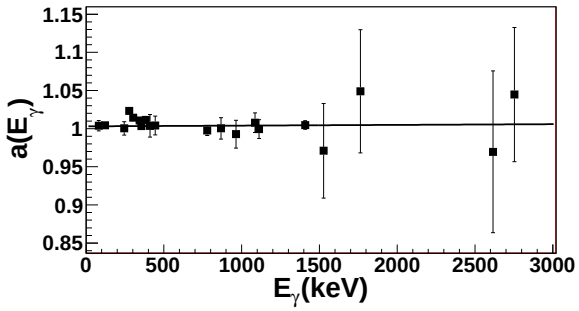

FIG. 34: Plot of the asymmetry factor "a"as a function of γ-ray energy for the Clover detector placed at 90^o with respect to the beam direction in the present setup.

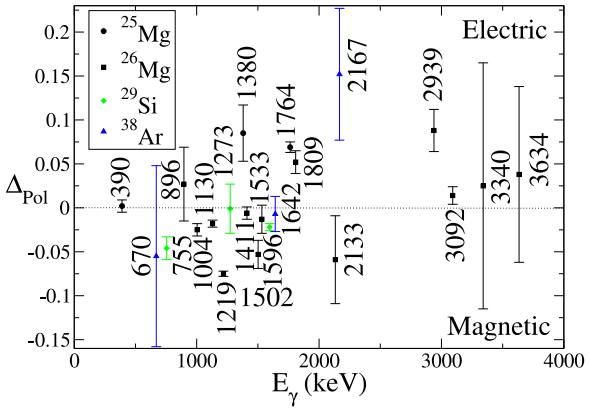

FIG. 35: Plot for the polarization asymmetry for γ-ray transitions observed in the current experiment.

The energy dependence of the $a(E_\gamma)$ (for a representative Clover detector) upto E_γ $\sim$ 3 MeV is presented in Fig. 34. The average value (over all the detectors at 90°) of the fitting parameters are, a_0 = 1.003 $\pm$ 0.002 and a_1 = 1.0 $\pm$ 4.0 $\times 10^{-6}$ $(keV)^{-1}$. To obtain the value of the Δ_{Pol} the coincidence data is sorted into two asymmetric γ - γ matrices ,where the Y-axis contains the parallel (perpendicular) scattered events in detectors at 90°, with the corresponding coincidence events in all other detectors plotted along the X-axis. Gates are set on the X-axis and counts for a given peak of interest in the gated spectrum correspond to the parallel ($N_{||}$) and the perpendicular ($N_\perp$) scattering. It is apparent from the Fig. 35, that we are able to distinguish between electric and magnetic transitions thereform.

The energy dependent polarization sensitivity $Q(E_\gamma)(= \frac{\Delta_{Pol}}{P})$ helps us relate the

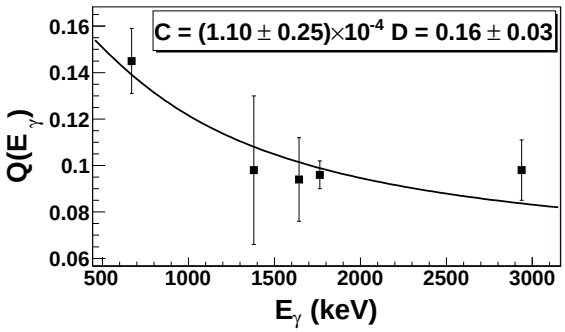

FIG. 36: Plot of polarization sensitivity as a function of γ-ray energy. The solid curve is obtained by fitting the data with Eq. (54).

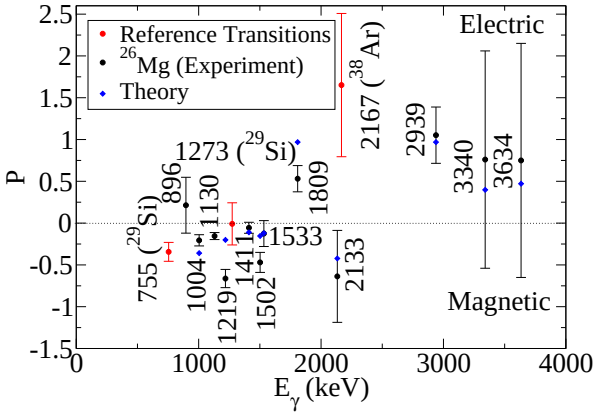

FIG. 37: Plot of the experimental and calculated polarization for γ-ray transitions observed in the present work.

measured linear polarization asymmetry Δ_{Pol} to the polarization P. The energy dependent polarization sensitivity for a similar setup (as used in the present experiment) upto 1.5 MeV was established by Palit and co-workers [71]. The observation of high energy transitions $E_\gamma \geq$ 2MeV, necessitated the extension of the sensitivity upto to this energy domain. This exercise was undertaken, and the results are shown in Fig. 36. It is to be noted that the polarization results using the present sensitivity parameters have been compared with the those using the parameters from Palit *et al.* [71] and have been found to be in satisfactory agreement in the common energy domain.

Using the above obtained value for the polarization sensitivity, the polarization values (P) are calculated and presented in Fig. 37. The figure also includes the polarization of known transitions from other nuclei, populated in the current investi-

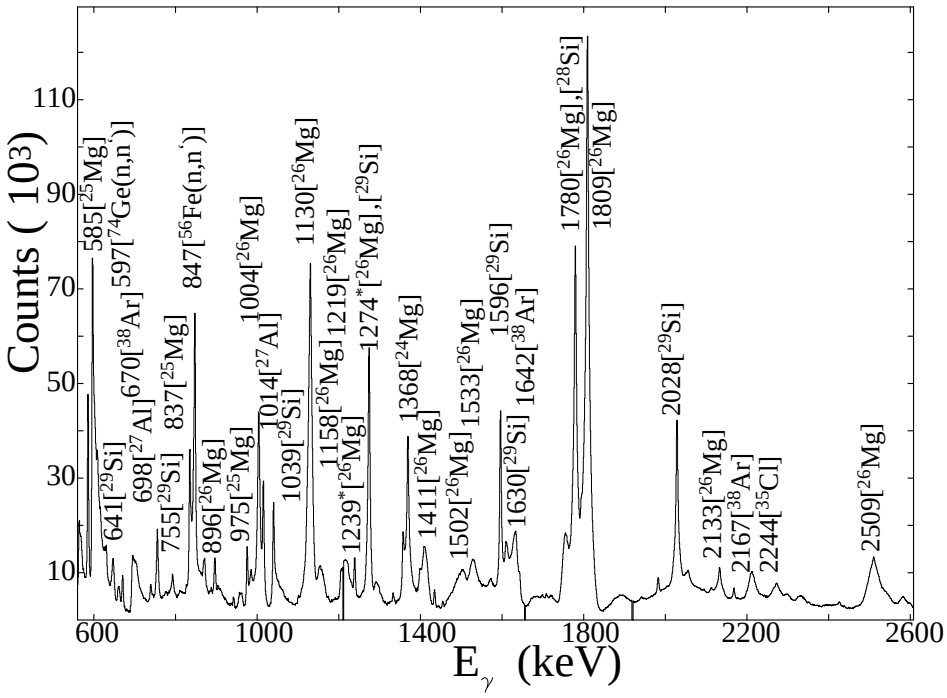

FIG. 38: Projection spectrum from the $\gamma - \gamma$ matrix, for the ^{13}C + ^{18}O reaction. Identifying the populated nuclei from their characteristics γ-transitions. The new transitions belonging to ^{26}Mg have been labeled with asterisk.

gation. The later are found to corroborate the previous assignments. The theoretical polarization has also been extracted for comparison with the experimental results (Fig. 37). The calculated values are in qualitative agreement with the experimental findings, as illustrated in Fig. 37. The procedure for extraction of both theoretical and experimental values of polarization have been presented in chapter 3.

5.4 Level Scheme of ^{26}Mg

The projection spectra (90^o) from the $E_\gamma - E_\gamma$ matrix is depicted in Fig. 38. From the characteristic de-exciting γ-ray transitions, (primarily originating from the decay of the first excited state to the ground state) the nuclei populated in the present experiment have been identified to include ^{24,25,26}Mg, ^{27}Al and ^{28,29}Si, which are commensurate with the predictions of the statistical model calculations. The γ-ray transitions attributed to nuclei such as ^{38}Ar and ^{35}Cl originate from the beam halo

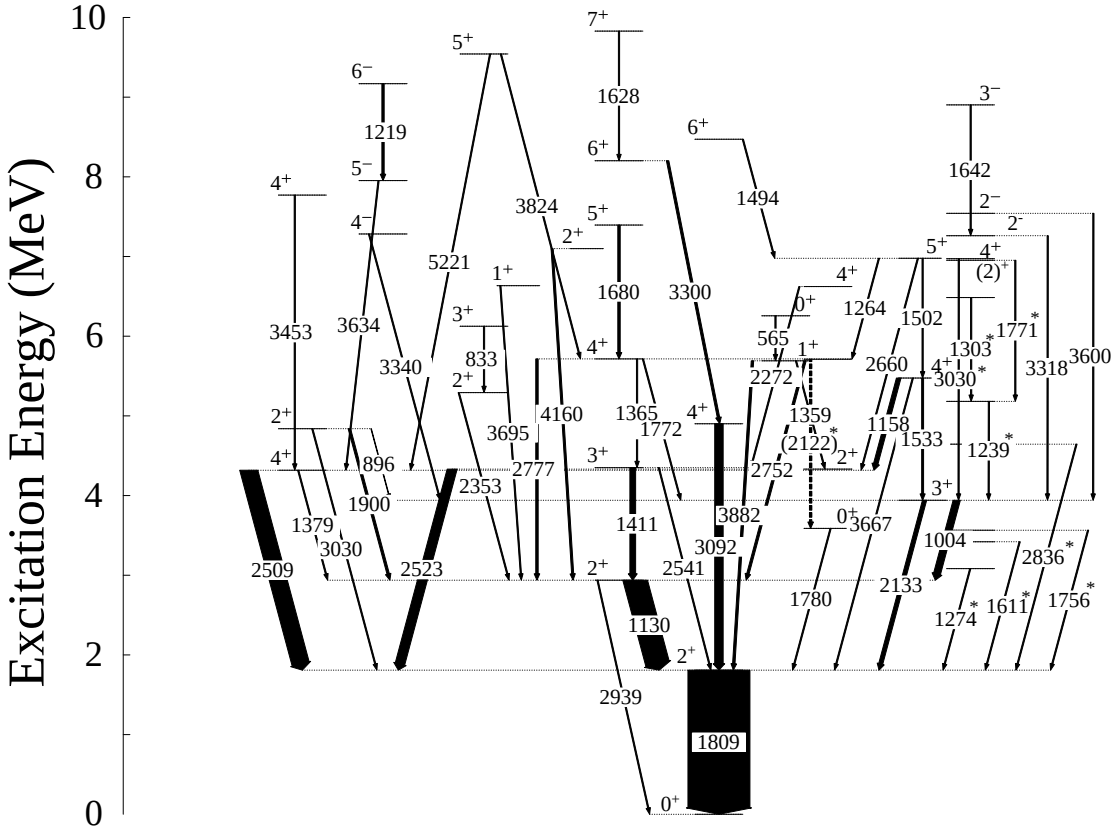

FIG. 39: Level scheme of ^{26}Mg nucleus from the present work. New transitions from the current measurements are labeled with *. The widths of the arrows are proportional to the γ-ray intensities.

of (^{13}C) interacting with the (^{27}Al) target holder. These lines have been used as additional reference points for $R_{anisotropy}$ and polarization measurements, as detailed in the preceding section.

The level scheme of the ^{26}Mg nucleus developed from the present endeavour is presented in Fig. 39 while Fig. 40 illustrates a partial gated spectrum, when the gate is set on the on the 1809 keV ($2_1^+ \rightarrow 0_1^+$), projected on the forward angles, 90^o and the backward angles. The stopping time for the recoiling ^{26}Mg nuclei in the Ta_2O_5 backing is typically of the order of few hundreds of fs, and hence, levels with $\tau_{level} \leq \tau_{stopp}$, would exhibit Doppler shape or shift. The angular spectra (Fig. 40) illustrates Doppler shapes and shifts for various transitions that may be used for extracting the level lifetimes. Several γ-transitions reported by the earlier workers have not been observed in the present experiment and thus have not been placed in the level scheme. For

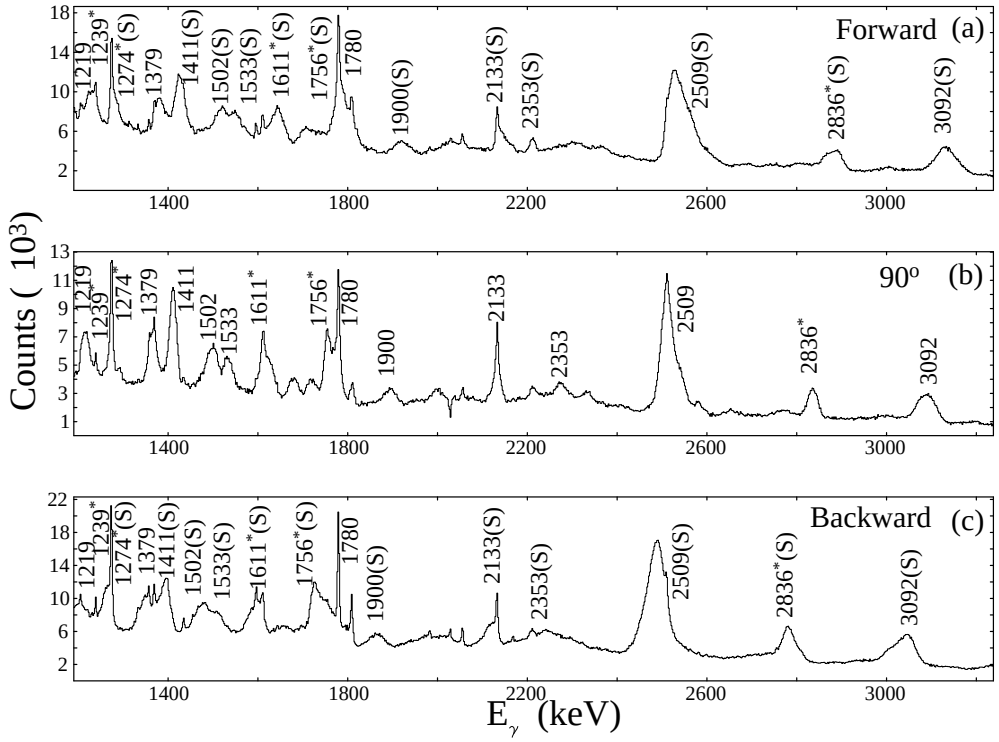

FIG. 40: Angle dependent coincidence spectra with gate set on the 1809 keV transition in ^{26}Mg, illustrating the observed Doppler shapes and shifts for different γ-ray transitions. Completely shifted transitions and the transitions with Doppler shapes are identified with the label "S"at the forward and backward angles. The new transitions have been labeled with an asterisk.

transitions with known multipolarity and electro-magnetic nature, whose $R_{anisotropy}$ and / or polarization could not be determined from the present experiment, the spin-parity assignments of the associated levels have been adopted from literature, as recorded in the NNDC database [23]. From the present efforts, around 8 new transitions belonging to ^{26}Mg have been identified, which have been been appropriately placed in the decay scheme from the observed coincidence relationship. The relative intensities of the transitions have been calculated after due incorporation of the efficiency of a Clover detector to an extended energy range upto $\sim$ 6 MeV, using data from Ref. [31, 32]. The results from the present work, in form of the excitation energies, the gamma-ray energies, $R_{anisotropy}$, polarization measurements and the subsequent assignments for the γ-ray transitions in ^{26}Mg nucleus, are summarized in Table III. The γ-transition energies $\leq$ 2 MeV have been quoted from fitting the corresponding peaks while higher energy transitions, that could not be appropriately fitted due to substantial Doppler

broadening, have been quoted with an uncertainty of 2 keV. The subsequent discussion is devoted to detail the observations and assignments and the development of the level scheme, which for convenience is categorized into negative and positive parity sequences.

5.4.A. Negative Parity Sequences

The negative parity states in these *sd* nuclei, originate due to the excitation of a single nucleon across the *sd-pf* shell gap, and hence are of importance, as the excitation energy of the first negative parity level is the indicator of the shell gap between *sd* and *pf* shells. From the previous studies for ^{26}Mg negative parity levels at 6878 ($J^\pi = 3^-$), 7062 ($J^\pi = 1^-$), 7261 ($J^\pi = (2,3)^-$), 7283 ($J^\pi = 4^-$), 7349 ($J^\pi = 3^-$), 7543 ($J^\pi = 2^-$), 7952 ($J^\pi = 5^-$) and 9169 ($J^\pi = 6^-$) (identified as 9171 keV in the present work), were established. The lowest negative parity level recorded was at 6878 keV that could not be confirmed in the current investigation, due to the broadening and contamination from the neighbouring channels. The 7062 ($J^\pi = 1^-$), and 7349 ($J^\pi = 3^-$) levels were previously reported Endt *et al.* [72] and were subsequently adopted by Glatz *et al.* [13]. These two negative parity levels have not been observed in the present experiment. The levels 7261 ($J^\pi = (2,3)^-$), 7283 ($J^\pi = 4^-$), 7543 ($J^\pi = 2^-$), 7952 ($J^\pi = 5^-$), 8903 ($J^\pi = 3^-$), 9171 keV ($J^\pi = 6^-$) were reported by Glatz *et al.* [13] and have been observed in the present measurements. The 7261 keV level was tentatively assigned $J^\pi = (2,3)^-$ of which the $J^\pi = 2^-$ assignment has been concluded in the present work from shell model calculations, discussed in the subsequent section. The 7283 keV level was reported to de-excite via 3340, 2963, 2932, 2381 and 1567 keV γ-transitions with branching ratio 50, 31, 9, 5 and 5%. The 3340 keV transition has been observed in the present work and included in the proposed level scheme while all other transitions have not been confirmed in the present work. The electro-magnetic character of the 3340 keV transition has been concluded as $E1$, from the measured value for $R_{anisotropy} = 1.09 \pm 0.01$ (when the gate is set on a quadrupole transition), and $P = 0.75 \pm 1.30$. This assignment is in conformity with the previous assignment, for this transition. The 7543 keV level was previously reported to be de-exciting by 3209, 4603, 3600, 3191 and 5732 keV transitions with branching ratio 37, 31, 14, 3, 15

TABLE III: Details of γ-ray transitions of the ^{26}Mg nucleus, observed in the present work.

$E_i(keV)$	$E_\gamma(keV)$	$E_f(keV)$	$I_\gamma(\%)$	J_i^π	J_f^π	$R_{anisotropy}$	P	Assignment
1809	1809.2 ± 1.0	0	259.3 ± 10.2	2_1^+	0_1^+	1.87 ± 0.04^D	0.53 ± 0.15	E2
2939	1130.4 ± 0.3	1809	100.0 ± 7.3	2_2^+	2_1^+	1.24 ± 0.01^Q	-0.15 ± 0.04	M1+E2
	2938.9 ± 1.0	0		2_2^+	0_1^+	2.20 ± 0.17^D	1.05 ± 0.33	E2
3083	1274.1 ± 2.0	1809			2_1^+			
3420	1611.4 ± 1.7	1809			2_1^+	1.08 ± 0.02^Q		D+Q
3565	1756.1 ± 1.9	1809			2_1^+			
3589	1779.6 ± 2.1	1809		0_2^+	2_1^+	2.19 ± 1.46^Q	1.74 ± 2.80	E2
3943	1004.1 ± 1.6	2939	29.3 ± 7.6	3_1^+	2_2^+	0.92 ± 0.16^Q	-0.20 ± 0.06	M1+E2
	2133.1 ± 1.0	1809	17.1 ± 2.7	3_1^+	2_1^+	1.11 ± 0.05^Q	-0.63 ± 0.55	M1(+E2)
4318	1379.2 ± 1.1	2939		4_1^+	2_2^+			
	2509.0 ± 2.0	1809	73.3 ± 20.6	4_1^+	2_1^+		1.2 ± 1.6	$(E2)^N$
4332	2523.0 ± 2.0	1809	40.4 ± 52.7	2_3^+	2_1^+		-0.57 ± 0.61	
4350	1411.4 ± 0.4	2939	24.0 ± 3.0	3_2^+	2_2^+	1.16 ± 0.03^Q	-0.05 ± 0.06	M1+E2
	2541.0 ± 2.0	1809		3_2^+	2_1^+		-0.34 ± 0.91	$M1+E2^N$
4645	2836.0 ± 1.3	1809			2_1^+	1.13 ± 0.07^Q		D+Q
4839	896.0 ± 1.3	3943	2.1 ± 2.2	2_4^+	3_1^+	1.01 ± 0.01^Q	0.21 ± 0.33	M1+E2
	1900.1 ± 2.0	2939	10.0 ± 2.7	2_4^+	2_2^+			$M1(+E2)^N$
	3030.0 ± 2.0	1809		2_4^+	2_1^+			
4901	3092.0 ± 2.0	1809	35.3 ± 3.4	4_2^+	2_1^+	1.74 ± 0.04^Q	0.17 ± 0.12	E2(+M3)
5182	1238.9 ± 0.7	3943			3_1^+			
5292	2353.0 ± 2.0	2939		2_5^+	2_2^+			
5476	1158.3 ± 1.2	4318	18.6 ± 3.2	4_3^+	4_1^+	1.42 ± 0.07^Q		$M1+E2^N$
	1533.4 ± 0.8	3943	8.0 ± 2.7	4_3^+	3_1^+	1.19 ± 0.83^Q	-0.12 ± 0.15	M1+E2
	3667.0 ± 2.0	1809		4_3^+	2_1^+			$(E2)^N$
5691	1359.4 ± 0.3	4332		1_1^+	2_3^+			
	2752.0 ± 2.0	2939		1_1^+	2_2^+			
	3882.0 ± 2.0	1809		1_1^+	2_1^+			
5711	2122.5 ± 0.8	3589			0_2^+			
5715	1365.0 ± 1.1	4350		4_4^+	3_2^+			$M1+E2^N$
	1772.0 ± 1.1	3943		4_4^+	3_1^+			$M1+E2^N$
	2777.0 ± 2.0	2939		4_4^+	2_2^+			$(E2)^N$
6125	833.1 ± 1.3	5292		3_3^+	2_5^+			

continued...

TABLEIII - continued...

$E_i(keV)$	$E_\gamma(keV)$	$E_f(keV)$	$I_\gamma(\%)$	J_i^π	J_f^π	$R_{anisotropy}$	P	Assignment
6256	565.1 ± 1.3	5691		0_4^+	1_1^+			D^N
6485	1302.7 ± 1.3	5182						
6622	2271.8 ± 1.0	4350		4_5^+	3_2^+			
6634	3695.0 ± 2.0	2939		1_2^+	2_2^+			
6953	1771.1 ± 1.4	5182		$(2)_7^+$				
6973	3030.0 ± 2.0	3943		4_6^+	3_1^+	0.95 ± 0.03^D		D+Q
6978	1263.7 ± 2.1	5715		5_1^+	4_4^+			
	1501.8 ± 1.0	5476		5_1^+	4_3^+	0.6 ± 0.8^Q	-0.47 ± 0.12	M1+E2
	2660.0 ± 2.0	4318		5_1^+	4_1^+			$M1+E2^N$
7099	4160.0 ± 2.0	2939	8.6 ± 2.5	2_8^+	2_2^+			
7261	3318.0 ± 2.0	3943		2_1^-	3_1^+			$(E1)^N$
7283	3340.0 ± 2.0	3943		4_1^-	3_1^+	1.09 ± 0.01^Q	0.75 ± 1.30	E1
7395	1680.0 ± 1.0	5715		5_2^+	4_4^+			$M1+E2^N$
7543	3600.0 ± 2.0	3943		2_2^-	3_1^+			$(E1)^N$
7771	3453.0 ± 2.0	4318		4_7^+	4_1^+			
7952	3634.0 ± 2.0	4318		5_1^-	4_1^+	1.19 ± 0.01^Q	0.75 ± 1.40	E1+M2
8201	3300.0 ± 2.0	4901		6_1^+	4_2^+			$E2(+M3)^N$
8472	1494.0 ± 1.4	6978		6_2^+	5_1^+			$M1+E2^N$
8903	1642.3 ± 0.7	7261		3_2^-	2_1^-			
9171	1218.7 ± 2.3	7952	9.5 ± 2.7	6_1^-	5_1^-		-0.66 ± 0.10	$M1+E2^N$
9539	3824.0 ± 2.0	5715		5_5^+	4_4^+			
	5221.0 ± 2.0	4318		5_5^+	4_1^+			$D+Q^N$
9829	1628.3 ± 1.2	8201		7_1^+	6_1^+			$M1(+E2)^N$

^{Q} From quadrupole gate. ^{D} From dipole gate. ^{N} Adopted from NNDC.

% respectively, of which only the 3600 keV transition has been confirmed in the present work and all other transitions are not confirmed. The 7952 keV (5^-) level was also reported by Glatz *et al.* [13] with the 3634 and 2238 keV transitions as the de-exciting transitions. However, in the present experiment, only the 3634 keV transition has been observed. The $R_{anisotropy}$ and polarization value of 1.19 ± 0.01 and 0.75 ± 1.40, respectively, indicate a dominant E1 character for the same, that is commensurate

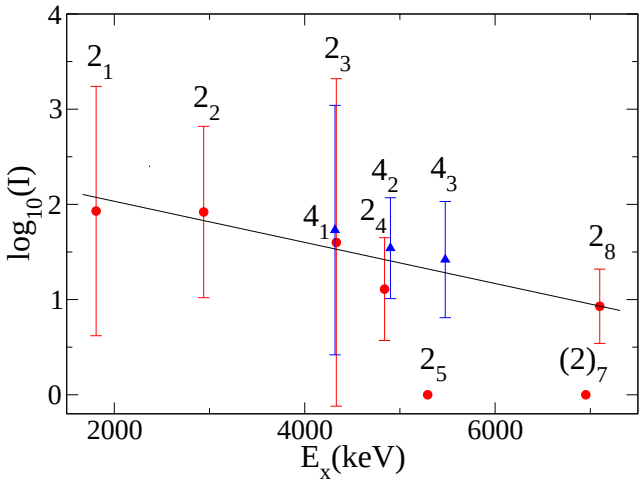

FIG. 41: Yield of the 2^+ and 4^+ states in ^{26}Mg, populated in the present experiment. The solid line represents the slope in the yield of the 2^+ states.

with the previous assignment. The 9171 (6^-) keV level, observed by Glatz *et al.* [13], was reported to be de-excited by 1216, 1774 and 1886 keV transitions. In the present work, only the 1216 keV, identified as 1219 keV, transition has been observed and included in the level scheme. The polarization asymmetry of the transition, determined in the present investigation, indicate it to be of magnetic character. The observation of 1774 keV transition could not be confirmed due to overlap from strong 1780 keV transition, both from ^{26}Mg as well as from ^{28}Si. The 1886 keV transition has also not been observed in the present experiment. Hence, the present study confirms most of the earlier reported negative parity states in ^{26}Mg.

5.4.B. Positive Parity Sequences

The advantage of heavy-ion fusion reactions, is it's preferential population of yrast and near yrast states. An intriguing finding in the present study, is the observation of several non-yrast states, especially for the 2^+, 4^+ and multiple $3, 5, 6^+$ levels. The present study reports the identification of 7 2^+ and 4^+ levels. As far as the 2^+ states are concerned Glatz *et al.* have reported upto five levels along with the corresponding shell model calculated energies. In addition they have also observed a 2^+ state at 7099

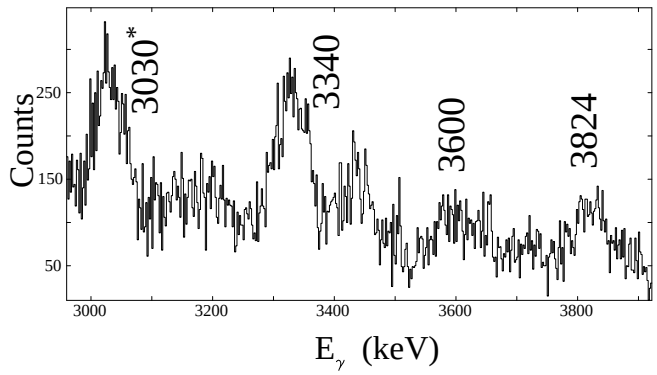

FIG. 42: Part of the gated spectrum on 1004 keV transition projected on 90^o. The high energy γ-ray transitions feeding the 3943 keV level have been labeled. The new transitions have been marked with *. The spectrum illustrates the observed Doppler broadening.

keV, but have not reported a corresponding state from the shell model calculations. In the present work, the first five 2^+ states have been found to comply with the results from Glatz *et al.*. However, the sixth 2^+ level at 6745 keV could not be confirmed in the present investigation. The level at 6953 keV has been tentatively assigned as the seventh 2^+ level. Further, the 2^+ level at 7099 keV has been well reproduced as the eighth 2^+ state in the shell model calculations, discussed in the subsequent section. It is worthy to mention that, the when the yields of the 2^+, 4^+ states, when corrected for the cascade feeding from corresponding the upper levels, it exhibits a general decreasing trend (Fig. 41) with increasing excitation energies. A plausible explanation for this feature could be attributed to the decreasing phase space.

The earlier workers have discussed in details the characteristics of the positive parity sequences [13, 73], since these sequences were identified as members of rotational bands, for example, Glatz *et al.* assigned these bands, to be based on $K^\pi = 0^+_1$, 0^+_2, 2^+_1, $(2)^+_2$, and 3^+ band-head. The following points summarizes the comparison between the present work and the findings of of Glatz *et al.* [13]

1. For the $K^\pi = 0^+_1$ ground state band, similar to the observation of Glatz and co-workers we also have observed, the 1809, 4901 and 8472 keV levels. The present anisotropy and polarization asymmetry measurements for the 1809 keV

transition, are indicative of an E2 character, which is in agreement with the previous assignments. The intraband E2 transition 3092 keV, deexciting the 4901 keV level, has also been observed in the present experiment. Based on the $R_{anisotropy}$ measurement for this transition a quadrupole multipolarity has been assigned to it. However, the 3571 keV (maximum branching reported in Ref. [23]) transition, de-exciting from the 8472 level, has not been observed in the current investigation. The spin-parity assignments of the 8472 keV level in this work have been adopted from previous measurements.

2. The difference between the present work and that of Glatz *et al.*, is substantial for the $K^{\pi} = 0_2^+$ [13]. This sequence according to Glatz comprised of 3589, 4332, 6622 and 9383 keV levels. Only the first three of these levels have been observed in this work. We could not confirm any of the intraband E2 transitions in the present measurements.

3. The $K^{\pi} = 3^+$ band was proposed to be consisting of 3941 (identified as 3943 in the current work), 5476, 6978 and 9112 keV levels, of which the first three have been observed in the present measurements along with the intraband transitions. The present anisotropy and polarization measurements, for the 1533 and 1502 keV transitions respectively deexciting the 5476 and 6978 keV levels, are suggestive of an M1/E2 in nature from the present work and is in agreement with the previous assignments.

4. The $K^{\pi} = 2_1^+$ band identified by Glatz *et al.* [13] comprises of 2939, 4350, 5715, 7395, 8201, 9829 and 12479 keV levels of which all, except 12479 keV, have been observed in the present experiment. However, only the 1411 keV intraband transition, deexciting the 4350 keV level, is observed with sufficient intensity which enabled us to undertake both the angular anisotropy and polarization measurements which resulted in it's assignment as a mixed M1/E2 transition, which is in agreement with the previous assignment. The 1365 and 1628 keV intraband transitions, respectively deexciting the 5715 and 9829 keV levels, though observed in this work, lacked sufficient statistics for any electro-magnetic or multipolarity assignment. Similar argument also holds for the 1680 keV transition de-exciting from 7395 keV level.

5. The 5292, 6125, 7677, 9542 keV levels were proposed as the members of the $K^{\pi} = 2_2^+$ band, of which the 5292 keV, 6125 keV and 9542 keV (identified as 9539 keV), have been observed in the present investigation. These levels are found to be deexciting by the 2353, 833 and 5221 keV transitions, respectively. The 9539 keV level also de-excites by the 3824 keV transition, observed in the present work, as illustrated in the 1004 keV gated spectrum in Fig. 42. These transitions were also known from the previous measurements.

The interband transitions, particularly those feeding the ground state band, are of significance. Similar to Glatz *et al.* [13], the 2523 keV transition from the 4332 keV level of 0_2^+ band, 3667 and 2133 keV transitions respectively from the 5475 and 3941 keV, modified to 5476 and 3943 keV in the present study, levels of 3^+ band and 1130 and 2541 keV transitions respectively from the 2939 and 4350 keV levels of 2_1^+ band, feeding the 1809 keV level of the ground state band, have all been observed in the present experiment. Some of the corresponding peaks have been shown in the 1809 keV gated spectrum in Fig. 40. The other interband transition strongly observed is 1004 keV, connecting the 3943 keV level of 3^+ band to the 2939 keV level of the 2_1^+ band. The multipolarity and polarization assignments could be made for most of these transitions, that are in agreement with the previous values, and are recorded in Table III.

The level at 4318 keV with $J^{\pi} = 4^+$ was reported by Glatz *et al.* [13] with exceptional characteristics that debarred it's assignment to any of the aforesaid rotational sequences. The level was interpreted to be of spherical origin. The state has been observed in the present experiment and found, similar to the previous observations, to be de-exciting by 1379 and 2509 keV transitions.

The state at 4839 keV ($J^{\pi} = 2^+$), reported as 4835 keV in the previous studies, has been observed in the present measurement. The 896, 1900, 3030 keV transitions, previously reported as 893, 1897 and 3026 keV, have also been identified de-exciting the level from the present work. The $R_{anisotropy}$ and polarization values for the 896 keV transition indicate it to be of $M1 + E2$ character. The 4839 keV transition, also reported to de-excite the level, has not been observed in the current experiment. A new level at 6973 keV, de-exciting by the 3030 keV transition, connecting to the 3943

keV level, has been identified in the present experiment. The corresponding peak is illustrated in Fig. 42, in the 1004 keV gated spectrum. The $R_{anisotropy}$ value for this 3030 keV transition implies a dominant dipole nature following which the 6973 state has been assigned as $J^{\pi} = 4^{+}$. This assignment is also supported by the shell model calculations, described in the subsequent section.

Certain levels have been observed for the first time in the present experiment but spin-parity assignments could not be made for the same owing to the sparse statistics of the de-exciting transitions (peaks). These are 3083 keV level de-exciting by 1274 keV transition, 3420 keV level de-exciting by 1611 keV transition, 3565 keV level de-exciting by 1756 keV transition, 4645 keV level de-populating by 2836 keV transition, 5182 keV level de-populating by 1239 keV transition, 6485 keV level de-populating by 1303 keV transition and 6953 keV level, de-exciting by 1771 keV transition respectively. However, from the shell model calculations, the 6953 keV level has been tentatively assigned $J^{\pi} = 2^{+}$.

The level structure of this nucleus, reported earlier, from light ion reactions has been re-visited. New transitions in this nucleus have been identified. The spin assignments have been carried out following a simultaneous analysis of the coincidence angular anisotropy as well as linear measurements.

5.5 Shell Model Calculations

5.5.A. Calculations for ^{26}Mg

The spherical shell model has been extensively used to describe the observed level structures in *sd* nuclei. However, due to then computational limitations these calculations could not be extended for the negative parity states, as these involve the occupation of the fp orbitals by a single nucleon, and this requires a larger model space, which encompasses the $sd - pf$ orbitals. Hence, the earlier calculations were centred around the interactions derived for the full $2s-1d$ shell comprising of $1d_{5/2}$, $2s_{1/2}$, $1d_{3/2}$ orbitals [13]. The USD interaction, developed by Brown and co-workers has achieved

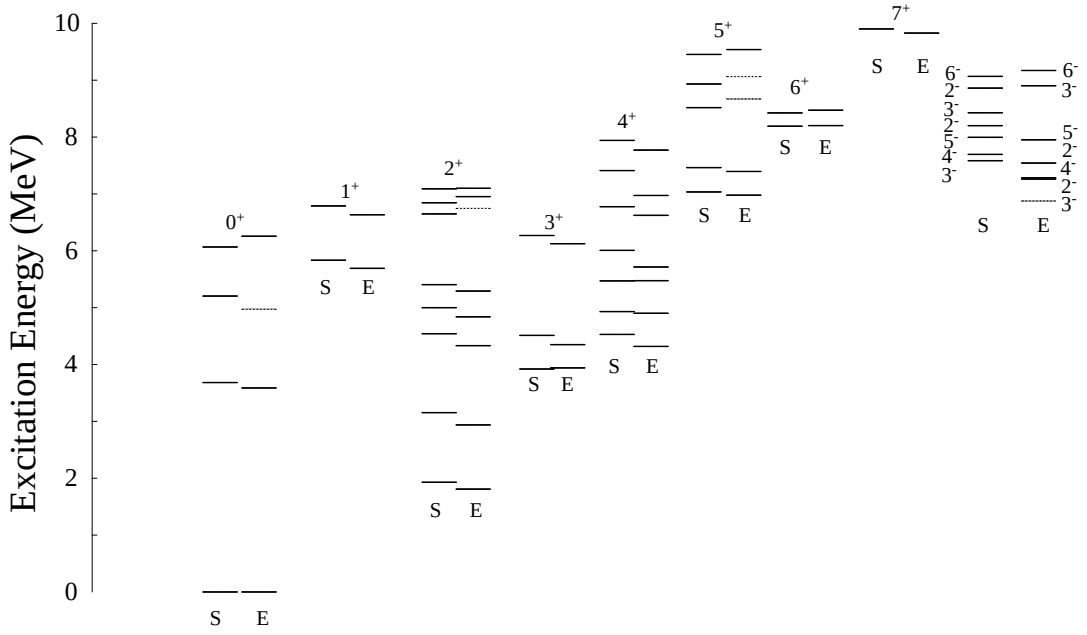

FIG. 43: Calculated levels (denoted by S) in ^{26}Mg shown alongside the experimental levels (denoted by E). Levels that are not observed in the present experiment, but were reported previously and adopted in the NNDC database, are shown in dotted lines. The positive-parity levels have been grouped according to their respective spins, indicated above each group, while the negative-parity levels are drawn in one group.

remarkable success in predicting the properties of the *sd* shell nuclei. Recently, this interaction was updated by obtaining the interaction parameters following a global fit to nearly 608 data points for the ground-state binding energies as well as the excited states (the original interaction was deduced from 66 experimental points). The updated interaction was codenamed USDA [61] in NuShellX @ MSU [57].

5.5.B. Positive Parity States

We have preformed the calculations for the positive states in ^{26}Mg using this interaction and the $1d_{5/2}$, $2s_{1/2}$, $1d_{3/2}$ orbitals. The predicted ground state energy is -105.498 MeV, which is in excellent compliance with the experimental value of -105.528 MeV. The experimental excitation energies are compared with the predictions of this interaction in Table IV. As is evident from the comparison, the values are in close conformity. Since we would like to extend these calculations to the negative parity states also, the

TABLE IV: Comparison of the experimentally observed and shell model predicted energy levels in ^{26}Mg from the present experiment and shell model calculations using $USDA$ and $sdpfmw$ interactions.

J_i^π	E^i_{expt} (keV)	$E^i_{SM}(USDA)$ (keV)	$E^i_{SM}(sdpfmw)$
2_1^+	1809	1938	1928
2_2^+	2939	3109	3153
0_2^+	3589	3664	3683
3_1^+	3943	3898	3921
4_1^+	4318	4402	4528
2_3^+	4332	4456	4542
3_2^+	4350	4374	4511
2_4^+	4839	4816	5000
4_2^+	4901	4908	4930
2_5^+	5292	5528	5404
4_3^+	5476	5492	5470
1_1^+	5691	5774	5833
4_4^+	5715	5897	6006
3_3^+	6125	6165	6268
0_4^+	6256	6106	6067
4_5^+	6622	6700	6776
1_2^+	6634	6568	6799
4_6^+	6973	7472	7410
5_1^+	6978	7058	7035
2_8^+	7099	7236	7090
5_2^+	7395	7445	7462
4_7^+	7771	7869	7940
6_1^+	8201	8119	8191
6_2^+	8472	8454	8424
5_5^+	9539	9408	9453
7_1^+	9829	9714	9902

model space has to be expanded to include the $1f_{7/2}$, $1f_{5/2}$, $2p_{3/2}$ and $2p_{1/2}$ orbitals. The two body matrix elements for such a large model space are usually derived from a combination of experimental and phenomenological interactions. One such interaction for the *sd-pf* model space, is codenamed *sdpfmw* [74] in NuShellX @ MSU [57], which adequately described the observed level structures in ^{34,32}P [9, 10]. The *sdpfmw* interaction is derived from a combination of USD interaction, the McGrony interaction and Millener-Kurath cross shell interaction. The USD interaction parameters consist of more than 60 two body matrix elements and three single particle energies relative to the ^{16}O core that were determined from a least square fit to $\sim$ 440 binding energies in A = 18 - 30 nuclei. The McGrory's interaction consists of 195 TBME and four SPE relative to ^{40}Ca core. The starting point of the interaction is the familiar effective interaction of Kuo and Brown. The least square fitting was carried out by McGrory for 29 binding energies in the A = 42 - 44 region with only eight $\langle f_{7/2}f_{7/2}|\, V\, |f_{7/2}f_{7/2}\rangle$ TBME as the variable parameters. The Millener Kurath particle hole interaction was developed to describe the non-normal parity states in the $A = 16$ region. A fairly good fit was obtained to the T = 0 and 1, $1p-1h$ states of ^{16}O with the parameters of this interaction.

However, unrestricted calculations are not computationally feasible in such a large model space. Hence, the model has to be internally truncated. Accordingly, the positive parity levels were generated by restricting the valence nucleons within the *sd* orbitals ($0\hbar\omega$ *i.e* no particles were allowed to be excited across the major shell). The predicted ground state energy using *sdpfmw* interaction is -105.531 MeV, which is in close agreement with the reported observations. The predicted excitation energies are compared with the experimental findings, in Tables IV and Fig. 43. As seen from the figure, no significant deviation is observed between the two. This exercise validates the truncation scheme as well as the two-body matrix elements used. The calculations were then extended to the negative parity states, wherein one nucleon was excited from the *sd* orbitals into the *fp* orbitals ($1\hbar\omega$ truncation).

Results of the shell model calculations for ^{26}Mg are summarized in the Tables V, VI, VII, VIII and pictorially illustrated in Fig. 43. As seen from the figure the excitation energies predicted by the model calculations reproduced reasonably their experimental counterparts. The particle occupancy are recorded in Table V. The * marked energy

level in Table V are taken from NNDC database [23]. The τ(Expt) values are taken from [23] are used in Table V and Table VI. The shell model wave function was used to deduce the level-lifetimes, from the calculated transition probabilities (Table VII) which was obtained using the values for effective charges as detailed in Ref. [75] ($g_{lp} = 1.175, g_{sp} = 5.000, g_{tp} = 0.260, g_{ln} = -0.106, g_{sn} = -3.500, g_{tn} = -0.170, e_p = 1.36, e_n = 0.45$). These results have been found to be in agreement with the previous results from Ref. [13].

TABLE V: Average particle occupancies (rounded-off to the second decimal) of positive-parity states in ^{26}Mg from shell model calculations along with the corresponding spectroscopic quadrupole moments and the level lifetimes.

J^π	E_{expt} (keV)	E_{SM} (keV)	Particles	$d_{5/2}$	$d_{3/2}$	$s_{1/2}$	τ(SM) psec	τ(Expt) psec	Q e^{2}fm^2
0_1^+	0	0	p	3.19	0.45	0.35	stable	stable	
			n	4.81	0.62	0.55			
2_1^+	1809	1928	p	3.15	0.43	0.41	0.353	0.687 ± 0.017	-14.13
			n	4.70	0.64	0.65			
2_2^+	2939	3153	p	2.98	0.42	0.58	0.165	0.203 ± 0.011	14.58
			n	4.37	0.60	1.02			
0_2^+	3589	3683	p	3.21	0.36	0.42	46.601	9.292 ± 0.202	0.00
			n	3.83	1.37	0.79			
3_1^+	3943	3921	p	3.20	0.39	0.39	3.444	1.226 ± 0.173	26.13
			n	4.45	0.89	0.64			
4_1^+	4318	4528	p	3.40	0.29	0.29	0.211	0.392 ± 0.023	2.93
			n	4.84	0.60	0.55			
2_3^+	4332	4542	p	3.19	0.36	0.44	0.104	0.028 ± 0.040	-15.62
			n	3.83	1.33	0.82			
3_2^+	4350	4511	p	2.99	0.48	0.52	0.111	0.152 ± 0.028	-0.19
			n	4.36	0.62	1.00			
2_4^+	4839	5000	p	3.08	0.37	0.54	0.090	0.040 ± 0.008	6.04
			n	4.38	0.79	0.81			
4_2^+	4901	4930	p	3.04	0.47	0.47	0.049	0.042 ± 0.009	0.69
			n	4.53	0.85	0.61			

continued...

TABLEV – continued...

J^π	E_{expt} (keV)	E_{SM} (keV)	Particles	$d_{5/2}$	$d_{3/2}$	$s_{1/2}$	τ(SM) psec	τ(Expt) psec	Q e^2fm^2
0_3^+	4972*	5203	p	2.67	0.31	1.00	0.499	0.635 ± 0.086	0.00
			n	4.17	0.78	1.03			
2_5^+	5292	5404	p	3.17	0.43	0.39	0.013	<0.014	18.12
			n	4.48	1.05	0.46			
4_3^+	5476	5470	p	3.00	0.38	0.61	0.039	0.030 ± 0.009	9.52
			n	4.30	0.77	0.91			
1_1^+	5691	5833	p	3.01	0.30	0.67	0.004	<0.011	-0.49
			n	4.32	0.74	0.92			
4_4^+	5715	6006	p	2.81	0.43	0.75	0.055	0.101 ± 0.050	-14.80
			n	4.33	0.71	0.95			
3_3^+	6125	6268	p	3.13	0.42	0.44	0.006	0.020 ± 0.009	4.14
			n	4.46	0.89	0.63			
0_4^+	6256	6067	p	3.12	0.63	0.23	0.106	0.075 ± 0.034	0.00
			n	3.91	0.76	1.32			
4_5^+	6622	6776	p	3.05	0.36	0.57	0.038	0.027 ± 0.007	-22.39
			n	3.82	1.34	0.82			
1_2^+	6634	6799	p	2.99	0.49	0.51	0.005	<0.010	4.43
			n	3.88	1.16	0.95			
2_6^+	6745*	6649	p	2.95	0.42	0.62	0.004	0.023 ± 0.011	-1.14
			n	3.96	0.99	1.03			
$(2)_7^+$	6953	6845	p	2.96	0.46	0.56	0.004		-7.12
			n	4.09	0.74	1.16			
4_6^+	6973	7410	p	2.91	0.59	0.49	0.005		25.05
			n	4.16	0.89	0.93			
5_1^+	6978	7035	p	3.11	0.38	0.50	0.029	0.020 ± 0.007	-4.29
			n	4.35	1.00	0.64			
2_8^+	7099	7090	p	2.89	0.59	0.51	0.006	<0.020	13.17
			n	4.49	0.79	0.70			
5_2^+	7395	7462	p	2.86	0.45	0.67	0.016	<0.020	-4.17
			n	4.31	0.61	1.07			
4_7^+	7771	7940	p	3.02	0.46	0.51	0.004	<0.010	-5.62
			n	4.24	1.02	0.72			
6_1^+	8201	8191	p	3.21	0.50	0.28	0.021	<0.020	-0.91

continued...

TABLEV – continued...

J^π	E_{expt} (keV)	E_{SM} (keV)	Particles	$d_{5/2}$	$d_{3/2}$	$s_{1/2}$	τ(SM) psec	τ(Expt) psec	Q e^2fm^2
			n	4.51	0.75	0.72			
6_2^+	8472	8424	p	3.27	0.27	0.44	0.030	<0.020	17.87
			n	4.39	0.70	0.89			
5_3^+	8670*	8518	p	2.74	0.54	0.71	0.003	<0.010	7.37
			n	4.27	0.77	0.95			
5_4^+	9064*	8933	p	2.94	0.58	0.47	0.002	<0.010	7.93
			n	4.35	0.78	0.85			
5_5^+	9539	9453	p	2.65	0.65	0.69	0.007	<0.020	28.94
			n	4.38	0.89	0.71			
7_1^+	9829	9902	p	3.50	0.21	0.28	0.069	0.053 ± 0.014	25.92
			n	4.56	0.60	0.82			

The detail of the spectroscopic and intrinsic quadrupole moment in context of shape evolution is discussed in chapter 6. The spectroscopic quadrupole (Q) moment as derived from the model calculations help us infer the shape of the nucleus in a given state. The ground state band, comprising of 0_1^+, 2_1^+, 4_2^+, 6_2^+ levels according to Glatz *et al.* [13] undergoes a shape evolution from prolate at low spins to vanishing quadrupole moment at 4_2^+ to oblate at higher spins. This corroborates with the spectroscopic quadrupole moments from the present shell model calculations, as illustrated in Table V. However, the calculations (present and the earlier) do not agree with the recent predictions of Hinohara *et al.* [65] who have reported their calculations for the ^{26}Mg nucleus based on the CHFB+LQRPA method. For example, the model calculations of Hinohara *et al.* are indicative of an oblate (potential) minimum for the ground state which is in sharp contrast to the prolate shape, predicted by the the shell model. Further, since Hinohara *et al.* have limited their discussions to the low lying deformed states in ^{26}Mg, detailed comparison with their results is not possible. Nevertheless, these two models are in qualitative unison regarding the γ-soft nature of the nucleus in the ground state and the subsequent shape evolution.

The band based on the $K^\pi = 0_2^+$ was as assigned a prolate deformation by Glatz

TABLE VI: Average particle occupancies (rounded-off to the second decimal) of negative-parity states in ^{26}Mg from shell model calculations along with the corresponding level lifetimes.

J^π	E_{expt} (keV)	E_{SM} (keV)	Particles	$d_{5/2}$	$d_{3/2}$	$s_{1/2}$	$f_{7/2}$	$f_{5/2}$	$p_{3/2}$	$p_{1/2}$	τ(SM) psec	τ(Expt) psec
3_1^-	6876*	7585	p	2.95	0.57	0.42	0.02	0.01	0.01	0.00		0.123(50)
			n	3.95	0.55	0.53	0.75	0.04	0.14	0.01		
2_1^-	7261	8209	p	2.91	0.55	0.49	0.01	0.01	0.01	0.00		< 0.010
			n	3.91	0.55	0.55	0.65	0.04	0.25	0.01		
4_1^-	7283	7695	p	2.97	0.59	0.41	0.02	0.01	0.00	0.00		0.034(11)
			n	4.05	0.53	0.44	0.78	0.02	0.15	0.00		
2_2^-	7543	8861	p	2.94	0.51	0.51	0.01	0.00	0.01	0.00		<0.010
			n	3.46	0.78	0.77	0.58	0.02	0.31	0.04		
5_1^-	7952	7995	p	2.95	0.57	0.43	0.02	0.01	0.00	0.00		0.020(9)
			n	4.04	0.52	0.46	0.84	0.02	0.09	0.00		
3_2^-	8903	8428	p	2.96	0.49	0.48	0.02	0.01	0.01	0.00		
			n	3.61	0.74	0.69	0.63	0.02	0.25	0.01		
6_1^-	9171	9067	p	2.94	0.55	0.47	0.02	0.01	0.00	0.00	0.332	0.037(11)
			n	4.03	0.52	0.47	0.88	0.02	0.06	0.00		

* From Ref. [23].

et al.. The Q values of the band members, 0_2^+, 2_3^+ and 4_5^+ (Table V), corroborate this assignment. The sign of quadrupole moment does not change for these members, an observation similar to that of Glatz *et al.*. As far as the $K^\pi = 3^+$ band is concerned, Glatz *et al.* assigned the levels 3_1^+, 4_3^+, 5_1^+, 6_3^+ to the band and proposed Coriolis mixing with the $K^\pi = 2_1^+$ band. Present shell model calculations reflect, an evolution from oblate to prolate deformation in the $K^\pi = 3^+$ band, at J$^\pi = 5_1^+$. The $K^\pi = 2_1^+$ band, assigned to be comprised of 2_2^+, 3_2^+, 4_4^+, 5_2^+, 6_1^+, 7_1^+ levels was identified to exhibit irregular behaviour by Glatz *et al.* which complies with the results of the present calculations.

TABLE VII: Transition probabilities in ^{26}Mg from the present shell model calculations.

J_i^π	E^i_{expt} (keV)	E^i_{SM} (keV)	J_f^π	E^f_{expt} (keV)	E^f_{SM} (keV)	B(M1) $\mu_N^2\times10^{-3}$	B(E2) e^2fm^4	B(M1)(Expt)** $\mu_N^2\times10^{-3}$	B(E2)(Expt) ** e^2fm^4
2_1^+	1809	1928	0_1^+	0	0.00	0.00	86.36		$62.61\pm^{4.11}_{3.65}$
2_2^+	2939	3153	2_1^+	1809	1928	137.90	53.07	$170.05\pm^{13.42}_{11.99}$	$27.42\pm^{12.33}_{9.59}$
2_2^+	2939	3153	0_1^+	0	0.00	0.00	3.65		1.78±0.27
0_2^+	3589	3683	2_1^+	1809	1928	0.00	1.05		4.57±0.27
3_1^+	3943	3921	2_2^+	2939	3153	19.43	0.15	$36.69\pm^{7.16}_{5.37}$	<4.11
3_1^+	3943	3921	2_1^+	1809	1928	0.96	0.02	$1.79\pm^{0.46}_{0.35}$	$5.94\pm^{1.37}_{0.91}$
4_1^+	4318	4528	2_2^+	2939	3153	0.00	7.54		
4_1^+	4318	4528	2_1^+	1809	1928	0.00	31.92		20.56±1.14
2_3^+	4332	4542	2_1^+	1809	1928	25.82	3.17	$102.03\pm^{21.48}_{16.11}$	
3_2^+	4350	4511	2_2^+	2939	3153	41.10	143.50	$62.65\pm^{23.27}_{14.32}$	$42.04\pm^{36.10}_{20.65}$
3_2^+	4350	4511	2_1^+	1809	1928	18.21	5.72	$10.74\pm^{3.58}_{2.68}$	$0.22\pm^{0.36}_{0.18}$
2_4^+	4839	5000	3_1^+	3943	3921	0.45	0.36		
2_4^+	4839	5000	2_2^+	2939	3153	34.25	1.04	$202.27\pm^{35.80}_{28.64}$	
2_4^+	4839	5000	2_1^+	1809	1928	0.70	4.79	$2.14\pm^{0.89}_{0.71}$	
4_2^+	4901	4930	2_1^+	1809	1928	0.00	62.36		$77.69\pm^{25.13}_{15.53}$
2_5^+	5292	5404	2_2^+	2939	3153	264.50	0.28		
4_3^+	5476	5470	4_1^+	4318	4528	383.60	10.25	$733.90\pm^{393.80}_{196.90}$	$64.89\pm^{242.21}_{62.15}$
4_3^+	5476	5470	3_1^+	3943	3921	110.80	89.18	$150.36\pm^{89.50}_{46.54}$	$66.26\pm^{68.55}_{31.99}$
4_3^+	5476	5470	2_1^+	1809	1928	0.00	14.85		$5.48\pm^{4.11}_{2.28}$
1_1^+	5691	5833	2_3^+	4332	4542	21.59	12.93		
1_1^+	5691	5833	2_2^+	2939	3153	231.10	3.59		
1_1^+	5691	5833	2_1^+	1809	1928	103.00	4.30		
4_4^+	5715	6006	3_2^+	4350	4511	56.34	40.28	$168.26\pm^{179.00}_{64.44}$	$37.01\pm^{67.63}_{21.02}$
4_4^+	5715	6006	3_1^+	3943	3921	0.56	1.71	$78.76\pm^{84.13}_{28.64}$	$5.02\pm^{13.25}_{3.65}$
4_4^+	5715	6006	2_2^+	2939	3153	0.00	7.46		$23.76\pm^{27.87}_{9.59}$
3_3^+	6125	6268	2_5^+	5292	5404	274.80	114.30		
0_4^+	6256	6067	1_1^+	5691	5833	98.16	0.00		
4_5^+	6622	6776	3_2^+	4350	4511	17.98	0.54	$35.79\pm^{19.69}_{12.53}$	
1_2^+	6634	6799	2_2^+	2939	3153	168.00	0.73		
4_6^+	6973	7410	3_1^+	3943	3921	101.00	0.22		
5_1^+	6978	7035	4_4^+	5715	6006	9.65	1.83	$50.12\pm^{48.33}_{23.27}$	
5_1^+	6978	7035	4_3^+	5476	5470	134.00	65.88	$393.80\pm^{268.50}_{125.30}$	$109.68\pm^{223.93}_{41.13}$
5_1^+	6978	7035	4_1^+	4318	4528	6.33	12.79	$6.80\pm^{6.08}_{2.86}$	$6.85\pm^{19.65}_{5.02}$

continued...

TABLEVII - continued...

J_i^π	E^i_{expt} (keV)	E^i_{SM} (keV)	J_f^π	E^f_{expt} (keV)	E^f_{SM} (keV)	B(M1) $\mu_N^2\times10^{-3}$	B(E2) e^2fm^4	B(M1)(Expt)** $\mu_N^2\times10^{-3}$	B(E2)(Expt)** e^2fm^4
2_8^+	7099	7090	2_2^+	2939	3153	11.71	0.45		
5_2^+	7395	7462	4_4^+	5715	6006	396.30	21.93	>264.92	>16.45
4_7^+	7771	7940	4_1^+	4318	4528	45.91	2.29		
6_1^+	8201	8191	4_2^+	4901	4930	0.00	52.60		
6_2^+	8472	8424	5_1^+	6978	7035	27.94	14.56	>161.10	> 28.33
5_5^+	9539	9453	4_1^+	4318	4528	0.87	0.07		
7_1^+	9829	9902	6_1^+	8201	8191	127.10	0.82	$213.01\pm^{80.55}_{46.54}$	

** From Ref. [13].

5.5.C. Negative Parity States

The negative parity states in these nuclei would be generated following the excitation of odd number of nucleons in to the *fp* shell. The shell model calculations for the neighbouring P nuclei, ^{32,34}P [9, 10]. have established that the excitation of a single nucleon into the *fp* shell could explain the observed negative parity levels. Accordingly, the calculations for the negative-parity states in Mg isotopes have been carried out by considering the excitation of a single nucleon from the *sd* to the *fp* orbitals ($1\hbar\omega$). The results for the ^{26}Mg nucleus are presented in Fig. 43. The calculated level energies are in satisfactory agreement with the experimental value. Particularly for $J^\pi = 5^-, 6^-$, the agreement is at the level of $\sim$ 40-100 keV while for lower spins $J^\pi = 3^-, 4^-$, it is $\sim$ 400-700 keV. The shell model predictions helped us resolve the ambiguity regarding the $J^\pi = (2,3)^-$ tentative assignment for the level at 7261 keV. The predicted energy for the $J^\pi = 2^-$ level is in better agreement with the experimental value ($E_{expt} - E_{theo} \sim$ 900 keV) than the calculated energy for $J^\pi = 3^-$, which is far more discrepant. Thus, the level has been assigned a spin-parity of $J^\pi = 2^-$. The particle occupancy for the negative-parity states, is suggestive of the domination of a single neutron into the $f_{7/2}$ orbital, with minor contribution from occupation of the $p_{3/2}$ orbital. It is understood that, in principle, the negative-parity states could also be generated due to configurations such as $(p)^{-n}, (sd)^{+n}$, which originate due to excitations across the ^{16}O

TABLE VIII: Transition probabilities in ^{26}Mg from the present shell model calculations.

J_i^π	E^i_{expt} (keV)	E^i_{SM} (keV)	J_f^π	E^f_{expt} (keV)	E^f_{SM} (keV)	B(M1) μ_N^2	B(E1)/B(E2) e^2fm^2/e^2fm^4
2_1^-	7261	8209	3_1^+	3943	3921	0.00	0.83×10^{-4}
4_1^-	7283	7695	3_1^+	3943	3921	0.00	0.46×10^{-3}
2_2^-	7543	8861	3_1^+	3943	3921	0.00	0.63×10^{-7}
5_1^-	7952	7995	4_1^+	4318	4528	0.00	0.95×10^{-3}
3_2^-	8903	8428	2_1^-	7261	8201	0.03	5.51
6_1^-	9171	9067	5_1^-	7952	7995	0.13	124.10

core. Such configurations could not be simultaneously considered with the excitations from *sd* to *fp* shells, within the present calculations. Nevertheless, reasonable agreement in the level energies have been obtained with *sd* to *fp* excitations, not only in the ^{26}Mg nucleus but in the neighbouring isotopes, as shall be discussed in the next section. It can thus be stated that the observed level structure of ^{26}Mg can be adequately described by $0\hbar\omega$ (positive-parity) and $1\hbar\omega$ (negative-parity) configuration beyond the oxygen core.

5.5.D. Systematics for Mg Isotopes

The success of the shell model calculations for ^{26}Mg nucleus, motivated us to extend these large basis shell model calculations to the neighbouring Mg isotopes. Besides trying to understand the systematics in the mass region, the main impetus was the absence of previous shell model study for the negative parity states in this nuclei. The results are illustrated in Fig. 44 and Fig. 45, individually for the even-A (^{24,26,28}Mg) and the odd-A (^{25,27,29}Mg) Mg isotopes. The experimental energies for Mg isotopes, other than ^{26}Mg, have been adopted from NNDC database [23]. The positive-parity states have been calculated including $0\hbar\omega$ excitations (*sd* configurations) and the results, for $^{24-29}$Mg, are in satisfactory agreement with the experimental observations, as illustrated in Fig. 44 and Fig. 45.

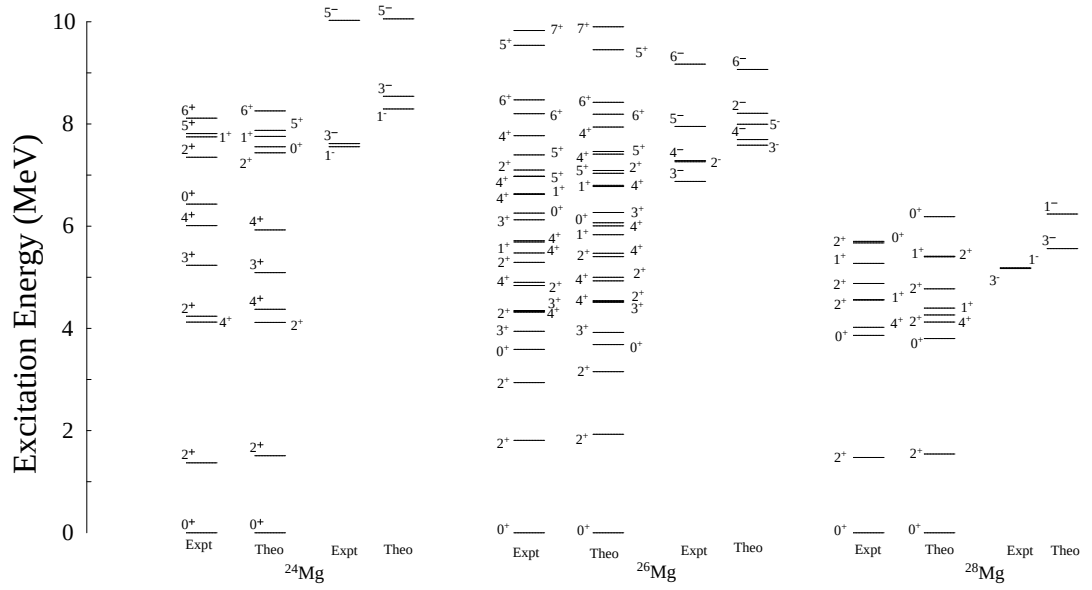

FIG. 44: Comparison of the experimental energy levels (Expt) in even-A Mg isotopes with the shell model calculations (Theo), carried out in the present work. The data for ^{24,28}Mg are taken from the NNDC database.

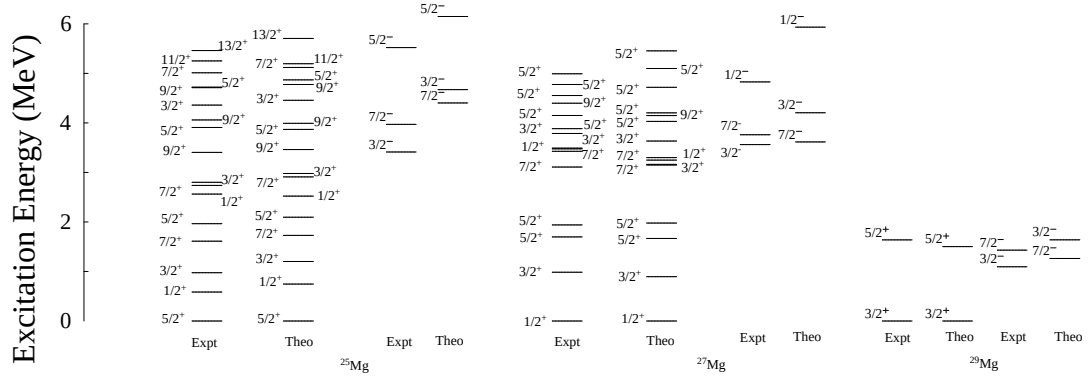

FIG. 45: Comparison of the experimental energy levels (Expt) in odd-A Mg isotopes with the shell model calculations (Theo), carried out in the present work. The data are taken from the NNDC database.

The negative-parity states in ^{25,27,29}Mg have been calculated including $1\hbar\omega$ excitations. For ^{25}Mg, the agreement with the experimental level energies varies from ~ 400 keV for $J^\pi = 7/2^-$ to ~ 1.2 MeV for $J^\pi = 3/2^-$. In ^{27}Mg, the tentative spin-parity assignments of $J^\pi = 5/2^-, 7/2^-$ on the 3.761 MeV level and $J^\pi = 1/2^-, 3/2^-$ on the 4.828 level, could be resolved from the present calculations. In case of the former,

the shell model calculations with $J^\pi = 7/2^-$ produced an agreement within $\sim$ 150 keV of the experimental value while the predicted energy for $J^\pi = 5/2^-$ is 5.649 MeV, largely discrepant with respect to the experimental level energy, thus favoring the $7/2^-$ assignment to the 3.761 MeV level. For the 4.828 level, calculations with $J^\pi = 1/2^-$, produced an agreement of $\sim$ 1.106 MeV while that with $J^\pi = 3/2^-$ was substantially different from the experimental level energy, thus supporting an $1/2^-$ assignment. Similarly, in case of ^{29}Mg, the present calculations aided in resolving the the tentative spin-parity assignments of $J^\pi = 1/2^-, 3/2^-$ on the 1.095 MeV level and $J^\pi = 5/2^-, 7/2^-$ on the 1.431 level. For the 1.095 keV level, calculations with $J^\pi = 3/2^-$ produced an agreement of $\sim$ 500 keV with the experimental level energy while that for the 1.431 MeV state, with $J^\pi = 7/2^-$, was $\sim$ 150 keV. Calculations with alternative spin-parities have also been carried out and found to result in substantially discrepant level energies with respect to the experimental results.

The negative-parity states in ^{28}Mg have been calculated including $1\hbar\omega$ excitations. The resulting energies have shown agreement with the experimental energies within $\sim$ 400 keV for $J^\pi = 3^-$ and $\sim$ 1 MeV for $J^\pi = 1^-$. For the ^{24}Mg nucleus $J^\pi = 5^-$ level have been well reproduced by $1\hbar\omega$ excitation resulting in an agreement of $\sim$ 30 keV, with the experimental level energy. However, for $J^\pi = 1^-$ and 3^- levels of the nucleus $3\hbar\omega$ excitations were necessitated for agreement ($\sim$ 700-900 keV) with the experimental energy.

It appears that the positive-parity states in the $^{24-28}$Mg isotopes have been well reproduced within pure *sd* configurations whereas the negative-parity states are dominated by one neutron excitation to the *fp* shell. The calculations were performed without any alteration in the single particle energy. However, the discrepancy of $\sim$ 1 MeV with respect to the experimental data, particularly for the low lying negative-parity states, might indicate the limitation of the Hamiltonian and omissions of important excitations from *p* to *sd* orbitals that could not be considered in the present calculations.

The nucleus ^{26}Mg was populated following heavy-ion fusion reaction. The de-exciting γ-rays were detected using an array of Clover detectors. New transitions have been observed and placed in the level scheme. The use of Clover detectors facilitated linear

polarization measurements, which helped us assign the electro-magnetic nature to the transition, whose multipolarity was deduced from observed angular intensity anisotropy.

The developed level scheme was successfully interpreted using large basis shell model calculations. The calculation indicated the dominance of nucleon excitation with in the sd shell, on the positive parity sequences. The negative parity states are dominated by the excitation of single nucleon from sd orbital to the fp orbital.

The systematics for the negative parity sequence indicate a decrease in the excitation energy of the lowest negative parity level, which encodes the information on the $sd - pf$ shell gap. This may plausibly indicate a preference of many body correlations in reducing the extreme single particle shell gap and stabilizing deformed structure at lower energies than their experimental counterpart.

Chapter - 6

Spectroscopic Study of Si Isotopes

This chapter details the first high resolution in-beam gamma-ray spectroscopic investigation of ^{29}Si nucleus, populated in a conventional heavy-ion induced fusion-evaporation reaction. High spin states of the nucleus have been populated using ^{18}O(^{13}C,2n) and ^{18}O(^{16}O,αn) reactions at E_{lab} = 30 and 34 MeV. The level scheme was developed using the conventional analysis procedure. Large basis shell model calculations have been carried out for positive and negative parity states for ^{29}Si using updated interactions and the results corroborate the experimental findings. The calculations have also been undertaken for the neighbouring ^{28,30}Si isotopes. The shell model calculations have been performed without any adhoc tweaking of the single particle energies, a practice routinely followed in this mass region. The deformation characteristics were also successfully interpreted within the framework of the shell model for the Si isotopes.

6.1 Introduction

The *sdpf* nuclei, with $Z \sim$ 12-16 and $N \sim$ 14-18, have been subjects of recent spectroscopic investigations, carried out using contemporary facilities [8–10, 76]. The primary motivation has been to probe the evolving structure of these nuclei belonging to the transitional region, between the line of stability and the island of inversion [77, 78]. Interestingly, the *sd* shell nucleus, ^{29}Si occupies an important region in the nuclear landscape, where the nuclear deformation is changing from prolate to oblate [79, 80]. A large number of nucleons in the *sd* shell and a preferential occupation of the fp-shell configurations even at lower excitation energies are expected to favour the stabilization of deformed structures in these mid-shell nuclei. The observed energy levels are indeed a combination of both single particle as well as collective excitations. The associated theoretical studies have also been zealously pursued in conjunction with the experimental endeavours. The calculations were performed within the framework of

diverse models such as the single particle model, the collective model and the recently developed Antisymmetrized Molecular Dynamics (AMD) model, which were equally successful in interpreting the level structures. The large basis shell model calculations in this region focused on interpreting the lowest negative parity level, which reveal the energy gap between the *sd* and *pf* orbitals. However, these calculations have been performed with a nucleus specific adhoc adjustment in the single particle energies [81], while calculations with updated interactions [75] and reasonable configuration space have indicated such modifications to be inessential [7].

Most of the previous studies on the level structure of these nuclei were performed using light-ion induced reactions and they used modest detector setups as their detection system. As a consequence, for example, the level lifetimes and the γ-ray angular distributions, exhibit substantial scatter and some of them have large uncertainties even at low excitation energies and spins. The ambiguities and/or uncertainties in the experimental findings can be found, for example, in the ^{29}Si nucleus, being probed in the present study, as illustrated in Fig. 46. The lifetime of the 1274 keV ($J^{\pi} = 3/2^{+}$) (a transition de-exciting the first excited state to the ground state) level has been reported in several previous studies [14–22] but the values are considerably variant, with a few of them having substantial uncertainties. Similarly, the multipolarity and the mixing ration (δ) of the 1596 keV transition in the same nucleus, de-exciting the lowest negative parity state (3624 keV, $J^{\pi} = 7/2^{-}$), has been investigated in a previous study [24] carried out with a NaI(Tl) scintillator detector, with the concomitant large uncertainties on the angular distribution coefficients (Fig. 46), as a consequence of it ,their mixing ratio assignment has large uncertainty. As we discussed in earlier chapter of the present thesis the lowest negative parity level is very crucial in this region, as it originates from the cross-shell excitation of a nucleon across the $sd - pf$ major shell gap and hence warrants detailed and unambigious measurements. From the previous measurements due to associated uncertainties and or scatter in the reported values, we are not able to arrive at unambiguous experimental pointers, such as level lifetime, branching ratio, multipolarity, electro-magnetic nature, mixing ratio, pertinent for benchmarking model calculations.

In the present work the level structure of ^{29}Si was investigated, in two separate

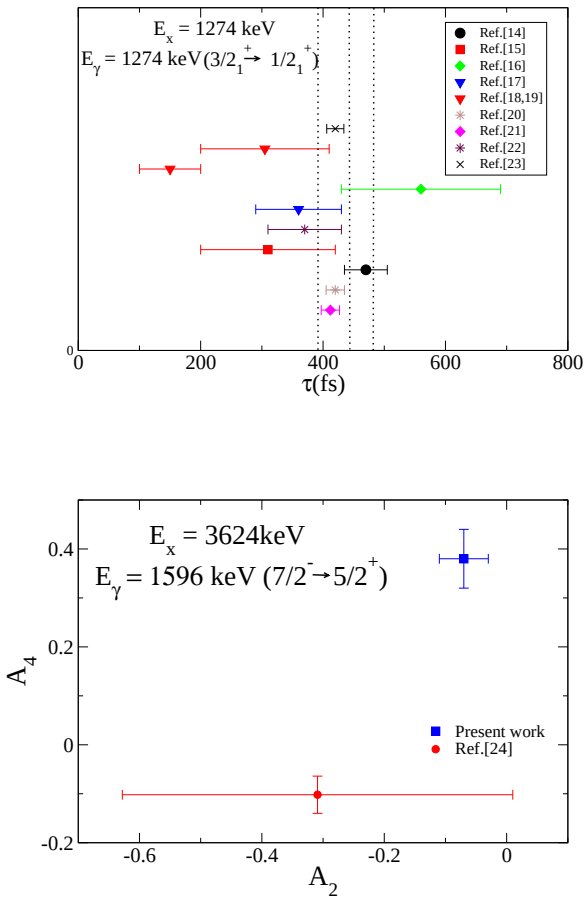

FIG. 46: (Upper panel) The level lifetimes of the 1274 keV ($J^\pi = 3/2^+$) state in the ^{29}Si nucleus from earlier measurements. The results from the present measurement are also included (see text for details). (Bottom panel) Angular distribution coefficients for the 1596 keV ($7/2^- \rightarrow 5/2^+$) transition in the ^{29}Si nucleus from the earlier and the present work (see text for details)

heavy-ion induced fusion-evaporation experiments, wherein the de-exciting gamma-rays were efficiently detected using a large array of high resolution composite γ-ray detectors (Clover) which also facilitate polarization measurements. The experimental findings have been compared with large basis shell model calculations using updated interactions and the results are in close agreement. As a further extension these calculations were also performed for the neighbouring Si (^{28,30}Si nuclei [11, 81]). The calculations for ^{28}Si, could satisfactory reproduce the previously reported deformed states, by Jenkins *et al.* [11]. Further, the predicted negative parity states in ^{30}Si, are in reasonable agreement with the observed level sequences. Interestingly, the calculations did not require any system dependent lowering of the single-particle energies of the $f_{7/2}$ and the

$p_{3/2}$ orbitals, as was found necessary in the previous studies [81–83].

6.2 Previous Study on Si Isotopes

The level structures of Si isotopes ($A = 27 - 30$) are of importance, since they reveal a host of intriguing phenomena. Historically, ^{29}Si, was one of the first light nucleus after ^{25}Al to be interpreted from the point of view of the collective model. Superdeformation (SD) was conventionally associated with $A \sim 150, 130$ & 190 nuclei. SD bands in the light, α-conjugate nuclei, ^{36}Ar [84] and ^{40}Ca [85], has been recently identified. Existence of SD bands in lighter, α-conjugate nuclei such as ^{32}S and ^{28}Si has been theoretical predicted and have motivated several detailed experimental ventures [11] . Based on model calculations, these nuclei are also expected to exhibit clusters, for example one may conceive, the structure of ^{28}Si to be dominated by cluster configurations such as ^{26}Mg + α or ^{12}C + ^{16}O [86]. Thus the level structure of these nuclei provide intriguing examples such as the presence of single particle as well highly deformed structures, including esoteric cluster configurations, and theoretically the complementary model descriptions meet with identical success in interpreting the experimental observations.

The level structure of ^{28}Si was studied by using both the light-ion [87] as well as α like heavy-ion transfer reactions [11]. Since ^{28}Si constitutes the mid-shell nucleus in the *sd* shell, it can be described as having either 12 particles outside the ^{16}O core, or 12 holes in the ^{40}Ca core. As mentioned earlier, both, the spherical shell model using the the universal *sd*-shell (USD) interaction as well as deformed models *viz.* the Hartree-Fock calculations [88] the Nilsson-Strutinski cranking formalism [89, 90] have adequately reproduced the experimental observations. The recent Antisymmetrized Molecular Dynamics (AMD) calculations by Taniguchi *et al.* [86] suggested the presence of a superdeformed (SD) band in ^{28}Si nucleus with ^{24}Mg + α cluster configuration. A similar prediction holds good following the calculations based on shape isomers and clustering [91]. The experimental results are in concurrence with the presence of highly deformed structures in this nucleus.

Most of the experiments performed to investigate the level structure of ^{29}Si utilized light ion induced reactions such as ^{28}Si (d, pγ), $^{27}Al(^{3}He,\ p\gamma)$, $^{26}Mg(\alpha, n\gamma)$ $(n\gamma)$ capture reactions [12, 92–97]. The de-exciting γ-rays were detected using either NaI(Tl) or Ge(Li) detector. The γ-ray angular correlations as well as particle-γ coincidence measurements were performed. The level scheme was extended upto $\sim$ 13 MeV excitation energy [12]. The positive parity sequences were reproduced by the shell model calculations. Three rotational bands with $1/2^+$, $3/2^+$ and $7/2^-$ as the bandhead were assigned in ^{29}Si [12]. There was a possibility of existence of a $5/2^+$ and $1/2^-$ band with prolate deformation. Doppler Shift Attenuation Method was exploited by Tikkanen and co-workers [21] to measure the level lifetimes in ^{29}S, which was populated following the ^{15}N(^{16}O, np)^{29}Si reaction and at incident beam energies of 17, 20 and 22 MeV. The experimental transition strengths, derived from the extracted level lifetime, are compared with shell model calculations, and found to be in satisfactory agreement.

The level structure of ^{30}Si was studied by using both the light [98] as well as heavy ion induced fusion evaporation reactions [81]. The recent study by Steppenbeck *et al.* [81] established the yrast or near yrast states upto and excitation energy of $E_x \sim 15.5$ MeV and spin of $J = 9\hbar$. The spin parity assignments were based on the DCO - ratio and angular distribution measurements. The positive parity energy levels are in agreement with the shell model calculations which were performed using the USD, $USDA$ and $USDB$ interactions. The negative parity states were calculated by allowing $1p - 1h$ excitations across the sd into the fp shell using WBP and $WBP - a$ interactions. The authors have resorted to a nucleus specific tweaking of the single particle energies to arrive at a compliance with the experimental observations. However, the shell model calculations performed by our group [9] indicate that updated interactions in conjunction with proper / adequate truncation scheme successfully reproduced the negative parity level sequences in the neighbouring nuclei, and hence there is a need to re-visit these calculations.

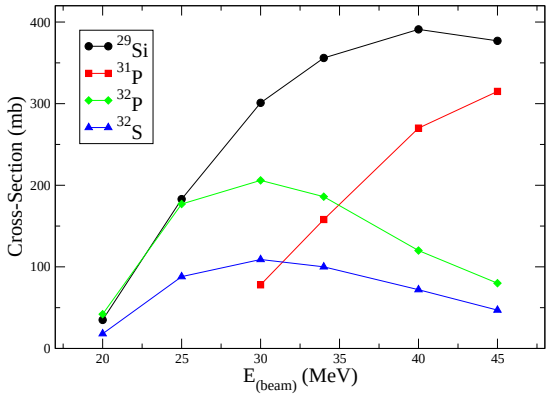

FIG. 47: Predictions of the statistical model PACE4 for the ^{16}O + ^{18}O reaction depicting the production cross-section for ^{29}Si, ^{31}P, ^{32}P and ^{32}S nuclei.

6.3 Present Work

High spin states in ^{29}Si have been populated using the ^{18}O(^{16}O, αn) and ^{18}O(^{13}C, $2n$) reactions at incident beam energy of 34 and 30 MeV. The heavy-ion ^{16}O and ^{13}C beams were delivered by the Pelletron facilities at Inter University Accelerator Center (IUAC), New Delhi and Tata Institute of Fundamental Research (TIFR), Mumbai, respectively. As we discussed in the previous chapter the beam energies were optimum for the production / population of ^{29}Si, based on the predictions of the statistical model calculations using PACE4 [69]. The statistical model predictions for the relevant cross-sections as a function of the incident beam energy for the ^{16}O + ^{18}O, reaction is presented Fig. 47. A similar plot for the ^{13}C + ^{18}O reaction was presented in the previous chapter. The multi-Clover detector array, the Indian National Gamma Array (INGA) has been used to detect the de-exciting γ-rays. The details of the experimental setup are discussed in chapter 2. Two and higher fold coincidence events have been recorded and subjected to a detailed offline analysis.

The analysis technique / procedure is identical as detailed in the previous chapter. Most of the transitions belonging to ^{29}Si exhibited Doppler effects (shifts and shapes depending on the level lifetimes). Hence, the data have been sorted into angle dependent $E_\gamma - E_\gamma$ matrices with the 90° detectors on one axis and the detectors at

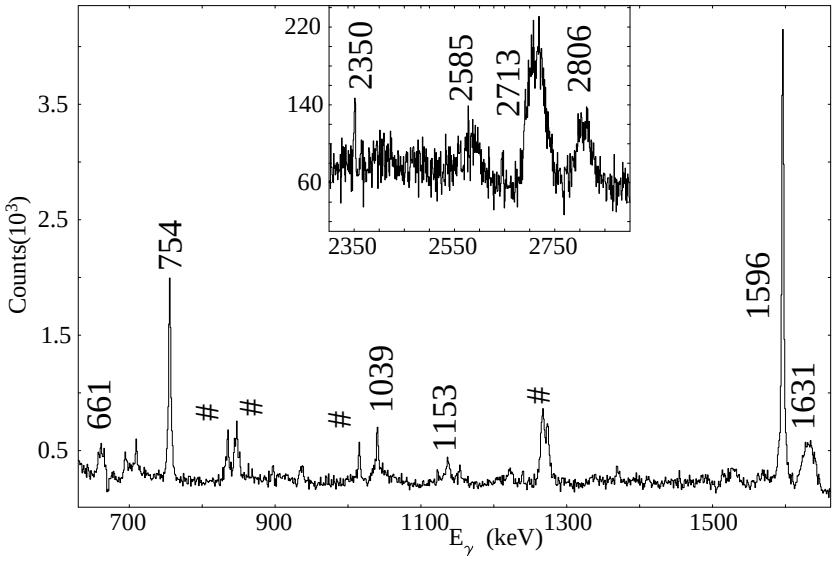

FIG. 48: Coincidence spectrum with gates on the 1274 keV and the 2028 keV transitions in ^{29}Si. The transitions belonging to the ^{29}Si nucleus are labeled with the respective energies, while the contaminant peaks are identified with sign (#). The inset illustrates the higher energy transitions ($E_\gamma > 2.0 MeV$).

one of the remaining angles on the other axis for subsequent analysis. Fig. 48, depicts the (coincident) transitions observed at 90° with gates on the 1274 keV ($3/2^+ \rightarrow 1/2^+$) and the 2028 keV ($5/2^+ \rightarrow 1/2^+$) transitions in the ^{29}Si nucleus.

As discussed in the previous chapter the substantial Doppler shapes did not permit us to undertake the conventional measurement of the ratio for Directional Correlation from Oriented nuclei (DCO) for multipolarity assignments of the observed γ-ray transitions [10]. The dominant multipolarity of the observed transitions has thus been determined using the anisotropy ratio ($R_{anisotropy}$) [8, 9], defined as, for the present experimental set-up

$$R_{anisotropy} = \frac{I_{\gamma_1}\ (at\ \theta_1\ gated\ by\ \gamma_2\ at\ 90^\circ)}{I_{\gamma_1}\ (at\ \theta_2\ gated\ by\ \gamma_2\ at\ 90^\circ)} \tag{97}$$

As presented in Fig. 49, this method facilitates distinction between transitions of different multipolarities. For the present detector geometry, a gate on a pure dipole transition would lead to $R_{anisotropy} = 1.9$ for pure quadrupole transition and $R_{anisotropy} = 1.0$ for pure dipole transition. In case of gate on pure quadrupole transition,

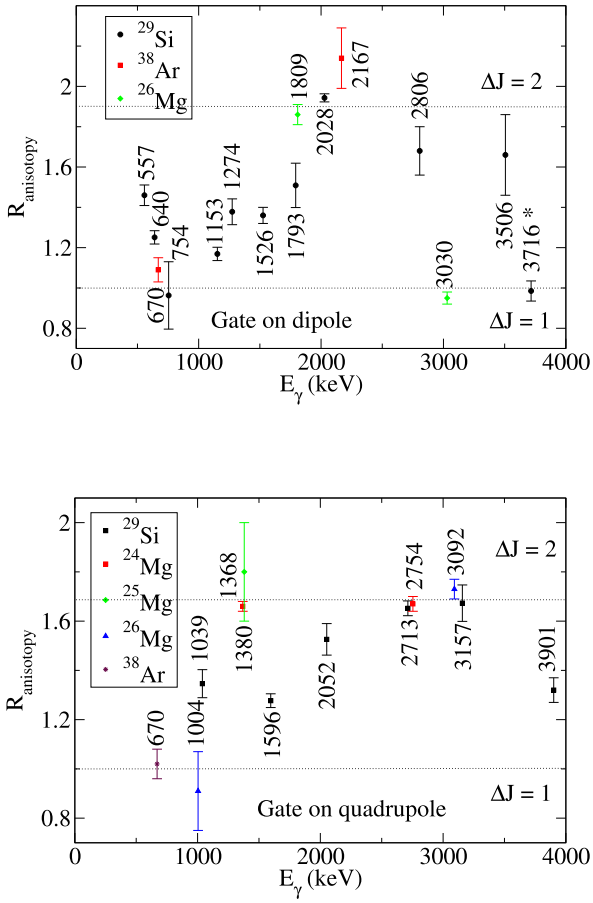

FIG. 49: The experimental $R_{anisotropy}$ values for transitions in ^{29}Si from the present work. The new transition is labeled with *.

$R_{anisotropy} = 1.7$ for a pure quadrupole transition and $R_{anisotropy} = 1.0$ for pure dipole transition. These values have been extracted using transitions of known multipolarities from nuclei populated in the same experiment. The $R_{anisotropy}$ information helps us deduce the dominant multipolarity (change in angular momentum) of the transitions. This information when coupled with the linear polarization measurements, which yields information on the electro-magnetic character of the transition, enable unambiguous spin-parity assignments for the observed levels.

The Clover detector has four identical crystals in a close packed geometry, with a few mm spacing in-between the crystals. This geometry is ideal for linear polarization measurements of the observed γ-ray transitions with any one of the four crystals acting as the scatterer and the two adjacent crystals, which correspond to mutually perpen-

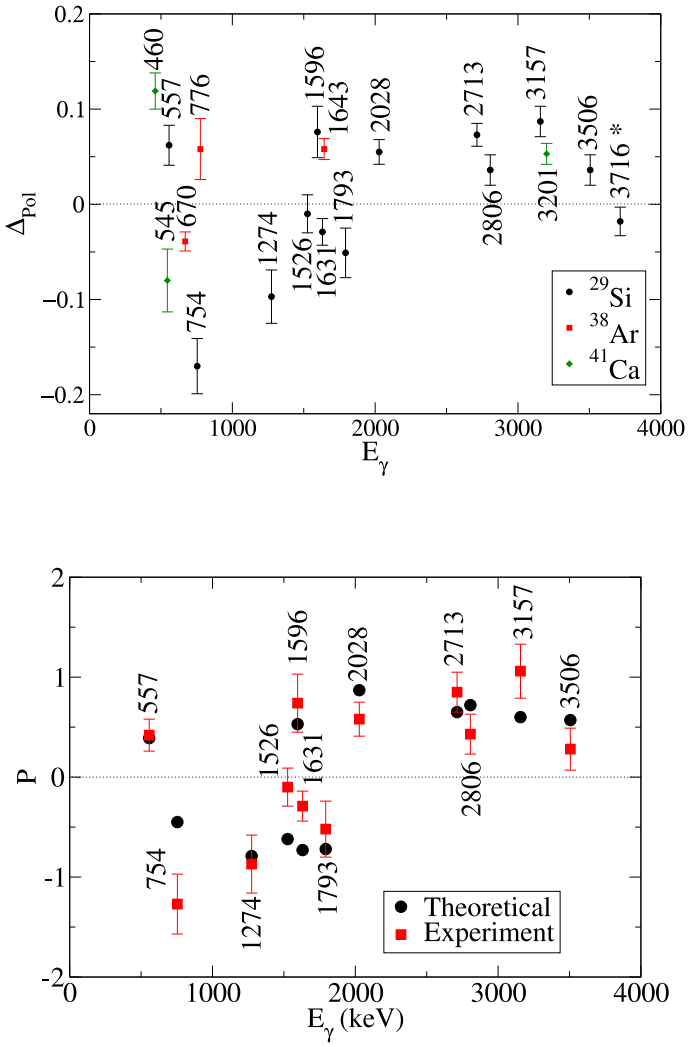

FIG. 50: Plot of polarization asymmetry for transitions in ^{29}Si from the present measurements (upper panel). Transitions with established electro-magnetic nature in ^{41}Ca and ^{38}Ar have been included for reference. These nuclei have been populated following the interaction of the beam halo with the aluminum target frame. The corresponding polarization (P) values have been also plotted (lower panel). The new transition identified in the present work has been labeled with *.

dicular directions, as the absorbers. The preferential scattering of electric and magnetic transitions respectively in the direction perpendicular and parallel to the reaction plane, allows us to identify the electro-magnetic nature of the transition. Since intensity is proportional to the differential cross section of Compton scattering, the intensities of the mutually perpendicular Compton scattered γ-rays, denoted by $N_\perp$ and $N_\parallel$, are used to

obtain polarization asymmetry, Δ_{Pol} defined as,

$$\Delta_{Pol} = \frac{aN_{\perp} - N_{\parallel}}{aN_{\perp} + N_{\parallel}}, \tag{98}$$

The geometrical effects of the array have to be incorporated in the estimation of the polarization asymmetry. This is represented by the asymmetry term, a, obtained from the ratio of $N_{\parallel}$ to $N_{\perp}$ for γ-rays from radioactive sources which are characteristically unpolarized. This constant was obtained in the previous studies carried out using the same detector setups [8, 9] and has been used for the present measurements. Fig. 50 illustrates the polarization asymmetry for the transitions in ^{29}Si along with those for transitions of known electro-magnetic nature belonging to ^{38}Ar and ^{41}Ca nuclei populated in same experiment due to the interaction of the beam halo with the aluminum target holder, included here for reference. From the experimental asymmetry, the polarization ($P = \Delta_{Pol}/Q$, Q being the polarization sensitivity) has been obtained for the transitions, using the method detailed in Ref.[8], and are presented in Fig. 50. The theoretical polarization for these transitions, using the known mixing ratios from the previous studies [23], have also been calculated and included in the plot (Fig. 50). The agreement between the theoretical and experimental polarization is satisfactory.

The observation of Doppler shapes / shifts in the present work facilitated the determination of level lifetimes using the Doppler shift attenuation method (DSAM). Conventionally such measurements have been carried out using a **thin** target on a high-Z **elemental backing**. The thin target ensures that the recoils do not loose substantial energy in the target, and the slowing down process occurs entirely within the elemental backing, wherein the process for the energy-loss is rather well understood. This is in gross discordance with the present experimental scenario, as we have a thick molecular target. Hence, the LINESHAPE [53] package, extensively used for analysis of the observed Doppler shapes and shifts has been substantially modified to cater to the present use of a thick molecular target, as detailed in Ref.[7]. The slowing down of the residue of interest in the thick Ta_2O_5 target has been simulated using the updated stopping powers calculated using the SRIM [99] software and the variation of the cross section for the production of the residues along the target thickness with evolving beam energy, has been obtained from the statistical model calculations using the PACE4 [69], are incorporated in the LINESHAPE code. The results of the analysis are summarized

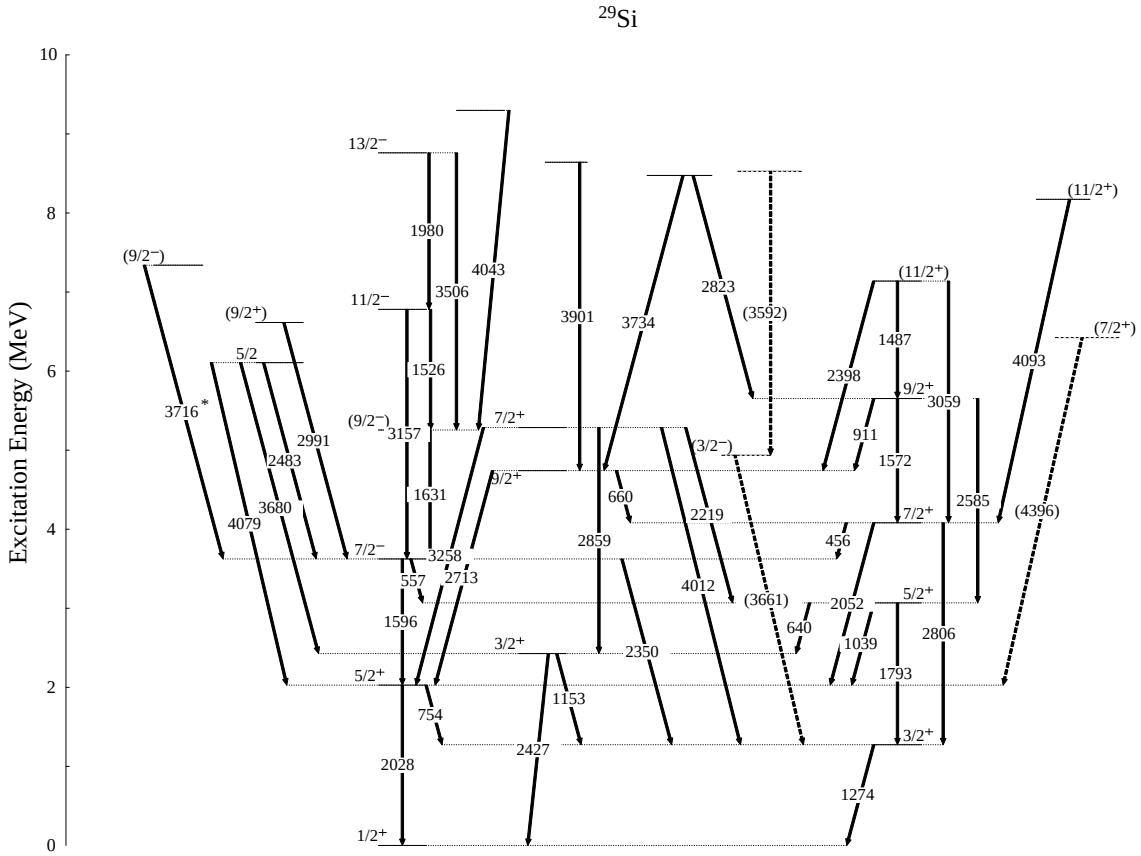

FIG. 51: The level scheme of the ^{29}Si nucleus from the present work. The new level and the de-exciting transition has been labeled with *. The levels and the transitions that are known from the previous studies but could not be conclusively confirmed in the present work have been indicated with dotted lines.

in the subsequent section.

6.4 Results

The level scheme of the ^{29}Si nucleus, following the present study, is illustrated in Fig. 51. Table IX records the level energies, the de-exciting γ-ray transitions, branching ratios and the spin-parity assignments. Most of the levels and the transitions in ^{29}Si, reported in the previous studies, have been confirmed in present (both the reactions) effort with high resolution spectroscopic tools in the form of large array of Compton suppressed Clover detectors. In addition, one new negative parity level at $E_x = 7340$ keV de-exciting by 3716 keV γ-ray transition has been identified in this work.

The 1631 keV transition de-exciting the 5255 keV ($9/2^-$) level is of special relevance. This transition was discussed in particular, in the previous studies, especially by Bardin *et al.* [79, 80] to explore the development of collectivity in this nucleus. The negative parity sequence could be a possible candidate for a rotational structure. The angular distribution for 1631 keV transition was performed by Bardin *et al.* [79] and the results are summarized in Table I in Ref.[79]. Based on these measurements, the 1631 keV γ-ray was assigned a mixed nature, and identified to have an admixture of quadrupole-dipole multipolarity with a substantial mixing (δ = -0.49 $\pm$ 0.07, [79]). The high mixing ratio for this transition, did not permit us to ascertain its dominant multipolarity. However, such a high mixing ratio leads to the possibility of this transition having either a M1+E2 or an E2+M3 electro-magnetic nature. An unambiguous conclusion based solely on the angular distribution measurement is difficult. Nevertheless, if we were to consider the theoretical polarization these two possibilities produce widely contrasting results. The M1+E2 assignment would result in a theoretical polarization of -0.7, which is in reasonable agreement with the experimental value (-0.3$\pm$0.1), and on the other hand, the E2+M3 possibility predicts a theoretical polarization value of +0.8, that is widely discrepant with respect to the measurements. The possibility of the transition being M1+E2 is further corroborated by the lifetime of the 5255 keV level, that was previously reported to be 118 fs and has been confirmed in the present work. The alternative E2+M3 mixed character would result in much longer level lifetime, due to it's highly retarded nature.

The 1596 keV transition de-exciting the 3624 keV ($7/2^-$) level [23] has previously been studied by Becker *et al.* [24]. The authors have performed the particle-γ angular correlations, where the γ-detector employed was a NaI(Tl) scintillator. The reported angular distribution coefficients have large uncertainties. In Figure 10 of Ref.[24] illustrates simultaneous fitting for the 1596 and 2028 keV cascade of γ-transitions which sequential decay from the 3624-keV level this analysis indicates that the allowed spin state of the above mentioned level is 7/2. From the previous measurements the spin and parity of this level was assigned as $(5/2, 7/2)^-$. Hence the spin parity of the 3624 keV level was assigned by Becker *et al.* to be $7/2^-$. The 1596 keV transition was assigned to be mixed dipole-quadrupole character, though with a high

TABLE IX: Details of γ-ray transitions of the ^{29}Si nucleus, observed in the present work.

$E_i^b(keV)$	$E_\gamma^a(keV)$	$E_f^b(keV)$	Br(%)	J_i^π	J_f^π	$R_{anisotropy}$	Δ_{Pol}	Assignment
1274	1273.8±0.4	0	100	$3/2_1^+$	$1/2_1^+$	1.37 ± 0.06^D	-0.097±0.028	M1+E2
2028	754.2±0.4	1274	7.94±0.10	$5/2_1^+$	$3/2_1^+$	0.96 ± 0.17^D	-0.170±0.029	M1+E2
	2027.6±0.5	0	92.06±0.60	$5/2_1^+$	$1/2_1^+$	1.94 ± 0.02^D	0.055±0.013	E2
2427	1152.6±0.8	1274		$3/2_2^+$	$3/2_1^+$	1.17 ± 0.03^D		D+Q
	2427.0 ±2.0	0		$3/2_2^+$	$1/2_1^+$			$M1+E2^N$
3067	640.0±0.6	2427	0.42±0.05	$5/2_2^+$	$3/2_2^+$			
	1038.8±0.3	2028	16.03±0.36	$5/2_2^+$	$5/2_1^+$	1.35 ± 0.06^Q		$M1+E2^N$
	1792.6±0.2	1274	83.55±1.03	$5/2_2^+$	$3/2_1^+$	1.51 ± 0.11^D	-0.051±0.026	M1+E2
3624	556.7±0.2	3067	11.23±0.46	$7/2_1^-$	$5/2_2^+$	1.46 ± 0.05^D	0.062±0.021	E1+M2
	1595.9±0.4	2028	86.57±1.70	$7/2_1^-$	$5/2_1^+$	1.27 ± 0.03^Q	0.076±0.027	E1+M2
	2349.6±0.4	1274	2.19±0.18	$7/2_1^-$	$3/2_1^+$			
4080	456.4±0.5	3624	< 1.00	$7/2_1^+$	$7/2_1^-$			
	2051.9±0.8	2028	32.00±10.00	$7/2_1^+$	$5/2_1^+$	1.52 ± 0.06^Q		$M1+E2^N$
	2806.0±2.0	1274	67.00±18.00	$7/2_1^+$	$3/2_1^+$	1.68 ± 0.12^D	0.036±0.016	E2
4741	660.6±0.6	4080	6.00±5.00	$9/2_1^+$	$7/2_1^+$			
	2713.0±2.0	2028	93.00±7.00	$9/2_1^+$	$5/2_1^+$	1.65 ± 0.03^Q	0.073±0.012	E2
4935	3661.0±2.0	1274	100	$(3/2_1^-)$	$3/2_1^+$			
5255	1631.5±0.4	3624	100	$(9/2_1^-)$	$7/2_1^-$		-0.029±0.014	$(M1+E2)^N$
5286	2219.0±2.0	3067		$7/2_2^+$	$5/2_2^+$			
	2859.0±2.0	2427		$7/2_2^+$	$3/2_2^+$			
	3258.0±2.0	2028		$7/2_2^+$	$5/2_1^+$			$M1+E2^N$
	4012.0±2.0	1274		$7/2_2^+$	$3/2_1^+$			
5652	911.5±0.3	4741		$9/2_2^+$	$9/2_1^+$			
	1572.0±2.0	4080		$9/2_2^+$	$7/2_1^+$			$M1+E2^N$
	2585.0±2.0	3067		$9/2_2^+$	$5/2_2^+$			
6107	2483.0±2.0	3624		5/2	$7/2_1^-$			
	3680.0±2.0	2427		5/2	$3/2_2^+$			
	4079.0±2.0	2028		5/2	$5/2_1^+$			$D+Q^N$
6424	4396.0±2.0	2028	100	$(7/2_3^+)$	$5/2_1^+$			$D+Q^N$
6615	2991.0±2.0	3624	100	$(9/2_3^+)$	$7/2_1^-$			
6781	1526.4±0.6	5255	45.00±17.00	$11/2_1^-$	$(9/2_1^-)$	1.36 ± 0.04^D	-0.01±0.02	M1+E2
	3157.0±2.0	3624	54.00±28.00	$11/2_1^-$	$7/2_1^-$	1.67 ± 0.07^Q	0.087±0.016	E2
7139	1487.0±2.0	5652		$(11/2_1^+)$	$9/2_2^+$			$(M1+E2)^N$

continued...

TABLEIX - continued...

$E_i^b(keV)$	$E_\gamma^a(keV)$	$E_f^b(keV)$	Br(%)	J_i^π	J_f^π	$R_{anisotropy}$	Δ_{Pol}	Assignment
	2398.0±2.0	4741		$(11/2_1^+)$	$9/2_1^+$			
	3059.0±2.0	4080		$(11/2_1^+)$	$7/2_1^+$			
7340	3716.0±2.0	3624	100	$9/2_2^-$	$7/2_1^-$	0.98 ± 0.05^D	-0.018±0.015	(M1+E2)
8173	4093.0±2.0	4080	100	$(11/2_2^+)$	$7/2_1^+$			
8475	2823.0±2.0	5652			$9/2_2^+$			
	3734.0±2.0	4741			$9/2_1^+$			
8527	3592.0±2.0	4935	100		$3/2_1^-$			
8642	3901.0±2.0	4741	100		$9/2_1^+$	1.32 ± 0.05^Q		D+Q
8761	1980.0±2.0	6781		$13/2_1^-$	$11/2_1^-$			
	3506.0±2.0	5255		$13/2_1^-$	$(9/2_1^-)$	1.66 ± 0.20^D	0.036±0.016	E2
9298	4043.0±2.0	5255	100		$(9/2_1^-)$			

^{Q} From quadrupole gate. ^{D} From dipole gate. ^{N} Adopted from NNDC.

uncertainty on the mixing ratio ($\delta = 0.02 \pm 0.02$). The transition is significant owing to the associated change in parity and the long ($\sim$ 3.8 ps) level lifetime (compared to neighbouring states). This is indicative of a change in the structure therein. Indeed, the 3624 keV $(7/2^-)$ level has been interpreted as the band-head of the $K^\pi = 7/2^-$ band in the previous studies [14, 80]. Such a scenario warrants a re-examination of the 1596 keV transition with the contemporary spectroscopy tools, as used in the present investigation. The $R_{anisotropy}$ value for the transition, from the present measurement, is 1.27 ± 0.03 in a quadrupole gate, indicating a dominant dipole nature with quadrupole admixture, while the value of polarization asymmetry (0.08 ± 0.03) is suggestive of a principally electric behaviour. In the light of these results, the 1596 keV has been interpreted as a mixed E1+M2 transition in the present work. The mixing ratio of 0.14 ± 0.04 has been estimated from the angular distribution analysis of the 1596 keV γ-ray, following the prescription detailed in chapter 3. The fit to the angular distribution from the current study and the χ^2 analysis is illustrated in Fig. 52. The theoretical polarization (P) for the transition, calculated using this mixing ratio, is in reasonable agreement with the experimental result. It is interesting to note a similar feature in the neighbouring ^{31}Si isotope wherein an E1+M2 transition (1438 keV), with $\delta = 0.11 \pm 0.01$ [23], de-excites the lowest negative parity state at 3133 keV

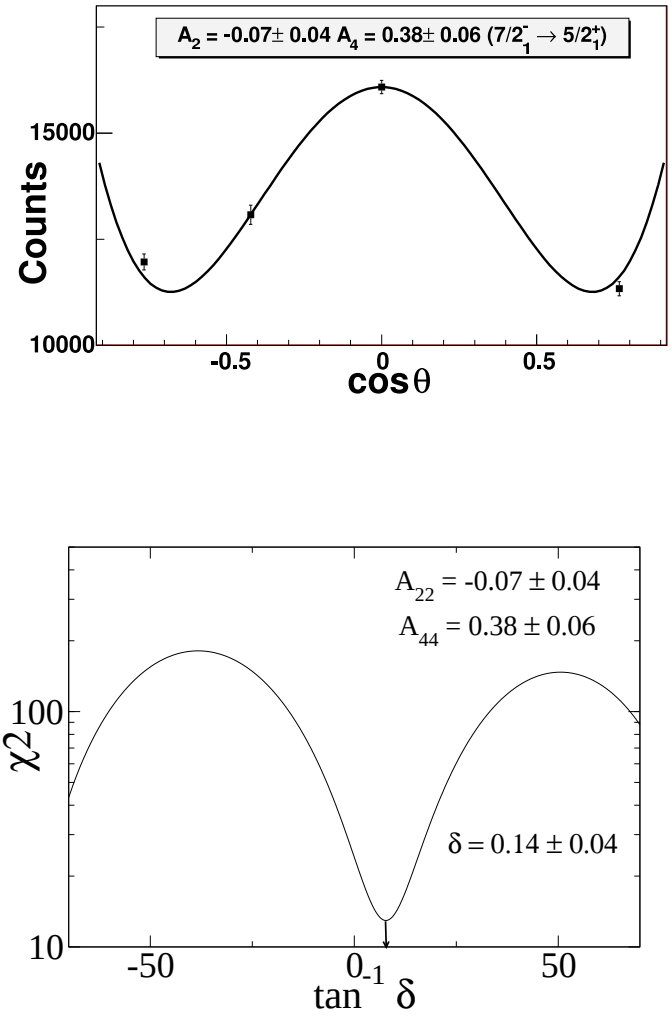

FIG. 52: The angular distribution fit for the 1596 keV ($7/2^-_1 \rightarrow 5/2^+_1$) transition in the ^{29}Si nucleus and the corresponding χ^2 analysis for obtaining the mixing ratio.

($7/2^-$). However, the experimental B(E1) value for the 1596 keV (^{29}Si) transition is $\sim 8\times10^{-5}$ Wu while that for the 1438 keV transition (^{31}Si) is $\sim 61\times10^{-5}$ Wu, which could possibly indicate an enhancement in the collectivity with increasing neutron number in the Si isotopes.

As already mentioned in the preceding discussions, observation of Doppler shapes / shifts in the γ-transitions of ^{29}Si, enabled extraction of the corresponding level lifetimes using the DSAM technique. The modified LINESHAPE package [7] has been used for the purpose. Least square fitting of the observed shapes to the calculated ones have been carried out simultaneously at five different angles, 148°, 123°, 90°, 57°,

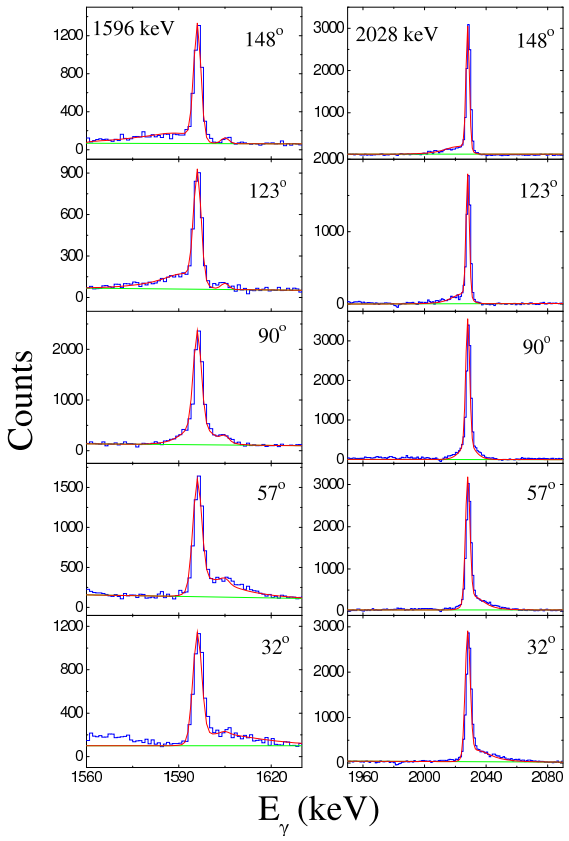

FIG. 53: Representative fits to the Doppler shapes observed for the 1596 keV ($7/2^-_1 \rightarrow 5/2^+_1$) and the 2028 keV ($5/2^+_1 \rightarrow 1/2^+_1$) transitions in ^{29}Si nucleus.

32°, for determination of the level lifetimes. The parameters for the fitting procedure included the level lifetime, the side-feeding time, the peak height, the contaminant peak(s) and the background parameters. The results of the lifetime analysis in case of ^{29}Si are recorded in Table X while Fig. 53 illustrates the representative fits to the Doppler shapes for the 1596 keV and the 2028 keV transitions. Level lifetimes that could be extracted from gates on transitions above (GTA) have been quoted as definite values while those that could be analyzed only with gates on transitions below (GTB) have been stated as the upper limits, after incorporating the side feeding contribution. The dominant uncertainties on the quoted lifetimes stem from the uncertainties in the stopping power estimates that are typically $\sim$ 10%. Thus, the stopping powers have been varied by $\pm$10% and the resulting dispersions in the level lifetimes have been included in the quoted uncertainties. Most of the level lifetimes / limits derived in the present study are in agreement with the previously reported values [23]. However, the level lifetime for E_x = 3624 keV, which de-excites

TABLE X: Lifetimes of the states in ^{29}Si from the present work in comparison to the previously reported values. The quoted uncertainties include the effect of the uncertainties in the stopping powers. Please refer to the text for details.

J_i^π	E_x	E_γ	τ (fs)	
			Present	NNDC
	(keV)	(keV)	Work	
$3/2_1^+$	1274	1274	444^{+39}_{-53}	420^{+14}_{-14}
$5/2_1^+$	2028	2028	444^{+44}_{-40}	442^{+14}_{-14}
$5/2_2^+$	3067	1793	$< 28^{+3}_{-3}$ [a]	48^{+1}_{-1}
$7/2_1^-$	3624	1596	2541^{+226}_{-190}	3795^{+130}_{-130}
$7/2_1^+$	4080	2806	$< 155^{+27}_{-10}$ [a]	63^{+17}_{-17}
$9/2_1^+$	4741	2713	$< 116^{+20}_{-18}$ [a]	52^{+10}_{-10}
$(9/2_1^-)$	5255	1631	$< 169^{+24}_{-28}$ [a]	118^{+6}_{-6}
$11/2_1^-$	6781	1526	$< 35^{+5}_{-7}$ [a]	22^{+3}_{-3}
$9/2_2^-$	7340 [b]	3716	$< 3^{+1}_{-1}$ [a]	
	8642	3901	$< 32^{+12}_{-13}$ [a]	< 20
$13/2_1^-$	8761	3506	$< 40^{+12}_{-10}$ [a]	27^{+6}_{-6}

[a] The dominant side-feeding allowed for assignment of only an upper limit on the lifetime.

[b] New level, first observed in the present work.

by the 1596 keV transition, has been determined to be $\tau = 2.5 \pm 0.2$ ps, from the present work, and is at variance with the previously reported value of $\tau = 3.8 \pm 0.1$ ps. This being the lowest negative parity state, accurate estimation of the level and the transition properties could contribute to refining the model calculations. Upper limit on the lifetime has also been obtained for the $E_x = 7340$ keV level, de-exciting by the 3716 keV transition, that has been reported for the first time in the present work.

6.5 Shell Model Calculations

Large basis shell model calculations have been carried out for the ^{29}Si nucleus and the neighbouring ^{28,30}Si isotopes using the shell model code NuShellX@MSU [57]. The $USDA$ [75] and the $SDPFMW$ [10] interactions have been used. The details of these

interactions are outlined in the previous chapter. The basis space used was either *sd*, consisting of the $d_{3/2}$, $s_{1/2}$ and $d_{5/2}$ orbitals, or the $sd-pf$, consisting of the *sd* and the $f_{7/2}$, $p_{3/2}$, $p_{1/2}$ and $f_{5/2}$ orbitals. For all the calculations the transition probabilities ($B(M1)$ and $B(E2)$) have been calculated using the effective g-factors and the effective charges discussed previously. The specific features and results of these calculations are described in the subsequent sections.

6.5.A. Calculations for ^{29}Si

The positive parity states in the ^{29}Si nucleus have been calculated using both the $USDA$ and the $SDPFMW$ interactions with only the *sd* model space considered in both cases. The results for ^{29}Si are presented in Tables XI and XII. The level energies and the lifetimes for the positive parity states from the calculations are in reasonable agreement with the experimental values (Table XI). The negative parity states in this nucleus have been calculated for the first time in the present work, using $1\hbar\omega$ excitations, *ie.*, excitation of one nucleon from the *sd* into the *fp* orbitals. The predictions exhibit satisfactory conformity with the experimental measurements.

The transition probabilities, *viz.* $B(M1)$ and $B(E2)$ values of the transitions for which the branching ratios could be determined in the present investigation, have also been compared with the shell model calculations (Table XII) and found to be in adequate concurrence.

The ^{29}Si nucleus, being a mid-shell nucleus, has adequate number of valence nucleons in the *sd* shell itself, and hence is expected to manifest deformation characteristics [79]. The deformation characteristics can be inferred from the quadrupole moment. The quadrupole moment quantifies the amount of deviation of electric charge distribution from spherical symmetry. The spectroscopic quadrupole moment Q (obtained in the laboratory frame) is related to the intrinsic quadrupole moment Q_0 (defined in body fixed frame), and the deformation β, as

$$Q = Q_0 \left(\frac{3K^2 - J(J+1)}{(J+1)(2J+3)} \right) \tag{99}$$

TABLE XI: Comparison of experimental and shell model calculated level energies and lifetimes in ^{29}Si. States with lifetimes (or limits) measured in the present work have been marked in boldface.

Experimental			Shell Model Calculation			
E_x	J^π	τ	USDA		SDPFMW	
			E_x	τ	E_x	τ
(keV)		(fs)	(keV)	(fs)	(keV)	(fs)
1274	$3/2_1^+$	$\mathbf{444}^{+39}_{-53}$	**1252**	**574**	**1394**	**829**
2028	$5/2_1^+$	$\mathbf{444}^{+44}_{-40}$	**2062**	**297**	**2123**	**282**
2427	$3/2_2^+$	$26\ ^{+1}_{-1}$	2578	12	2633	13
3067	$5/2_2^+$	$\mathbf{48}^{+1}_{-1}$	**3256**	**24**	**3516**	**21**
4080	$7/2_1^+$	$\mathbf{63}^{+17}_{-17}$	**4219**	**43**	**4412**	**46**
4741	$9/2_1^+$	$\mathbf{52}^{+10}_{-10}$	**4593**	**81**	**4780**	**65**
5286	$7/2_2^+$	9^{+4}_{-4}	5128	11	5221	9
5652	$9/2_2^+$	74^{+4}_{-4}	5486	77	5783	64
6424	$(7/2_3^+)$	<20	5942	32	5881	16
6615	$(9/2_3^+)$	<20	6795	34	6991	33
7139	$(11/2_1^+)$	42^{+14}_{-14}	7049	42	7307	40
8173	$(11/2_2^+)$	<20	7967	13	8120	13
3624	$7/2_1^-$	$\mathbf{2541}^{+226}_{-190}$			**3485**	
5255	$\mathbf{(9/2_1^-)}$	$\mathbf{118}^{+6}_{-6}$			**5159**	**83**
6781	$11/2_1^-$	$\mathbf{22}^{+3}_{-3}$			**6546**	**34**
7340	$9/2_2^-$	$<\mathbf{3}^{+1}_{-1}$			**8788**	**12**
8761	$13/2_1^-$	$\mathbf{27}^{+6}_{-6}$			**8383**	**21**

and

$$B(E2 : J_i \rightarrow J_f) = \frac{5}{16\pi} e^2 Q_0^2 < J_i K 20 | J_f K >^2 \tag{100}$$

Where K is the projection of the total angular momentum J on the quantization axis of the intrinsic system. The Clebsch-Gordon-coefficient $< J_i K 20 | J_f K >$ represents the coupling of the angular momenta in the intrinsic frame.

The shell model prediction provide us with the spectroscopic quadrupole moment Q, which in turn can be used to calculate Q_0. The sign and magnitude of Q_0 provide

TABLE XII: Comparison of the experimental transition probabilities and branching ratios of the ^{29}Si nucleus, wherever possible, with those from the shell model calculations.

			Experimental			Shell Model					
E_x	E_γ	M				USDA			SDPFMW		
(keV)	(keV)		B(M1)	B(E2)	BR	B(M1)	B(E2)	BR	B(M1)	B(E2)	BR
			(μ_n^2)	(e^2fm^4)		(μ_n^2)	(e^2fm^4)		(μ_n^2)	(e^2fm^4)	
1274	1274	M1+E2	$0.06^{+0.01}_{-0.01}$	$19.08^{+2.58}_{-1.54}$	1.00	0.05	28.36	1.00	0.02	34.81	1.00
2028	2028	E2		$49.29^{+5.42}_{-4.07}$	0.92±0.01		64.09	0.87		63.31	0.94
3067	1793	M1+E2	$0.16^{+0.01}_{-0.01}$	$48.21^{+2.09}_{-1.93}$	0.83±0.01	0.21	71.90	0.82	0.21	58.16	0.80
4080	2806	E2		$49.88^{+18.43}_{-10.59}$	0.67±0.18		43.76	0.54		53.10	0.74
	2052	M1+E2	$0.03^{+0.01}_{-0.01}$	$0.72^{+0.27}_{-0.15}$	0.32±0.10	0.05	0.60	0.40	0.02	2.68	0.23
4741	2713	E2		$99.29^{+23.64}_{-16.02}$	0.93±0.07		94.06	0.98		93.88	0.99
5255	1631	(M1+E2)	$0.09^{+0.01}_{-0.01}$	$93.49^{+5.05}_{-4.52}$	1.00				0.12	157.10	1.00
6781	1526	M1+E2	$0.30^{+0.05}_{-0.04}$	$166.54^{+26.30}_{-19.98}$	0.45±0.17				0.28	143.90	0.48
	3157	E2		$63.86^{+10.08}_{-7.66}$	0.54±0.28					46.02	0.52

us with an indication into the associated deformation characteristics. A change in the sign of Q_0, within a given band is indicative of a shape evolution within the band. However caution needs to be exercised before interpreting the shape evolution with the change in sign of Q_0.

For $K = 0$ bands, a change in sign of Q_0 cannot be ascribed to the K and J dependent factor and has to be identified with a change of shape.

On the other hand for $K \neq 0$ bands, there is a domain with $3K^2 > J(J+1)$ where in a change in sign of Q_0 is definitely associated with a corresponding shape.

Hence a change in sign of Q_0 upto the said spin can only result from a change in the sign of Q which originates from a change in the intrinsic shape of the nucleus.

For the sequence of levels $E_x(J^\pi)$ = 3624 $(7/2^-)$, 5255 $(9/2^-)$, 6781 $(11/2^-)$, the calculations indicate an oblate deformation at the lowest spin, represented by $Q \sim$ -30

efm^2 and $Q_0 \sim$ -63 mb, evolving to a prolate deformation, with $Q \sim 2$ efm^2 ($Q_0 \sim 217$ mb), at $J^\pi = 11/2^-$. In particular, the calculated $|Q_0| = 68$ fm^2, for the state $J^\pi = 9/2^-$ of this sequence, is in excellent overlap with the results of Bardin *et al.* [79] ($|Q_0| = 66 \pm 9$ fm^2). It is interesting that the present large basis shell model calculations corroborate the transitional characteristics of this mid-shell ^{29}Si nucleus. The previous studies have reported a considerably higher B(E2) value ($\sim$ 100-200 e^{2}fm^4) particularly for the aforesaid negative parity sequence which is also reproduced by the present calculations (Table XII). The success of the shell model calculations in reproducing the indicators / markers for deformation, may imply an accurate inclusion of most of the dominant multi-particle configurations in the two-body matrix elements. These results do indicate with a considerable level of unambiguity, the presence of deformation in this nucleus. The success of the shell model approach in reproducing these deformation characteristics in ^{29}Si provided the motivation in exploring the strongly deformed structures, identified in the neighbouring ^{28}Si isotope.

6.5.B. Deformation Characteristics in ^{28}Si

As we discussed earlier that the large number of nucleons within one major oscillator shell *viz.* the *sd* shell is expected to favour, collective features in mid-shell transitional nucleus. For example the recent study on ^{28}Si, by Jenkins *et al.* [11] have indeed confirmed these deformed structures and have proposed a candidate superdeformed band in the same. Antisymmetrized Molecular Dynamics (AMD) calculations [86] have been found to corroborate the experimental observations. Calculations have been carried out in the present work to explore the possibility of interpreting the aforesaid bands in the ^{28}Si nucleus within the shell model framework. The positive parity states, reported to be constituting these deformed bands, have been calculated using the $USDA$ and the $SDPFMW$ interactions. Both these calculations have been performed, only by $0\hbar\omega$ configuration (nucleon excitation within the *sd* shell was only allowed).

Table XIII summarizes the results of these calculations for ^{28}Si [11]. The observed excitation energies from the measurements have been well represented in these calcula-

TABLE XIII: The shell model calculations for the bands identified in the ^{28}Si nucleus, compared to the available experimental results.

		Experimental				Shell Model							
						USDA				*SDPFMW*			
Band	J^π	E_{expt} (keV)	E_γ (keV)	τ_N (fs)	$B(E2)$ e^2fm^4	E_{SM} (keV)	τ (fs)	B(E2) e^2fm^4	Q efm^2	E_{SM} (keV)	τ (fs)	B(E2) e^2fm^4	Q efm^2
Oblate	2_1^+	1779	1779	685±24	$66.85^{+2.43}_{-2.26}$	1940	355	83.56	19.09	1990	320	81.85	18.78
	4_1^+	4618	2839	53±6	$83.48^{+10.66}_{-8.49}$	4549	58	116.90	23.05	4659	52	115.80	23.25
	6_1^+	8544	3926	16±1	$54.68^{+3.64}_{-3.22}$	8395	10	98.75	28.65	8457	10	100.60	28.69
	8_1^+	14642	6098			14305	2	66.49	25.56	14212	2	73.42	26.82
SD	2_8^+	9796	3106			10693	6	2.12	-8.56	10688	7	1.81	-9.66
			8018					2.03				1.51	
	4_7^+	10946	2687	22±14		11481	39	9.47	10.87	11550	15	0.92	3.55
			3530					0.23				1.40	
			3565					0.15	10.87			0.18	
			9167					0.00				0.39	
	6_6^+	12865	1919			13423	6	3.84	12.46	13591	8	0.50	10.21
			3700					0.00				0.04	
			5977					9.07				4.83	
			8247					0.18				0.01	
Prolate	0_3^+	6691	4912	212±14	$1.34^{+0.10}_{-0.08}$	7478	85	1.83	0.00	7235	46	4.51	0.00
	2_2^+	7381	5602	7±3		7524	8	14.31	-10.28	7521	12	11.38	-7.36
			7381		$1.91^{+1.44}_{-0.57}$			0.94				0.29	
	4_3^+	9165	1749	40±4	$62.32^{+6.92}_{-5.67}$	9369	49	63.15	-4.71	9489	68	65.56	-9.54
			1784		$158.05^{+17.56}_{-14.37}$			1.17				0.03	
			4547					1.61				2.31	
			7386		$0.44^{+0.05}_{-0.04}$			0.47				0.15	
	6_4^+	11509	2344	13±3	$186.29^{+55.88}_{-34.93}$	11953	16	30.37	8.67	11815	16	43.06	0.99
			4621		$17.27^{+5.19}_{-3.24}$			16.67				17.15	
			6891		$0.84^{+0.25}_{-0.16}$			0.09				0.24	
vibr.	0_2^+	4979	3200	50±3	$48.63^{+3.11}_{-2.75}$	4821	58	70.12	0.00	5013	47	69.04	0.00
	2_5^+	8259	3280	14±3	$30.70^{+8.38}_{-5.42}$	8860	24	20.81	0.32	8665	14	1.89	9.37
			6480		$4.13^{+1.12}_{-0.72}$			0.46				0.01	

		Experimental				Shell Model							
						$USDA$				$SDPFMW$			
Band	J^π	E_{expt}	E_γ	τ_N	$B(E2)$	E_{SM}	τ	B(E2)	Q	E_{SM}	τ	B(E2)	Q
		(keV)	(keV)	(fs)	e^2fm^4	(keV)	(fs)	e^2fm^4	efm^2	(keV)	(fs)	e^2fm^4	efm^2
(K=3^+)	3_1^+	6277	1659	1125±86		6460	2324	10.27	11.57	6163	5475	6.66	13.99
			4498					0.00				0.00	
	4_2^+	6888	5109	48±3	$4.88^{+0.32}_{-0.29}$	7069	23	9.76	4.74	7032	30	8.22	4.99
	5_1^+	8945	2057	84±9		9302	42	88.15	2.43	9227	56	85.74	4.07
			4327					5.87				5.11	
	6_3^+	11331	6713	<30	< 1.99	11531	91	0.00	6.56	11508	42	0.38	13.48
	7_2^+	13710	5166			14352	13	0.12	12.70	14374	8	0.00	8.67

TABLE XIV: Static intrinsic quadrupole moment of the ground state oblate band and the excited prolate (normal deformed) band in ^{28}Si from the present shell model calculations (using $USDA$ interaction).

Band	J^π	Q (Theo.) (efm^2)	Q_0 [a] (mb)	B(E2) (Theo.) (e^2fm^4)	$\lvert Q_0\rvert$ [b] (mb)
	2^+	19.09	-668	83.56	648
	4^+	23.05	-634	116.90	641
Oblate					
	6^+	28.65	-716	98.75	562
	8^+	25.56	-607	66.49	450
	2^+	-10.28	360	-	
Prolate	4^+	-4.71	130	1.17	64
	6^+	8.67	-217	30.37	312

[a] Calculated using Eq (99)
[b] Calculated using Eq (100)

tions. The experimental transition probabilities *viz.* $B(E2)$ values for the intra-band $E2$ transitions have been determined, based on inputs from the NNDC database [23] and compared with the calculations. For the ground state oblate band, the

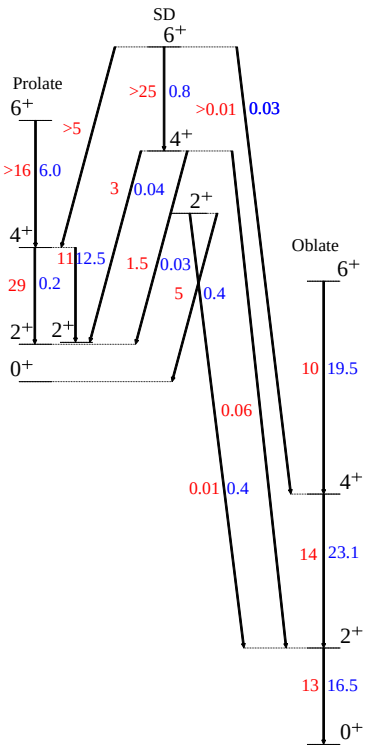

FIG. 54: Comparison of the $B(E2)$ transition probabilities (in Wu), in ^{28}Si, as reported by Jenkins *et al.* with those from the present calculations (numbers in blue for $USDA$).

experimental trend of an increasing $B(E2)$ followed by a reduction is well reproduced by the calculations. Further, the transition strengths (in Wu) for the oblate (ground state), the prolate (normal deformed) and the candidate for the superdeformed (SD) band in ^{28}Si, as identified by Jenkins *et al.* [11], have been computed and compared in Fig. 54. As seen from the figure, most of the transition probabilities are in qualitative agreement with the experimental results. The deviations in the higher spin states may warrant further experimental and computational investigations. One plausible explanation could be the omission of $2\hbar$ configurations from the present calculations. Such configurations are indeed expected to considerably favour the stabilization of deformed structures in these nuclei. The quadrupole moments for the oblate ground state band and the prolate (normal deformed) bands have also been calculated using Eq (99) and (100) and presented in Table XIV. The values for the quadrupole moments corroborate the oblate assignment for the former while a change of sign of the intrinsic quadrupole moment corresponds to a change of deformation with increasing spin in case of the prolate band. A point worth mentioning is that, for the (proposed) SD

band, the current calculations predict the moment of inertia in the range 5-9 $\hbar^2/MeV$, which is very similar to the reported values in the recent study by Jenkins *et al.* [11]. It is interesting to note that even without the inclusion of the deformation favouring $2\hbar$ configurations, the shell model predictions provide tantalizing indicators for the presence of deformed structures in such mid-shell nucleus.

6.5.C. Re-examining Shell Model Calculations in ^{30}Si

Based on the success of the shell model calculations in reproducing the general deformation characteristics in the ^{28}Si nucleus, as a natural extension to the present efforts, we have extended these calculations to the subsequent higher even-even Si isotope, ^{30}Si. This exercise is of significance because the $N \sim 20$ nuclei [9, 10, 76, 81] have been investigated, both experimentally and theoretically, with specific motivation to explore the effects of intruder states from the *fp* shells on their level structure. It is expected that these configurations would compete and even dominate the level structures at much lower excitation energies than their single particle counterparts. Several factors could contribute to such a significant drop in the excitation energies of these intruder orbitals. The main contribution could arise from the many body correlations, which have a constructive effect on lowering the substantial energy gap between two major shells.

Contemporary investigations into the $sd-pf$ nuclei such as ^{32}P, have attempted to explain the observed level structures by introducing a nucleus specific reduction [82, 83] in the single particle energies of the intruder levels (single particle energy between the $p_{3/2}$ and the $f_{7/2}$ levels), and have attributed the agreement of such (shell model) calculations with the deduced level structure as a signature of the reduced shell gap. However, it may be noted that these calculations have been performed using a large model space and consequently, computational limitation necessitated a truncation of the active model space. It has been well established that an inadequate truncation of the model space renders the ground state less bound [74], resulting in the predicted excitation energies being substantially higher. Further, the crucial ingredient of any

shell model calculation is the choice of appropriate two-body matrix elements. The success of the present shell model calculations for ^{28,29}Si validates the use of the model space and the choice of two-body matrix elements which motivated us to undertake the shell model calculations for ^{30}Si in an analogous way.

Previously, the shell model calculations for the ^{30}Si nucleus have been reported by Steppenbeck *et al.* [81] using the USD, $USDA$ and $USDB$ interactions for the positive parity states and the WBP and the $WBP - a$ interactions for the negative parity sequences. They reported a satisfactory reproduction of the positive parity states in these calculations. The predictions for the negative parity states with WBP interaction had to be shifted down in energy by ~ 2 MeV relative to the ground state. The calculated negative parity states, with the $WBP - a$ interaction, were equally or more discrepant with respect to the data and was ascribed to the inappropriate adjustments to the single particle energies of the $0f_{7/2}$ and $1p_{3/2}$ orbitals.

In the present work, calculations have been carried out for both the positive and the negative parity levels of the ^{30}Si nucleus. The $SDPFMW$ interaction has been used for the purpose. The positive parity states have been have been calculated using the full sd model space ($0\hbar\omega$ excitation) while the the negative parity states have been calculated using the $sd - pf$ model space with $1\hbar\omega$ excitations. The results are presented in Fig 55. The present calculations reproduce the experimental results satisfactorily. The compliance with the experimental data, particularly for the negative parity states, is substantially improved with respect to the previous studies. It is worthwhile to mention that there has been no reduction of the bare single particle energies for the $f_{7/2}$ and $p_{3/2}$ orbitals in the present work. Such adjustments, as mentioned before, have been reported by several other groups in this region [76].

The present work establishes the possibility to adequately interpret the observed level sequences along with the deformation characteristics in the transitional $sd - pf$ nuclei, within the shell model framework through proper choice of the effective interactions and the judicious choice of the active model space.

In conclusion the ^{29}Si nucleus has been studied through heavy-ion induced fusion-

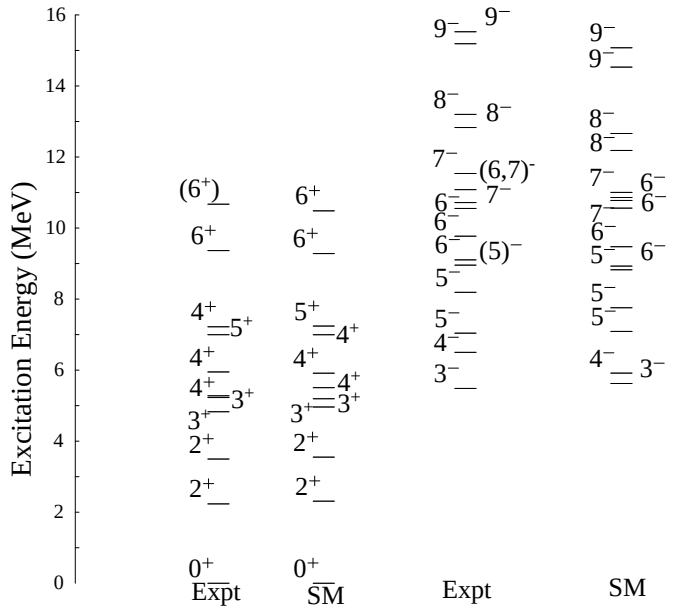

FIG. 55: Comparison of experimental level energies of the ^{30}Si nucleus from the work of Steppenbeck *et al.* with the shell model calculations in the present work. These calculations for ^{30}Si have been carried out using the $SDPFMW$ interaction with purely *sd* configurations for the positive parity states and $1\hbar\omega$ excitations for the negative parity states.

evaporation reaction and, using a large array of Compton suppressed Clover detectors. The spin parity assignments were undertaken and the results are consistent with the previous assignment. One new negative parity level has been identified at $E_x = 7340$ keV, de-exciting by a 3716 keV γ-transition. Level lifetimes have been extracted using DSAM, following substantial modifications to the conventional analysis programs to suit the thick molecular target used in the present setup. Most of the previously reported lifetimes have been reproduced in the present study, either directly or through an upper limit. However, the lifetime of the $E_x = 3624$ keV state, de-exciting by 1596 keV transition, has been determined to be $2.541^{+0.226}_{-0.190}$ ps, has a substantial variance with reported value of 3.795 ± 0.130 ps. This transition is of mixed E1+M2 nature, connecting the lowest negative parity state to the lower lying deformed states. It is interesting to note that a similar transition exists in the neighbouring ^{31}Si isotope, albeit with an enhanced B(E1) value which might indicate an enhancement of collectivity with increasing neutron number in the Si isotopes. Large basis shell model calculations have been carried out for the nucleus and the results are in satisfactory agreement with the experimental findings, including the deformation characteristics.

In view of the success of the calculations for the ^{29}Si nucleus, these have been extended to the neighbouring ^{28}Si and ^{30}Si isotopes. The deformation features in the former have been well represented in the present calculations. The calculations in case of the ^{30}Si nucleus have been carried out without any adhoc lowering of the single particle energies, contrary to the previous studies, and the experimental level energies, both for the positive and the negative parity states, have been satisfactorily reproduced.

Chapter - 7

Summary and Conclusion

The present thesis work is based on the detailed investigation of the nuclear structure of transitional nuclei, such as ^{26}Mg, ^{29}Si at the interface of the *sd* and *pf* shells. These nuclei are uniquely positioned in between the valley of stability and the island of inversion. The level structures of nuclei along the valley of stability are dominated by single particle excitations where as at the island of inversion they are dominated by collective excitations. Thus, the structure of the nuclei in the transitional region are likely to reveal an intriguing interplay between these two degrees of freedom. Hence, these nuclei, provide us an unique laboratory to explore the aforementioned features and their interplay. The excitation of nucleons within the *sd* shell would give rise to positive parity sequences. There are sufficient number of particles within this major shell to induce deformation in these mid-shell nuclei. Further, the excitation of a single nucleon across the $sd-pf$ shell gap, would result in the substantial occupation of the $f_{7/2}$ ($l = 3$) orbital, which is expected to favor deformed structures. The synergy between these two features *viz.* sufficient number of particles in *sd* orbitals and occupation on the *fp* orbitals, leading to deformed structures, could be uniquely probed within the framework of the spherical shell model due to the availability of adequate computational resources coupled to the development of appropriate interactions (inter & intra shell). The aforementioned features motivated the present thesis work.

It is pertinent to mention that all the previous investigations on the level structure of these nuclei were primarily based on light ion induced reactions using a modest detector setup, and consequently, had a substantial scatter with some of them have large uncertainties even at low excitation energies and spin. Hence, the need to re-visit the level structure of these transitional nuclei, using high resolution γ-ray spectroscopy, following heavy-ion induced fusion evaporation reactions. The use of a multi-Clover array was best suited for these measurements, due to the superior detection efficiency of these composite detectors for high energy γ-rays ($E_\gamma \geq 2$ MeV), routinely observed in these nuclei. The use of Clover detector uniquely facilitated linear polarization measurements,

which uniquely help elucidate the electro-magnetic nature of the transitions. The level scheme has been developed from the observed $\gamma - \gamma$ coincidences. Spin parity assignments were made following a consistent analysis of the angular intensity anisotropy and the linear polarization measurements (uniquely possible due to the use of Clover detectors). The observation of the Doppler effect in the energy of the γ-ray, emitted in flight by the recoils as they slow down in the medium, helped us extract the level lifetime using DSAM technique. Large basis shell model calculations were successfully carried out for these nuclei, whose predictions are in agreement with the experimental observables. The results could be summarized as :

- High spin states in ^{26}Mg [8] have been populated utilizing the reaction ^{13}C + ^{18}O, with ^{13}C beam of energy 30 MeV, whereas the ^{16}O + ^{18}O reaction [28] was used to populate the high angular momentum states in ^{29}Si at E_{lab} = 34 MeV.

- Several new transitions have been observed in these nuclei. Accordingly, the level schemes of ^{26}Mg and ^{29}Si have been extended upto $\sim$ 10 MeV ($7\hbar$) and 9.3 MeV ($13/2\hbar$) respectively.

- From the angular anisotropy and the linear polarization measurements, the multipolarity and the electro-magnetic nature of the de-exciting γ transitions has been uniquely assigned.

- The observation of Doppler shapes and shifts in the corresponding γ-transitions were analyzed using a substantially modified LINESHAPE package (optimized for thick molecular target setup [7]) to estimate the level lifetime.

- In these nuclei, the lowest negative parity state is very important, as it provides an indication of the $sd - pf$ shell gap. In ^{29}Si nucleus the first negative parity level (E_x = 3624 keV) de-excites via 1596 keV ($7/2^- \rightarrow 5/2^+$) transition. Our angular distribution data indicate that this transition has an admixture of both ΔJ = 1 & 2, with an approximate 14% mixing, and a dominant electric in nature. However, the level lifetime, has been determined to be $2.541^{+0.226}_{-0.190}$ ps, at substantial variance with the reported value of 3.795 $\pm$ 0.130 ps. It is interesting to note that a similar transition exists in the neighboring ^{31}Si isotope, albeit with an enhanced B(E1) value, which might indicate an enhancement of collectivity with increasing neutron number in these isotopes.

- Large basis shell model calculations using the code NuShellX@MSU were carried out using the $USDA$ and $sdpfmw$ interactions to understand the observed level structure. The positive parity states, originate from the excitation of nucleons within the sd orbitals.

- The observation of negative parity sequences in these nuclei, originate due to the promotion of odd number of nucleons from the sd ($even\ l$) orbitals across one major shell into the unnatural parity fp ($odd\ l$) orbital. These states could be adequately reproduced within the shell model using $1\hbar\omega$ excitations, within the $sd-pf$ model space without taking recourse to any adhoc lowering of the single particle energies. The present study reports the calculations for the negative parity states for the first time in this region.

- From the systematics for the excitation energy of the first (lowest) negative parity state in Mg isotopes, it can be concluded that the decrease in excitation energy with increasing neutron number may correspond to a decrease in the shell gap between the sd & pf shell. This is expected to have a bearing on our understanding of the island of inversion.

- The shell model wave functions were used to obtain the corresponding transition probabilities which were in close agreement with the experimental observables. The model wave function was also used to determine the intrinsic quadrupole moment, and its associated sign presented an evidence for the shape evolution, which is expected for such mid-shell nuclei. Thus it is possible to successfully probe the deformation characteristics in these transitional nuclei, within the framework of the spherical shell model.

Thus, the present thesis work contains a detailed investigation of the level structure of transitional nuclei at the interface of the $sd-pf$ shells using all the available text-book tools and techniques in γ-ray spectroscopy. It establishes the possibility to interpret the observed level sequences in these mid-shell nuclei, along with the deformation characteristics, within the shell model framework. Choice of an appropriate model space and the associated effective interactions, along with a judicious truncation scheme however, remain the crucial inputs for such an exercise.

References

[1] H. Yukawa, Proc. Phys. Math. Soc. Japan **17**, 48 (1935).

[2] H. A. Bethe and R. F. Bacher, Rev. Mod. Phys **8**, 82 (1936).

[3] C. von Weizsäcker, Z Phys **96**, 431 (1935).

[4] M. G. Mayer, Phys. Rev. **74**, 235 (1948).

[5] M. G. Mayer, Phys. Rev. **75**, 1969 (1949).

[6] M. G. Mayer, Phys. Rev. **78**, 22 (1950).

[7] R. Bhattacharjee, S. S. Bhattacharjee, K. Basu, P. V. Rajesh, R. Raut, S. S. Ghugre, D. Das, A. K. Sinha, L. Chaturvedi, U. Garg, et al., Phys. Rev. C **90**, 044319 (2014).

[8] S. S. Bhattacharjee, R. Bhattacharjee, R. Chakrabarti, R. Raut, S. S. Ghugre, A. K. Sinha, T. Trivedi, L. Chaturvedi, S. Saha, J. Sethi, et al., Phys. Rev. C **89**, 024324 (2014).

[9] R. Chakrabarti, S. Mukhopadhyay, R. Bhattacharjee, S. S. Ghugre, A. K. Sinha, A. Dhal, L. Chaturvedi, M. K. Raju, N. Madhavan, R. P. Singh, et al., Phys. Rev. C **84**, 054325 (2011).

[10] R. Chakrabarti, S. Mukhopadhyay, Krishichayan, A. Chakraborty, A. Ghosh, S. Ray, S. S. Ghugre, A. K. Sinha, L. Chaturvedi, A. Y. Deo, et al., Phys. Rev. C **80**, 034326 (2009).

[11] D. G. Jenkins, C. J. Lister, M. P. Carpenter, P. Chowdury, N. J. Hammond, R. V. F. Janssens, T. L. Khoo, T. Lauritsen, D. Seweryniak, T. Davidson, et al., Phys. Rev. C **86**, 064308 (2012).

[12] P. Betz, E. Bitterwolf, A. Burkard, F. Glatz, F. Heidinger, T. Kern, R. Lehmann, S. Norbert, H. Röpke, C. Schneider, et al., Z. Phys. A **309**, 163 (1982).

[13] F. Glatz, S. Norbert, E. Bitterwolf, A. Burkard, F. Heidinger, T. Kern, R. Lehmann, H. Röpke, J. Siefert, and C. Schneider, Z. Phys. A **324**, 187 (1986).

[14] D. C. Bailey, P. E. Carr, J. L. Durell, L. L. Green, M. W. Green, A. N. James, J. F. Sharpey-Schaffer, and D. A. Viggars, J. Phys. A **5**, 596 (1972).

[15] S. I. Baker and R. E. Segel, Phys. Rev. **170**, 1046 (1968).

[16] E. C. Booth and K. A. Wright, Nucl. Phys. **35**, 472 (1962).

[17] P. R. Dekock, J. W. Koen, and W. L. Mouton, Nucl. Phys. A **140**, 190 (1970).

[18] T. R. Fisher, T. T. Bardin, J. A. Baker, and A. D. W. Jones, Bull. Am. Phys. Soc **15**, 600 (1970).

[19] T. W. Retz-Schimdt, S. J. Skorka, H. Morgenstern, and H. Schimdt, C. R. Congr. Intern. Phys. Nucl. **2**, 396 (1964).

[20] D. E. C. Scherpenzeel, G. A. P. Engelbertink, H. J. M. Aarts, C. J. V. D. Poel, and H. F. R. Arciszewski, Nucl. Phys. A **349**, 513 (1980).

[21] P. Tikkanen, J. Keinonen, A. Kuronen, A. Z. Kiss, E. Koltay, E. Pintye, and B. H. Wildenthal, Nucl. Phys. A **517**, 176 (1990).

[22] J. M. J. Wozniak, R. L. Hershberger, and D. J. Donahue, Phys. Rev. **181**, 1580 (1969).

[23] URL `www.nndc.bnl.gov`.

[24] J. A. Becker, L. F. Chase, and R. E. McDonald, Phys. Rev. **157**, 967 (1967).

[25] H. Ejiri and M. J. A. de Voigt, *Gamma - ray and Electron Spectroscopy in Nuclear Physics* (Clarendon Press, Oxford, 1989).

[26] M. Scheck, P. A. Butler, L. P. Gaffney, N. Bree, R. J. Carrol, D. Cox, T. Grahn, P. T. Greenlees, K. Hauschild, A. Herzan, et al., Phys. Rev. C **83**, 037303 (2011).

[27] D. E. Archer, M. A. Riley, T. B. Brown, J. Döring, D. J. Hartley, G. D. Johns, T. D. Johnson, R. A. Kaye, J. Pfohl, S. L. Tabor, et al., Phys. Rev. C **52**, 1326 (1995).

[28] S. S. Bhattacharjee, R. Bhattacharjee, R. Raut, S. S. Ghugre, A. K. Sinha, L. Chaturvedi, T. Trivedi, U. Garg, S. R. B. K. Yogi, M. K. Raju, et al., Phys. Rev. C **91**, 044306 (2015).

[29] W. R. Leo, *Techniques for Nuclear and Particle Physics Experiments* (Springer, 1993).

[30] M. Lipoglavšek, A. Likar, M. Vencelj, T. Vidmar, R. A. Bark, E. Gueorguieva, F. Komati, J. J. Lawrie, S. M. Maliage, S. M. Mullins, et al., Nucl. Instr. Meth. Phys. Res. A **557**, 523 (2006).

[31] M. S. Sarkar, P. Dutta, I. Ray, C. Dey, S. Chattopadhyay, A. Goswami, P. Banerjee, R. Singh, P. Joshi, S. Paul, et al., Nucl. Instr. Meth. Phys. Res. A **491**, 113 (2002).

[32] M. S. Sarkar, R. Kshetri, R. Raut, A. Mukherjee, M. Sinha, M. Ray, A. Goswami, S. Roy, P. Basu, H. Majumder, et al., Nucl. Instr. Meth. Phys. Res. A **556**, 266 (2006).

[33] G. Duchêne, F. A. Beck, P. J. Twin, G. de France, D. Curien, L. Han, C. W. Beausang, M. A. Bentley, P. J. Nolan, and J. Simpson, Nucl. Instr. Meth. Phys. Res. A **432**, 90 (1999).

[34] Z. Elekes, T. Belgya, G. L. Molnár, A. Z. Kiss, M. Csatlós, J. Gulyás, A. Krasznahorkay, and Z. Máté, Nucl. Instr. Meth. Phys. Res. A **503**, 580 (2003).

[35] URL `http://geant4.web.cern.ch/geant4/`.

[36] P. K. Joshi, H. C. Jain, A. S. Medhi, S. Chattopadhyay, S. Bhattacharya, and A. Goswami, Nucl. Instr. Meth. Phys. Res. A **399**, 51 (1997).

[37] S. Muralithar, K. Rani, R. Kumar, R. P. Singh, J. J. Das, J. Gehlot, K. S. Golda, A. Jhingan, N. Madhavan, S. Nath, et al., Nucl. Instr. Meth. Phys. Res. A **622**, 281 (2010).

[38] R. Palit, S. Saha, J. Sethi, T. Trivedi, S. Sharma, B. S. Naidu, S. Jadhav, R. Donthi, P. B. Chavan, H. Tan, et al., Nucl. Instr. Meth. Phys. Res. A **680**, 90 (2012).

[39] S. Saha, R. Palit, J. Sethi, T. Trivedi, P. C. Srivastava, S. Kumar, B. S. Naidu, R. Donthi, S. Jadhav, D. C. Biswas, et al., Phys. Rev. C **86**, 034315 (2012).

[40] N. S. Pattabiraman, S. N. Chintalapudi, and S. S. Ghugre, Nucl. Instr. Meth. Phys. Res. A **526**, 432 (2004).

[41] N. S. Pattabiraman, S. N. Chintalapudi, and S. S. Ghugre, Nucl. Instr. Meth. Phys. Res. A **526**, 439 (2004).

[42] S. L. Tabor, Nucl. Instr. Meth. Phys. Res. A **265**, 495 (1988).

[43] R. Chakrabarti, Ph.D. thesis, UGC DAE CSR, KC (2012).

[44] URL `http://radware.phy.ornl.gov/`.

[45] D. C. Radford, Nucl. Instr. Meth. Phys. Res. A **361**, 297 (1995).

[46] K. S. Krane, *Introductory Nuclear Physics* (John Wiley & Sons, Inc., New York, 1988).

[47] K. Siegbahn, *Alpha-, Beta- And Gamma-Ray Spectroscopy* (North-Holland Publications, 1979).

[48] T. Yamazaki, Nucl. Data. A **3**, 1 (1967).

[49] E. D. Mateosian and A. W. Sunyar, Atomic. Nucl. Data **13**, 391 (1974).

[50] P. Singh, R. G. Pillay, J. A. Sheikh, and H. G. Devare, Phys. Rev. C **45**, 2161 (1992).

[51] P. M. Jones, L. Wei, F. A. Beck, P. A. Butler, T. Byrski, G. Duchêne, G. de. France, F. Hannachi, G. D. Jones, and B. Kharraja, Nucl. Instr. Meth. Phys. Res. A **362**, 556 (1995).

[52] J. K. Deng, W. C. Ma, J. H. Hamilton, A. V. Ramayya, J. Rikovska, N. J. Stone, W. L. Croft, R. B. Piercey, J. C. Morgan, P. F. Mantica, et al., Nucl. Instr. Meth. Phys. Res. A **317**, 242 (1992).

[53] J. C. Wells and N. R. Johnson, ORNL Report **6689**, 44 (1991).

[54] L. W. Nordheim, Phys. Rev. **75**, 1894 (1949).

[55] J. B. McGrory and B. H. Wildenthal, Ann. Rev. Nucl. Part. Sci **30**, 383 (1980).

[56] B. A. Brown, A. Etchegoyen, and W. D. M. Rae, OXBASH (unpublished) (1984).

[57] B. A. Brown and W. D. M. Rae, MSU-NSCL Report (2007).

[58] E. Caurier and F. Nowacki, Acta. Phys. Pol. B **30**, 705 (1999).

[59] P. Ring and P. Schuck, *The Nuclear Many-Body Problem* (Springer, 2000).

[60] W. A. Richter, S. Mkhize, and B. A. Brown, Phys. Rev. C **78**, 064302 (2008).

[61] W. A. Richter and B. A. Brown, Phys. Rev. C **80**, 034301 (2009).

[62] W. Brendler, P. Betz, E. Bitterwolf, and H. Röpke, Z. Phys. A **281**, 75 (1977).

[63] P. A. Butler, A. J. Brown, L. L. Green, A. N. James, C. J. Lister, J. D. MacArthur, P. J. Nolan, and J. F. Sharpey-Sahafer, J. Phys. G **1**, 665 (1975).

[64] D. M. Headly, R. K. Sheline, S. L. Tabor, U. J. Hüttmeier, C. J. Gross, E. F. Moore, B. H. Wildenthal, H. R. Weller, R. M. Whitton, and I. Ragnarsson, Phys. Rev. C **38**, 1698 (1988).

[65] N. Hinohara and Y. Kanada-En'yo, Phys. Rev. C **83**, 014321 (2011).

[66] J. E. Christiansson, J. Dubois, H. Roth, and L. Jarneborn, Phys. Scr. **14**, 193 (1976).

[67] K. L. Keyes, A. Papenberg, R. Chapman, J. Ollier, X. Liang, M. J. Burns, M. Labiche, K. M. S. N. Amzal, C. Beck, P. Bednarczyk, et al., J Phys. G **31**, S1903 (2005).

[68] Y. Kanada-Eńyo, M. Kimura, and H. Horiuchi, Nucl. Phys. A **738**, 3 (2004).

[69] A. Gavron, Phys. Rev. C **21**, 230 (1980).

[70] URL `http://root.cern.ch/drupal/`.

[71] R. Palit, H. C. Jain, P. K. Joshi, S. Nagaraj, B. V. T. Rao, S. N. Chintalapudi, and S. S. Ghugre, Pramana **54**, 347 (2000).

[72] P. M. Endt, Nucl. Phys. A **521**, 1 (1990).

[73] A. Nagel, G. D. Jones, P. R. G. Lornie, M. R. Nixon, H. G. Price, and P. J. Twin, J. Rev. G **1**, 324 (1975).

[74] E. K. Warburton, J. A. Becker, and B. A. Brown, Phys. Rev. C **41**, 1147 (1990).

[75] W. A. Richter, S. Mkhlze, and B. A. Brown, Phys. Rev. C **78**, 064302 (2008).

[76] P. C. Bender, C. R. Hoffman, M. Wiedeking, J. M. Allmond, L. A. Bernstein, J. T. Burke, D. L. Bleuel, R. M. Clark, P. Fallon, B. L. Goldblum, et al., Phys. Rev. C **80**, 014302 (2009).

[77] G. Neyens, Phys. Rev. C **84**, 064310 (2011).

[78] J. R. Terry, B. A. Brown, C. M. Campbell, J. M. Cook, A. D. Davies, D. C. Dinca, A. Gade, T. Glasmacher, P. G. Hansen, B. M. Sherrill, et al., Phys. Rev. C **77**, 014316 (2008).

[79] T. T. Bardin, J. A. Becker, T. R. Fisher, and A. D. W. Jones, Phys. Rev. Lett. **24**, 772 (1970).

[80] T. T. Bardin, J. A. Becker, T. R. Fisher, and A. D. W. Jones, Phys. Rev. C **4**, 1625 (1971).

[81] D. Steppenbeck, A. Deacon, S. Freeman, R. Janssens, M. Carpenter, C. Hoffman, B. Kay, T. Lauritsen, C. Lister, D. ODonnell, et al., Nucl. Phys. A **847**, 149 (2010).

[82] M. Ionescu-Bujor, A. Iordachescu, D. R. Napoli, S. N. Lenzi, N. Marginean, T. Otsuka, Y. Utsuno, R. V. Ribas, M. Axiotis, D. Bazzacco, et al., Phys. Rev. C **73**, 024310 (2005).

[83] P. Mason, N. Marginean, S. N. Lenzi, M. Ionescu-Bujor, F. D. Vedova, D. R. Napoli, T. Otsuka, Y. Utsuno, F. Nowacki, M. Axiotis, et al., Phys. Rev. C **71**, 014316 (2005).

[84] C. E. Svensson, A. O. Macchiavelli, A. Juodagalvis, A. Poves, I. Ragnarsson, S. Åberg, D. E. Appelbe, R. A. E. Austin, C. Baktash, G. C. Ball, et al., Phys. Rev. L **85**, 2693 (2000).

[85] E. Ideguchi, D. G. Sarantites, W. Reviol, A. V. Afanasjev, M. Devlin, C. Baktash, R. V. F. Janssens, D. Rudolph, A. Axelsson, M. P. Carpenter, et al., Phys. Rev. L **87**, 222501 (2001).

[86] Y. Taniguchi, Y. Kanada-Eńyo, and M. Kimura, Phys. Rev. C **80**, 044316 (2009).

[87] F. Glatz, J. Siefert, P. Betz, E. Bitterwolf, A. Burkard, F. Heidinger, T. Kern, R. Lehmann, S. Norbert, and H. Röpke, Z. Phys. A **303**, 239 (1981).

[88] S. DasGupta and M. Harvey, Nucl. Phys. A **94**, 602 (1967).

[89] I. Ragnarsson and S. Åberg, Phys. Lett. B **114**, 387 (1982).

[90] I. Ragnarsson, S. Åberg, and R. K. Sheline, Phys. Scr. **24**, 215 (1981).

[91] J. Darai, J. Cseh, and D. G. Jenkins, Phys. Rev. C **86**, 064309 (2012).

[92] M. A. Islam, T. J. Kennett, and W. V. Prestwich, Phys. Rev. C **41**, 1272 (1990).

[93] M. J. Kenny, B. J. Allen, J. W. Boldem, and A. M. R. Joye, Nucl. Phys. A **270**, 164 (1976).

[94] L. R. Medsker, H. E. Jackson, and J. L. Yntema, Phys. Rev. C **9**, 1851 (1974).

[95] L. Meyer-Schützmeister, D. S. Gemmell, R. E. Holland, F. T. Kuchnir, H. Ohnuma, and N. G. Puttaswamy, Phys. Rev. **187**, 1210 (1969).

[96] S. Raman, E. T. Jurney, J. W. Starner, and J. E. Lynn, Phys. Rev. C **46**, 972 (1992).

[97] D. A. Viggars, P. A. Butler, P. E. Carr, L. L. Gadeken, L. L. Green, A. N. James, P. J. Nolan, and J. F. Sharpey-Schafter, J. Phys. A **7**, 360 (1974).

[98] E. Bitterwolf, P. Betz, A. Burkard, F. Glatz, F. Heidinger, T. Kern, R. Lehmann, , S. Norbert, J. Siefert, et al., Z. Phys. A **298**, 279 (1980).

[99] URL `www.srim.org`.